UNIVERSITY OF TRENTO

DOCTORAL THESIS

Multi-gain interferometric laser for intra-cavity beam combining

Author:
Sara PICCIONE

Supervisor:
Academic:
Prof. Lorenzo PAVESI
Industrial:
Maurizio Sbetti
Cristiano Raffaldi

A thesis submitted in fulfillment of the requirements for the degree of Doctor of Philosophy

in the

Nanoscience Laboratory
Department of Physics

July 10, 2020

Declaration of Authorship

I, Sara PICCIONE, declare that this thesis titled, "Multi-gain interferometric laser for intra-cavity beam combining" and the work presented in it are my own. I confirm that:

- This work was done wholly or mainly while in candidature for a research degree at this University.
- Where any part of this thesis has previously been submitted for a degree or any other qualification at this University or any other institution, this has been clearly stated.
- Where I have consulted the published work of others, this is always clearly attributed.
- Where I have quoted from the work of others, the source is always given. With the exception of such quotations, this thesis is entirely my own work.
- I have acknowledged all main sources of help.
- Where the thesis is based on work done by myself jointly with others, I have made clear exactly what was done by others and what I have contributed myself.

Signed: _____

Date: _____

Contents

List of Abbreviations

LASER	**L**ight **A**mplification by **S**timulated **E**mission of **R**adiation
MASER	**M**icrowave **A**mplification by **S**timulated **E**mission of **R**adiation
VCSEL	**V**ertical **C**avity **S**urface **E**mitting **L**aser
BPP	**B**eam **P**arameter **P**roduct
DDL	**D**irect **D**iode **L**aser
COD	**C**atastrophic **O**ptical **D**amage
BAL	**B**road **A**rea **L**aser
SCOWL	**S**lab **C**oupled **O**ptical **W**aveguide **L**aser
IBC	**I**ncoherent **B**eam **C**ombining
SBC	**S**patial **B**eam **C**ombining
PBC	**P**olarization **B**eam **C**ombining
WBC	**W**avelength **B**eam **C**ombining
CBC	**C**oherent **B**eam **C**ombining
OPPL	**O**ptical **P**hase **L**ock **L**oop
SPGH	**S**tochastic **P**arallel **G**radient **D**escent
MOPA	**M**aster **O**scillator **P**ower **A**mplifier
MO	Master Oscillator
SCOWA	**S**lab **C**oupled **O**ptical **W**aveguide **A**mplifier
OC	**O**utput **C**oupler
DOE	**D**iffractive **O**ptical **E**lement
ISA	**I**nterferometric **S**emiconductor **A**mplifier
SOA	**S**emiconductor **O**ptical **A**mplifier
TW	**T**raveling **W**ave
DH	**D**ouble **H**eterojunction
MQW-SOA	**M**ulti **Q**uantum **W**ell **A**mplifier
RW	**R**idge **W**aveguide
TEC	**T**hermo **E**lectric **C**ooler
NA	**N**umerical **A**perture
ASE	**A**mplified **S**pontaneous **E**mission
OSA	**O**ptical **S**pectrum **A**nalyzer
VOA	**V**ariable **O**ptical **A**ttenuator
SHB	**S**pectral **H**ole **B**urning
CH	**C**arrier **H**eating
TPA	**T**wo **P**hoton **A**bsorption
FCA	**F**ree **C**arrier **A**bsorption
FC	**F**ree **C**arriers
MZI	**M**ach **Z**ender **I**nterferometer
ECL	External **C**avity **L**aser
FT	**F**ourier **T**ransform
DFT	**D**iscrete **F**ourier **T**ransform
FFT	**F**ast **F**ourier **T**ransform
SFT	**S**caled **F**ourier **T**ransform
NA	**N**umerical **A**perture

CM	**C**urved **M**irror
VBW	**V**ideo **B**and**W**idth
BS	**B**eam **S**plitter
BC	**B**eam **C**ombiner

To my family...

Chapter 1

Introduction

LASER is an acronym that stands for Light Amplification by Stimulated Emission of Radiation. The LASER is a device which emits a coherent light beam. The first step to the development of the LASER was made by Einstein in 1917 [1], when introducing the concept of stimulated emission. Nevertheless, for more than 30 years, stimulated emission received marginal attention and was used only in theoretical contests. The first operating device, based on stimulated emission was built by Charles Townes in 1953 [2]. The device, called MASER (Microwave Amplification by Stimulated Emission of Radiation), operated in the microwave regime and consisted of a beam of excited ammonia molecules placed into a resonant cavity. The result was the amplification of microwaves at a frequency of about 24.0 GHz. Some years later, the collaboration between Townes and Arthur Shawlow lead to the theoretical foundation of the optical version of the maser, the LASER [3]. Based on this work, on May 16, 1960, Theodore Maiman and his group realized the first working laser [4]. The laser comprised two essential elements: an active medium, in which the stimulated emission took place, and an optical resonant cavity. The same configuration was maintained during the years. The active medium consisted of a ruby crystal, excited by a flash-lamp light. The external pump takes the system in a condition in which an higher energy level is more populated than the fundamental states. The equilibrium condition is restored by the spontaneous emission of photons. Because the medium is placed within a resonator, the portion of the emitted light, traveling parallel to the optical axis of resonator, bounces back and forth at the resonator mirrors, passing through the medium. The consequence is the emission of light, stimulated by the traveling optical beam.
The first continuous wave gas laser, the He-Ne laser, was demonstrated in 1961 [5]. The 1962, thanks to the improvements of semiconductor technology, is the birth date of the diode laser, where a small chip of GaAs semiconductor acted as the gain medium [6]. Today, laser diodes are the most used laser type. VCSELs (Vertical Cavity Surface Emitting Lasers) technology, in particular, is one of the fastest growing segment in the photonics market [7].
Devices operating at different wavelengths can be obtained exploiting different optical transitions of several active media, from solid state to gas material. Depending on the application lasers can operate in both continuous (CW) or pulsed wave operation.
Distinct types of laser can be used in a wide range of different applications, from scientific research to industrial applications. The important properties that enable the laser use in such a variety of applications are spatial and temporal coherence, low divergence, high power density and monochromaticity. Indeed, because of their properties, laser allows the realization of optical clocks of unprecedented accuracy [8] and can offers the most precise instrument to measure lengths [9]. Lasers affect also our everyday lives from medicine [10] and cosmetics [11], to entertainment [12]

and communications[13]. The graph in figure 1.1 shows the different laser market segments.

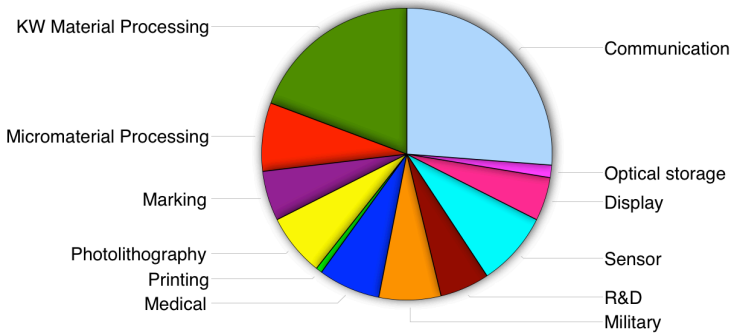

FIGURE 1.1: Laser Applications. Adapted according to the result reported in [7]

1.1 Material processing and laser brightness

Material processing represents the second biggest portion of the whole laser market. Laser material processing exploits the energy deposited in the material by an intense laser beam, to modify the structure of the processed material. Depending on the material and on the working condition of the laser source, only the surface region near the laser incidence point can be processed under extreme conditions, without affecting the properties of the bulk material. Depending on the laser power and on the interaction time different processes can be realized, as schematized in fig. 1.2

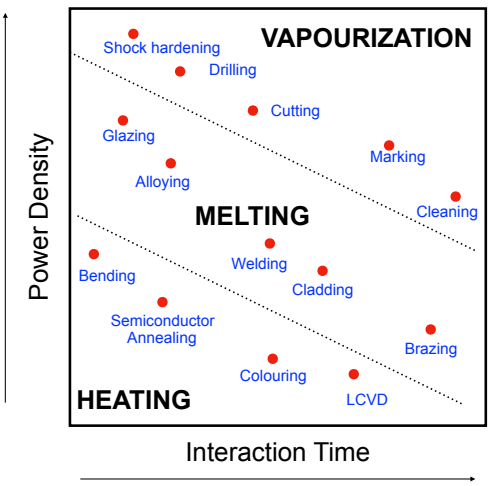

FIGURE 1.2: Schematic map of the processes, for different values of the power density and the interaction time. Adapted following the work in [14]

When a high energy density laser beam is focused on the surface of the material, the light is absorbed by the electrons in lattice vibrations and locally realize as heating. Thus, thermal energy causes the transformation of the material. The different

processes, according to the material response, can be grouped into three major categories: heating, melting and vaporization. Since laser material processing is a thermal effect, a big contribution in the effectiveness of the process depends on both the optical and mechanical properties of the material. A second fundamental role in determining the efficiency of the process is played by the properties of the used laser. In particular, a key parameter is the laser brightness, B [15]. This last is defined as the amount of light power per unit area, A per unit solid angle Ω,

$$B = \frac{P}{A\Omega} \tag{1.1}$$

where P indicates the laser power. The brightness is an unchangeable property, that is not affected by focusing elements, neither by the beam propagation, in absence of aberrations. The major contributors to the laser brightness are the laser beam parameters, in particular the laser beam quality. This last identifies the capability of a laser beam to be focused within a small spot size. Higher the beam quality, higher is the laser intensity at a given power.
The beam quality is typically quantified through the beam parameter product (BPP) or the beam propagation factor M^2. The BPP is defined as the product between the beam radius, w, and the beam divergence half-angle, θ

$$BPP = w \times \theta \tag{1.2}$$

The M^2 parameter is defined as

$$M^2 = \frac{BPP}{\lambda/\pi} \tag{1.3}$$

where λ stands for the laser emission wavelength.
The propagation factor gives an estimate of the beam degradation when compared to a diffraction-limited beam, for which $M^2 = 1$. Then, the laser brightness is defined as

$$B = \frac{P}{\lambda^2 M_x^2 M_y^2} \tag{1.4}$$

where M_x^2 and M_y^2 refers to the beam propagation factors along the x and y directions.
For material processing applications, high brightness laser sources offer several advantages with respect to other types of laser sources. Indeed, a higher brightness corresponds to a higher intensity within the same focusing area. This in turn, allows the achievement of a fine spot and creates a longer focusing distance. As a consequence a higher flexibility can be reached, since different distances between the source and the target can be covered. Second, a higher intensity ensures a high temperature during the interaction between the target and the source. The consequence is an increase of the processing speed, which in turn permits a cost reduction of the whole process. Therefore, for applications where high power density is needed, such as metal cutting, the use of a high brightness laser source is required.

1.2 High power, high brightness laser sources

Historically, the most utilized source in industry was the CO_2 laser [16]. In 1980s multikilowatt CO_2 lasers have been made available with higher beam quality and at a lower cost than other lasers. In this type of laser, the gain medium is a mixture of CO_2 and N_2 molecules. The nitrogen addition improves the CO_2 excitation [17]. The gas mixture is placed between an anode and a cathode, so that an electric discharge can be induced through the gas. The electric discharge excites the N_2 molecules in a metastable vibrational energy level. Because of the similarity between the resonance transitions of the two gases composing the mixture, a collisional energy transfer between nitrogen and carbon dioxide causes the excitation of this last. The result is the achievement of the population inversion, which is the necessary condition for starting and sustaining the laser emission. The consequent relaxation of the system towards the fundamental state causes the emission of a photon, which starts the laser oscillation. Figure 1.3 shows an example of a CO_2 laser cavity.

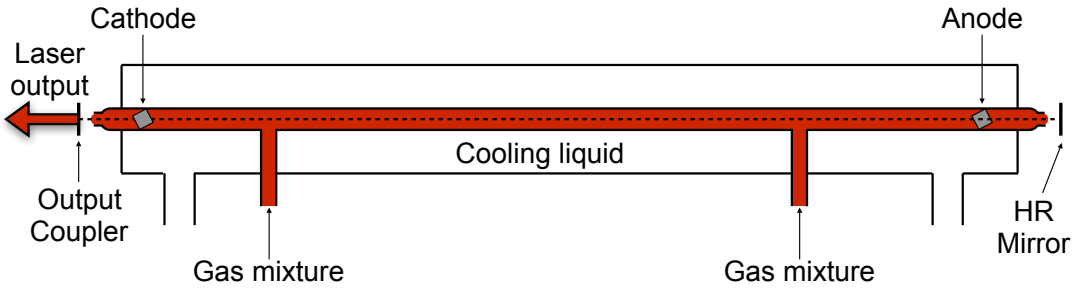

FIGURE 1.3: Scheme of the CO_2 laser device.

Laser systems with output power higher than $10kW$ have been operated in industrial environments for years. Typical values of the M^2 parameter range around $1 \div 1.2$, indicating a very high beam quality, while the emission wavelength is around $10\mu m$. The major drawback of CO_2 laser is the electrical-to-optical power efficiency, which is around 10%. Furthermore, because of the presence of the gas tube, the final device results in a very large apparatus. Moreover, because the laser system is fixed in place, several optical components are required to direct the laser beam towards the work station, where the material processing takes place.
The fiber laser, which nowadays dominates the high power laser market, overcomes all of these drawbacks, and offers a more efficient and feasible solution with respect to the CO_2 laser. In fiber lasers, the active medium is an optical fiber doped with rare-earth elements. Depending on the doping material (erbium, ytterbium or thulium) different emission wavelengths can be obtained, from $1.03\mu m$ to $2.1\mu m$. The laser cavity consists of a Fabry-Perot cavity, realized at the two fiber ends. Fiber Bragg Gratings acts as the cavity mirrors, providing the optical feedback that sustains the laser oscillation. The population inversion condition is achieved through optical pumping by high power semiconductor lasers. Figure 1.4 shows a scheme of the laser.
Fiber lasers offer several advantages with respect to the CO_2 laser. The optical fiber can be designed to support only the lowest-order mode. The result is a laser beam with a M^2 factor close to the ideal one, at no expense of the laser output power. The long length of the fiber improves both the heat dissipation and the total gain of the active region, making easier the implementation of strategies to scale up the

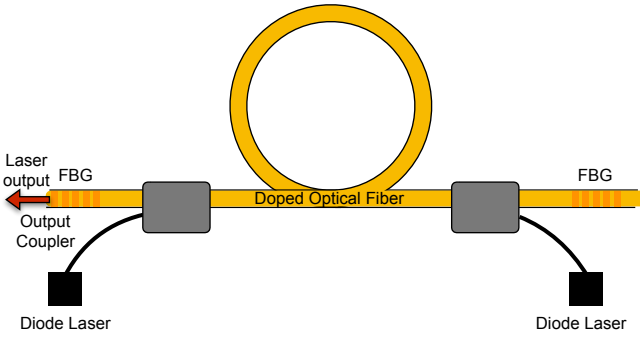

FIGURE 1.4: Typical design for fiber laser.

laser output power. Furthermore, the plug-in conversion efficiency is higher and can reach up to 50% [16]. The fiber effective mode area is one of the key parameter that needs to be considered to further scale up of the output power. In high power device, a large area is desirable to reduce nonlinear effects, associated with fiber lasers. An adopted strategy is the increase of the core diameter of the fiber, while minimizing the numerical aperture to maintain the single mode operation.
Laser system with output power as high as $100kW$ are already present in the market [18]. The achievement of such high values of power was possible thanks to the cladding pumping technique. The fiber presents a double-clad structure: the fiber core is clad by a surrounding layer where the pumping beam is confined by the second cladding. The pump is realized by coupling the output of several multimode broad area diode lasers into the clad region. Here the pump beam, while propagating in the fiber, overlaps with the rare earth doped core of the fiber. The rare-earth ions absorb the pump photons and re-emit coherent light at a different wavelength. The overall scheme can be viewed as a brightness converter of the multi-mode pumps, into a single beam of an excellent quality.
The primary use of high power semiconductor lasers has been as pumping sources. However, with the advancements both in the fabrication and packaging techniques, diode lasers are starting to be used as Direct Diode Laser (DDL) sources in industry. Laser diodes exhibit several advantages with respects to other laser technologies. Conversion efficiency as high as 70% are reported [19]. Simpler power suppliers are needed. The pumping is typically electrical, avoiding the presence of a second pump laser source. Laser chips of very small sizes can be realized, at very low costs. The technology is easy to integrate in more complex circuits, allowing the realization of compact and easy to use device. Volume production is also possible.
The major drawback that limits the use of diode lasers in industrial applications is their relatively low output power. This last is typically limited to some tens of watts [20]. Indeed, an higher output power corresponds to an higher current injected into the material. However, such an increase causes many detrimental effects, such catastrophic optical damage (COD) and thermal rollover [21]. These processes originate from the high power density hitting the semiconductor facets. The resulting heat generation causes either direct damage or themo-optical distortion of the semiconductor laser beam.
The increase of the diode laser brightness is now one of the primary goal of the laser researcher community for industrial application. The first adopted strategy to increase the laser output power was based on the increase of the active area of the semiconductor material. The obtained devices are typically referred to as broad-area lasers (BALs). The typical dimensions of the laser active region are of the order of

some $100\mu m$. The resulting emitted beam is multimode. For this reason, the power increase does not translate into a brightness increase. Indeed, the laser beam quality is limited by the multimode nature of the emitted beam. Moreover, in BALs, the beam quality can further degrade because of the filamentation effect [22]. The phenomenon arises from the decrease of the lateral confinement of the propagating light in BALs. In these conditions, even small local variations of the refractive index can lead to detrimental phenomena, breaking the lateral mode profiles into multiple filaments[23].
The successive solutions were devoted to the search for a design of the laser chip, that allows both the maintaining of the single mode operation and the output power increase. The Slab-Coupled Optical Waveguide Laser (SCOWL) [24] supports a large size optical mode that reduces the power density at the chip facets. A schematic cross-section of the device is shown in fig. 1.5a. The device resemble a ridge diode laser. However, here the ridge is etched into the waveguide layer forming the rib region. This results in a larger thickness of the waveguide layer. The larger mode size reduces the power density at the facets, while, because of the slab coupling, the higher order transversal modes are not guided.

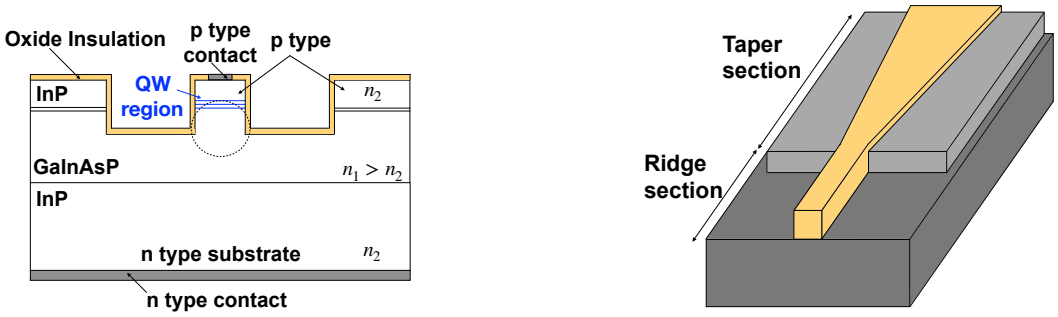

(A) (B)

FIGURE 1.5: (a): Cross section of the SCOWL, according to [25]. (b): Scheme of a tapered diode laser [26] .

The tapered laser [27] uses a different chip design. This last consists of two different geometries, as shown in fig. 1.5b. A single mode ridge waveguide is monolitycally integrated with a tapered amplifier. While the ridge section acts as a mode filter, the larger dimension of the tapered region enables high laser output power.
Nevertheless, the laser output power is still limited to some tens of watts [28].

1.3 Beam combining

The most accomplished technique to achieve the scaling up of the diode laser brightness is through the beam combination of several separated emitters. Different types of beam combining techniques can be distinguished, mainly divided in two categories: incoherent and coherent beam combining techniques. While in incoherent beam combining (IBC) schemes, the emitters are uncoupled, in coherent beam combing the beams must have identical emission spectra and a well definite phase relationship, in order to achieve the conditions for constructive interference. Because of the difficulties in the phase control of each emitters, especially due to thermal instabilities and mode hopping coherent beam combining is rarely implemented. Therefore, incoherent beam combining techniques are typically preferred.

1.3.1 Incoherent Spatial Beam Combining and Diode laser arrays

The easiest beam combining scheme is the Spatial Beam Combining (SBC) [29]. The method consists in placing several emitters next to each other. Diode laser bars and stacks can be realized depending if the combining happens in one or two dimension. The operating wavelength may or may not be equal for each individual emitter, and no attempt is made to control the relative spectra or phases of the elements. The output power increases linearly with the number of emitters, at expense of the overall laser beam quality. The beam quality depends on the arrangement of the free areas between the individual diodes, which is quantified by the filling factor, F. The filling factor expresses the ratio between the separation distance of two adjacent emitters, x_0, and the width of the emitted beam, w_0 [30]

$$F = \frac{x_0}{2w_0} \tag{1.5}$$

In the ideal case, when $F \approx 1$, the output beam radius is roughly N times the radius of the individual beam [1], with N being the number of combined emitters. As a consequence, the BPP is N times the BPP of the individual beam. Figure 1.6 shows both the near and far field profile for both a diode bar and stack, compared with the single emitter.

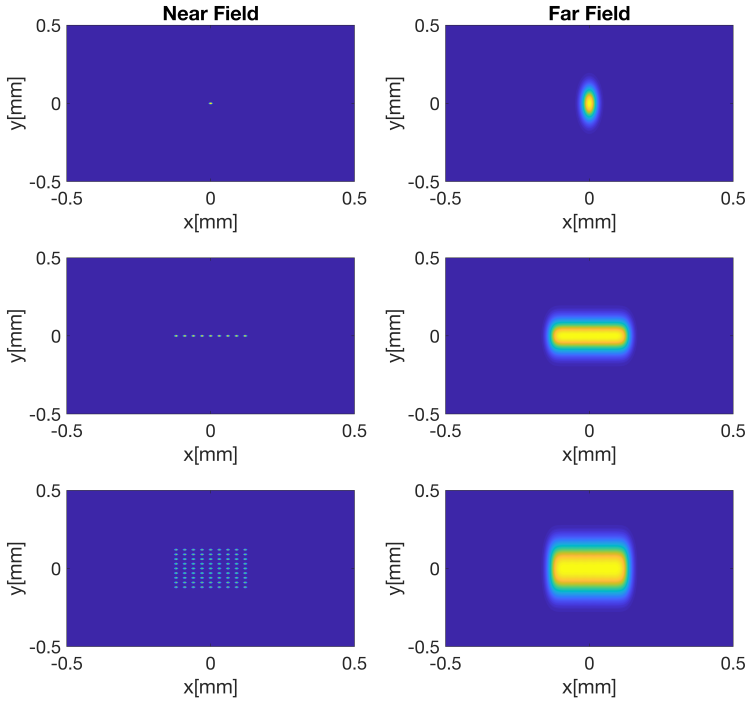

FIGURE 1.6: Near and Far field profile for a singel emitter diode laser, a diode bar and a diode stack.

The collimation condition of the individual laser beams influences the filling factor on both the slow and the fast axis. Therefore, the choice of the lenses array to properly shape the emitted radiation become crucial. Depending on the application, the

[1] If the intensity distribution is similar for all the combined emitters.

use of a high power source realized by using SBC requires a fiber coupling stage. Different strategies are adopted for shaping the beam to increase the fiber coupling efficiency [31, 32, 33]. The different methods are characterized by different configuration of mirrors and lenses. An example of application, where SBC is typically used, are the pumping sources of fiber lasers.

1.3.2 Incoherent Polarization Beam Combining

A second implementation of incoherent beam combining is realized exploiting the beam polarization and it is referred to as Polarization Beam Combining (PBC) [34]. Two linearly polarizing beams of opposite polarization are sent to a polarized beam splitter or to a thin-film polarizer. Such a polarization sensitive element transmits only a given polarization, while reflects the other. When the two beams, traveling along perpendicular directions, encounter the polarizer, they will be directed in the same direction. At the output of the splitter, one obtains an unpolarized beam having the combined optical power of the input beams and the same beam quality of the individual beam. The result is a doubled brightness. This method, however, can be applied to only two beams and cannot be scaled to many beams. Nevertheless, it is typically implemented with other architectures, to further improve the overall laser performance.

1.3.3 Incoherent Wavelength Beam Combining

Incoherent Wavelength Beam Combining (WBC), also known as spectral beam combining, is probably the most efficient way for realizing a high power, high brightness diode laser for direct industrial applications [35]. Here, the array elements operate at different wavelengths, and one or more dispersive optical elements are used to overlap the different beams. As for the SBC, the power of the individual emitters ideally increases as the number of the combined elements increases. However, the beam quality of the final output beam equals the beam quality of the single emitter. This also means that the laser brightness increases with the number of emitters. The only fundamental requirement is that the power spectra of the elements not overlap with each other. A potential overlap will cause the beams to interfere and, consequently, to get an efficient combining would require also the control of the phase.

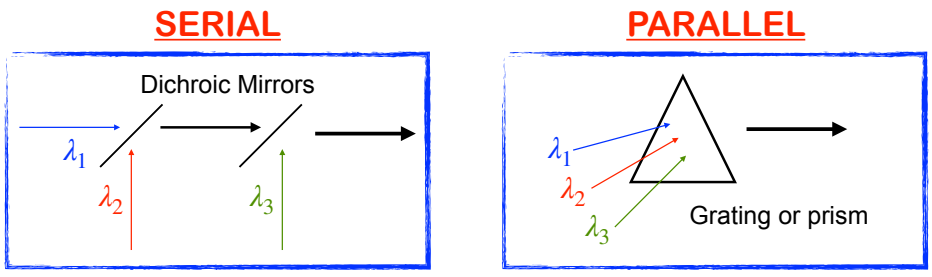

FIGURE 1.7: Seial WBC on the left panel. Parallel WBC on the right panel

Depending on the frequency spacing among the emitters, Coarse or Dense WBC are distinguished.
In general, WBC architectures can be divided into two subsets, serial and parallel, depending on the combining element, as reported in fig. 1.7. In the serial approach

the combining of N beams requires $N-1$ combiner elements, different from each other. The high number of optical components makes more difficult the alignment of the whole device and could reduce the combining efficiency. Therefore, the approach has proven to be effective only for a small number of emitters. On the contrary, parallel implementation requires only a single diffractive optical element. The first examples of the two architectures were early proposed during the 70s [36, 37], but the lack of sufficient wavelength stabilization mechanism, causes a relatively low combining efficiency and poor beam quality of the obtained laser.
The turning point has been reached in the early 2000s by the Laser Technology Applications Group of MIT Lincoln Laboratory [38]. The invented WBC architecture simultaneously achieves a nearly ideal beam combination and provides a wavelength stabilization system. A schematic of this implementation is shown in fig. 1.8. It consists of an array of semiconductor gain elements, a transform lens, a diffraction grating, and a partially reflective output coupler (OC). One of the two facets of each emitter is cleaved, acting as one of the external cavity mirror. The lens, when placed at one focal length from the array, converts the position of each element into a well definite angle of incidence on the grating, where the beams overlap. The different angles of incidence correspond to different emission wavelengths for each diode, selected by the external resonator.

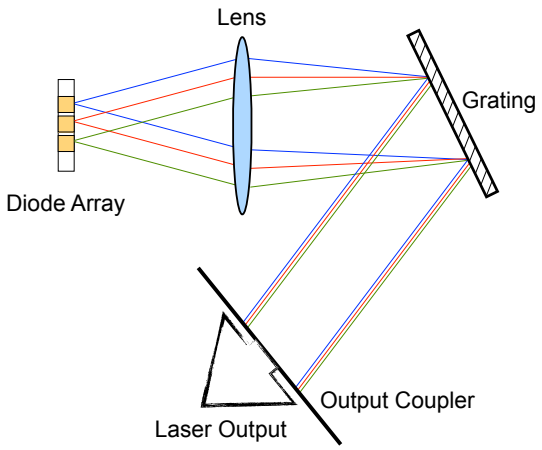

FIGURE 1.8: Schematic of the External Cavity WBC architecture. The image was remade according to [38].

The final result is a single output beam both in the near and far field, whose beam quality equals the one of the single emitter. A similar scheme can also be implemented for 2D WBC. The number of elements is limited by the grating resolution. Indeed, the dispersive element determines the minimum bandwidth allocation and sets the spectral separation between the emitters. A second limitation arises from the need to maintain the optical intensity under a certain critical value, to avoid both optical damage and thermo-optically distortion, and maintain a high beam quality.
The only drawback of the proposed scheme, is that the emission spectrum of the combined beam contains the spectral contribution of the single emitters, causing a decrease of the laser spectral brightness. However, for material processing applications, where the spatial brightness has more importance than the spectral brightness, the proposed architecture has been proved to be a valid alternative to the other laser solutions already used [39, 40].

Nowadays, the incoherent technology is ready for the market and the various products offered by the companies are characterized by different values of the laser output power and beam quality. Table 1.1 shows the major characteristic of some of the high power DDLs commercialized in the photonics industry.

Company	Product	Output Power	BPP	Reference
Teradiode	*TeraBlade*	$8kW$	$< 3.8mm \times mrad$	[41]
Trumpf	*TruDiode*	$6kW$	$30mm \times mrad$	[42]
Lumentum	*Corelight Direct Diode*	$6kW$	$50mm \times mrad$	[43]
Laserline	*LDF Series*	$40kW$	$220mm \times mrad$	[44]
Coherent	*DL Series*	$4kW$	$< 30mm \times mrad$	[45]

TABLE 1.1: High power Direct Diode Laser sources commercialized. The sources were all realized using incoherent combining techniques. Typically a modular approach is employed and both SBC and WBC are used.

The different systems, listed in table 1.1 are based on a modular approach. The differences between the various DDLs primary regard the total number of combined elements, the beam shaping unit [46, 47, 48, 49, 50] and the choice of the diffractive elements, as beam combiners, in WBC scheme [51, 52, 53, 54]. The different strategies influence the resulting beam quality. This last, in turn, defines the material processing application in which the DDL can be used.

1.3.4 Coherent Beam Combining

In coherent beam combining (CBC) schemes, the output beam is the result of the constructive interference between separated sources [55]. In CBC each element composing the array needs to operate with the same wavelength, and their relative phases need to be controlled to guarantee the condition for constructive interference. Two different types of CBC implementations can be distinguished, tiled aperture and filled aperture, depending if the interference occurs in far or near fields. In tiled aperture, beams are adjacent to each other and the interference happens only in the far field. To maximize the far-field intensity, the fill factor should be as high as possible, to reduce side lobes. On the contrary, in filled aperture CBC, the interference occurs in the near field thanks to the use of a beam combiner, which can be viewed as the inverse of a beam splitter and needs to be designed specifically.
The most difficult part in the realization of a successful CBC scheme is the phase control, which is particular demanding for semiconductor laser. Different implementations have been proposed and can be grouped into two subsets depending if the phase control is achieved actively or passively [34].
Actively controlled CBC is mainly implemented in the Master Oscillator Power Amplifier (MOPA) configuration, shown in fig. 1.9 [56]. Here, a master (or seed) laser oscillator (MO) is amplified by multiple amplifiers.
The amplified beams are then combined together, by means of CBC. Key issue is the determination of both the optical path difference and the correction, that needs to be applied, to equalize the amplifier phases. Commonly, two different types of control algorithms are used. The first detects the phase and corrects it via dedicated Optical Phase-Lock Loops (OPLLs)[57]. The second, which is easier to implement, detects the combined intensity. The individual phases of the emitters are controlled in order

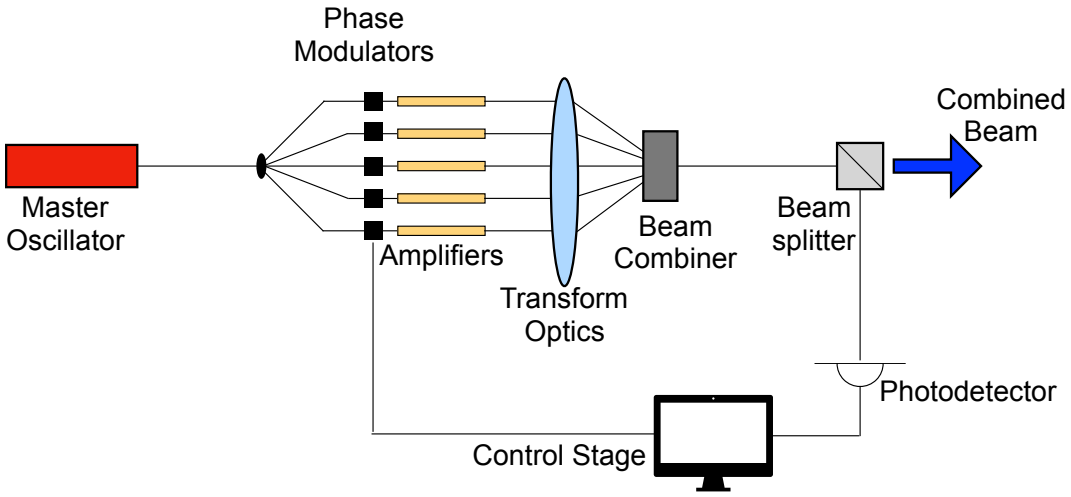

FIGURE 1.9: Scheme of the Master Oscillator Power Amplifier architecture.

to maximize both the laser power and the laser beam quality. In [58] the Stochastic Parallel Gradient Descent (SPGD) [59] is used to maximize the CBC combining efficiency. A MO is sent into an array of 47 slab-coupled optical waveguide amplifier (SCOWA). An output power of 40W has been measured, while the reported M^2 parameter varied between 1.2 and 1.3.
Active phase control algorithms have been proven to be effective also in absence of a master oscillator when combining diode lasers [60].
Passive-feedback CBC implementations, characterized by the absence of control stages, can be realized in several ways. In evanescent-wave coupling approaches [61], the individual emitters are placed sufficiently closed together. Their far field distributions overlap and interference occurs. The spacing between the array elements determines the strength of the coupling.
A more effective approach involves the use of a common resonator[62]. An example is shown in fig. 1.10.

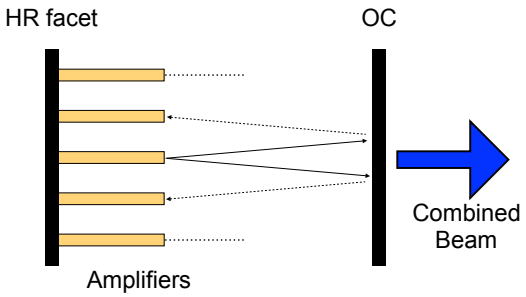

FIGURE 1.10: CBC implementation in a common resonator. The optical feedback from the cavity OC couples the array elements together.

Here, the array elements are placed inside an optical resonator, and the feedback from the resonator itself couples the element together. Each element of the array can be viewed as a separate optical resonator, and the emission wavelength is in principle locked separately. However, if the emission wavelength bandwidth is the same for all the emitter, eventually the mutual injection caused by the common resonator

will force a common and unique emission wavelength, consistent with the lowest intracavity losses.A further development in the common resonator design involves the of introduction of intracavity spatial filters [63] to suppress all the higher order transversal mode.
The Talbot effect is also used to passively establish the proper phase relationship, to obtain the constructive interference conditions [64]. The Talbot effect is a near-field diffraction effect [65]. It was demonstrated that a coherent light field, periodic in both transverse directions, induces a periodicity also in the propagation direction. As a result, the field exactly reproduces itself when the propagation distance is a multiple of a specific distance, called Talbot distance. This last depends on the beam wavelengt and on the period. The effect has been used in designing CBC common resonator architectures [66, 67, 68]. Here the periodicity refers to the separation distance between two adjacent emitters, composing the array. When the proper phase relationship among the different emitters is established, the resulting mutually coherent field reproduces itself. If the cavity round-trip is equal to an integer multiple of the Talbot distance, the obtained field exactly matches the original field, allowing the light to efficiently couples back into the emitters. For an incoherent ensemble, the Talbot self-imaging does not occur, resulting in a very poor coupling efficiency. Therefore, the optical mode corresponding to the coherent state represents also the condition of minimum cavity losses.
A different approach for realizing a passive CBC implementations consists in overlapping the beams emitted from the array elements in a common area, within the resonator. This could be either a Michelson interferometric resonator [69] or a Diffractive Optical Element (DOE) resonator [60], both depicted in fig. 1.11.

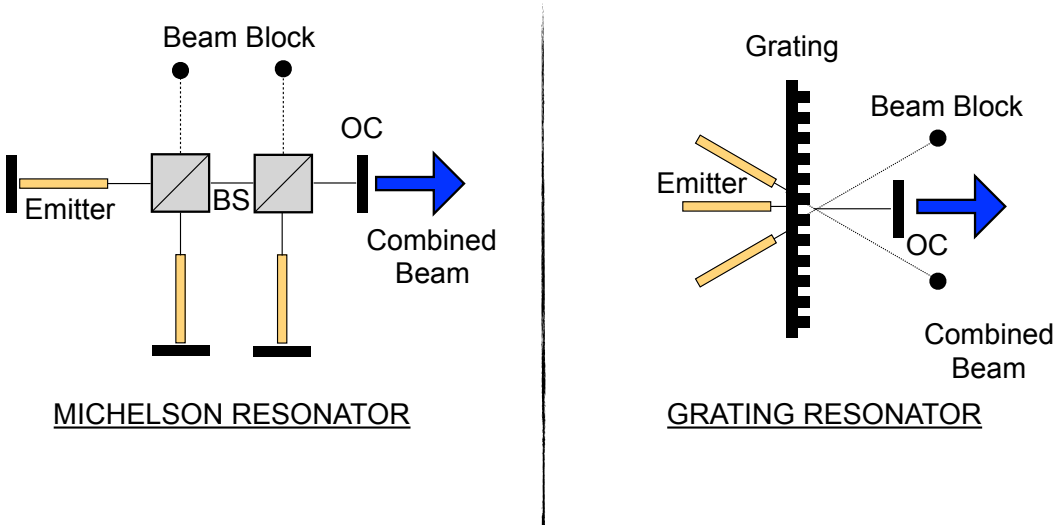

FIGURE 1.11: Scheme for CBC implementation based on beam superposition. In the left panel, the emitters are placed into a Michelson resonator, while the right panel depicts a grating resonator.

The emitters, which can have significantly different optical paths, are placed together in the resonator. First, the individual beams overlap in the beam splitters or in the DOE, where interference occurs. Then the resulting field is reflected back towards the emitters by the cavity OC. Similarly to the previous configuration, the resulting spectrum self-adjust in order to minimize the losses and maximize the coupling efficiency. This condition occurs when the constructive interference is verified.

Table 1.2 summed up some of the most relevant results reported in literature, when coherently combining diode lasers. Passive-feedback architectures avoid the use of phase control stages and the implementation of sophisticated algorithms. Nevertheless, they seem to be effective only for a relatively small numbers of combined emitters. On the other hand, actively-feedback CBC implementations offer a more robust solution, and higher values of output power have been obtained.

Reference	Phase Control	Method	Power	N
[58]	SPGD algorithm active	MOPA	$40W$	47
[57]	OPPL algorithm active	MOPA	$110W$ [2]	4
[63]	Passive	Spatial filtered resonator	$\approx 10W^{\diamond}$	35
[68]	Passive	Talbot resonator	$7.2W$	10
[69]	Passive	Michelson resonator	$6.7W$	2
[59]	SPGD algorithm active	DOE resonator	$1.2W$	21

TABLE 1.2: Summary of some of CBC solutions, proposed in literature. The symbol $\diamond$ indicates values estimated from the published data.

CBC can result in final beam with excellent properties, however, the combining efficiency is extremely sensitive to external parameter fluctuations, such as power changes, laser phase variation and misalignments. As a consequence, contrary to IBC, it is rarely implemented in industrial applications.

1.4 This Work

This work aims at demonstrating a new scheme of a laser based on CBC and was entirely supported by BLM Group Adige S.p.A. BLM Group is a worldwide company leader in the production of state-of the art systems for processing tubes. It is divided into three company; **BLM** specialized in the production of tube and wire bending machines, **ADIGE-SYS** for tube and sheet laser cutting systems, and **ADIGE** for tube laser-cutting systems. Today the most used laser source, in Adige systems, are fiber lasers.
My PhD project comes from the collaboration between Adige and the Universtity of Trento. The aim of the work was the proposal and the consequent study of the feasibility of a new power scaling architecture, entirely based on semiconductor laser diodes.
In this thesis I will propose a new laser architecture based on passive CBC architectures. Its aim is to provide an alternative laser cavity geometry where multiple gain stages are combined together in an intra-cavity scheme. The main block of the scheme is an Interferometric Semiconductor Amplifier (ISA). In an ISA, the optical amplifier is placed into one arm of a Mach-Zender interferometer. The input signal is divided into two arms. A major portion of the incoming beam travels unperturbed, while a smaller portion undergoes amplification. The power at the output of the ISA is the results of the constructive interference of the two beams. The main advantage of the ISA is the reduction of the power circulating on the amplifier. This in turn, reduces all the degradation effects associated with high power and nonlinear

[2] The value does not refer to a solution entirely based on semiconductor lasers. Fiber amplifiers were used to further amplified the output power.

behavior. The results is a device with a higher reliability and lifetime.

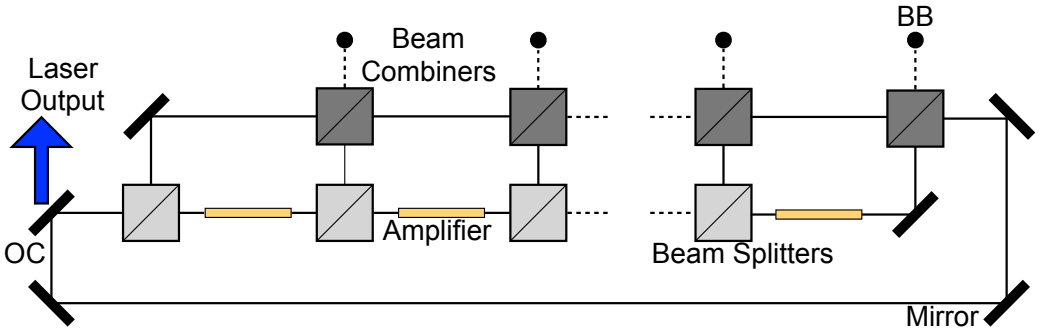

FIGURE 1.12: Scheme of the proposed multi-gain interferometric laser cavity (*Deposited Patent*: **DISPOSITIVO LASER A GUADAGNO INTERFEROMETRICO**).

The final idea is schematized in figure 1.12 and consists in a sequential cascade of ISAs within a common resonator structure. The cascade can achieve a laser power scaling, that ideally increases with the number of emitters. With respect to other types of combining architectures the idea, here presented, is based on a unique laser source, where both the beam quality and the spectral emission are not degraded by the increase in the number of emitters. Indeed, the laser characteristics depend only on the properties of the individual element and on the cavity structure. Furthermore, the common external cavity scheme self-adjust the interference condition so to maximize the laser performances.
This thesis is divided in five chapters the following way. After this introduction, **Chapter 2** presents the main properties of the semiconductor amplifier, which is the key element in the proposed. The experimental characterization of the used device is also reported in this chapter. **Chapter 3** describes the working principle of an ISA. Both the theoretical framework and the experimental characterization are presented. The following chapters are devoted to the laser system. **Chapter 4** first describes the passive resonator scheme employed in the realized laser. Both the simulation and experimental result of an external cavity semiconductor laser are here presented. Finally, **Chapter 5** in entirely dedicated to the interferometric laser. The power scaling architecture is presented and the first experimental results validating the whole idea are shown. **Chapter 6** draws the conclusions and gives some ideas for the future perspective of this work.

Chapter 2

Semiconductor Optical Amplifier

An optical amplifier is a device capable of amplifying coherently an optical input signal. In a Semicondutor Optical Amplifier (SOA), the population inversion is achieved in a semiconductor. Typically, this is obtained by current injection in a forward biased p-n junction. This chapter describes the working principle of a SOA and presents its main properties. Finally, the experimental characterization of the used SOA device is shown.

2.1 Traveling-wave SOA

The SOA is based on a forward biased p-n junction, to inject the high density of carriers, needed for the population inversion. The steady state excess carrier concentration Δn is related to the injection current density J, according to [70]

$$\Delta N = \frac{\tau}{el} J \tag{2.1}$$

where τ is the carrier lifetime including both radiative and nonradiative recombination process, e is the electron charge while l the SOA length.
To achieve a high optical confinement within the active region, the design of the SOA was first improved by the use of a double heterojunction (DH). This consists of a narrow band gap semiconductor, which can be either intrinsic or doped, placed between two higher gap p-type and n-type semiconductors. In this way, carrier injection is confined in the low band gap material. Since this last is the one responsible for the light amplification, it is called active region. At the same time, the high band gap materials have a lower refractive index than the active region; a slab waveguide is thus formed where the optical mode is confined.
From the semiconductor theory[1] it can be shown that the gain coefficient of the active region, at a frequency ν is given by the following formula[71]

$$\gamma(\nu) = \frac{c^2}{\nu^2 \tau_r 8\pi n^2} \frac{(2m_r)^{3/2}}{\pi\hbar^2} \sqrt{h\nu - E_g}\,[f_c(\nu) - f_v(\nu)] \tag{2.2}$$

where

Light speed in vacuum c
Radiative carrier recombination lifetime τ_r
Refractive index of the active region n
Reduced mass [72] m_r

[1] See Appendix A for more details

Planck constant h
Band-Gap energy [2] E_g
Fermi distribution respectively in the conduction and valence band f_c,f_v .

The fraction of mode propagating in the waveguide is given by the confinement factor, Γ. For a three layer slab waveguide, the confinement factor is found to be [74]

$$\Gamma = \frac{k_0^2 \left(n_1^2 - n_2^2\right) d^2}{2 + k_0^2 \left(n_1^2 - n_2^2\right) d^2} \tag{2.3}$$

where d is the active region thickness, while n_1 and n_2 refer to the refractive indexes of the cladding and of the core materials. Typical values of the active region thickness range from $0.1\mu m$ to $0.5\mu m$. The polarization sensitivity characteristics of a SOA depends on the different confinement factor, experienced by the TE and TM modes. The optical confinement influences also the gain coefficient, which becomes

$$\gamma_m = \Gamma\gamma \tag{2.4}$$

and it is referred to as the modal gain.
A typical schematic of a SOA chip is depicted in fig. 2.1.

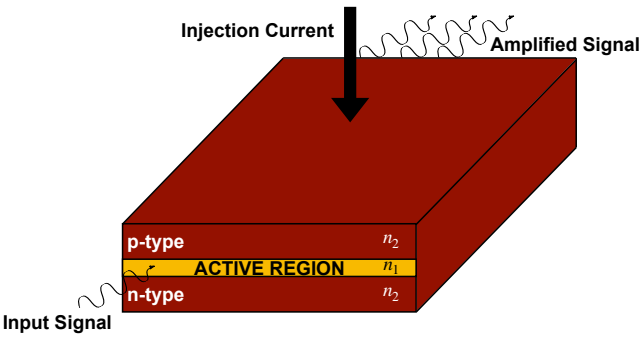

FIGURE 2.1: Schematic of a SOA

SOAs can be classified into two categories, the Fabry-Perot (FP) amplifier and the traveling-wave (TW) amplifier. The difference between the two is related to the reflectivity of the end facets of the waveguide. The input and output facets of a FP amplifier shows a residual reflectivity. The SOA acts as a Fabry-Perot Cavity, and the amplification is achieved only for the resonant modes of the cavity. This results in a very large optical gain for wavelengths corresponding to the cavity modes and a smaller gain for wavelength between two adjacent resonances. This gain modulation is usually unwanted for the majority of applications and the TW amplifier is preferred. The facets of a TW amplifier exhibit a negligible reflectivity and the input signal is amplified during a single pass. The gain spectrum is quite smooth and broad.
Finally, the active region normally contains quantum wells. Such amplifiers are called Multi-Quantum Well Amplifiers (MQW-SOAs). The active region consists of many quantum wells, separated by barrier levels, as schematized in fig. 2.2.

[2] For InGaAsP alloys, semiconductor material used in our SOA, E_G varies between $0.75eV$ and $1.36eV$ [73].

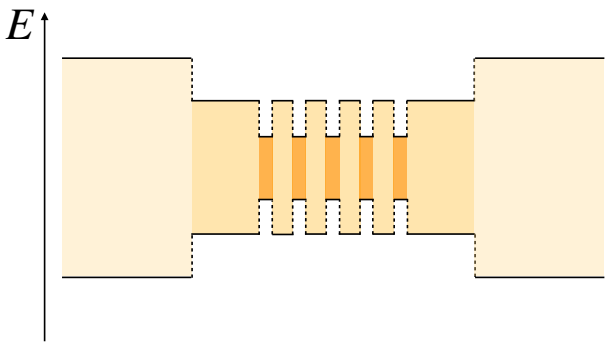

FIGURE 2.2: Schematic of the band diagram of the active region of Multi-Quantum Well SOA.

In these structures the carrier motion along the direction perpendicular to the layer is quantum confined. The energy levels in the conduction band are given by [75]

$$E(n, k_x, k_y) = E_n + \frac{\hbar^2}{2m_c}(k_x^2 + k_y^2) \tag{2.5}$$

where the index n refers to the n_{th} confined energy level, m_c is the reduced electron mass, k_x and k_y the wave vectors in the x and y directions and $E_n = \hbar^2(n\pi/L_z)^2/2m_c$, with L_z being the quantum well thickness. Similar considerations hold for the valence band. The discrete energy levels modify the optical joint density of states of the system. This last, according to the theory reported in Appendix A, influences the gain coefficient. Therefore, eq. 2.2, for a MQW SOA, transforms into

$$\gamma(\nu) = \frac{1}{c^2} 4\nu^2 \pi n^2 \frac{m_r}{\hbar L_z} [f_c(\nu) - f_v(\nu)] \sum_n H(h\nu - h\nu_n) \tag{2.6}$$

where $H(x)$ is the Heaviside step function.
A MQW SOA exhibits both a higher gain and a higher saturation power if compared to a DH SOA. As a drawback the optical gain exhibits a strong polarization dependence, with gain for TM modes rather low.
The complex dependence of the gain coefficient [76] on the injected carrier concentration ΔN makes the analysis of the SOA rather complicated. An empirical approach is adopted in which the maximum value of the gain coefficient, γ_p is assumed to be linearly related to ΔN [74], according to

$$\gamma_p \approx \Delta N - \Delta N_T \tag{2.7}$$

where ΔN_T is the injected carrier concentration at which the semiconductor is transparent.

2.2 Gain saturation

The gain coefficients in eqs. 2.2, 2.6 are referred to small-signal gain coefficient. For higher photon flux in the SOA, gain saturation takes place. This phenomenon is associated to a net decrease of the carrier population, because of the large number of stimulated emissions. From eq. 2.7 a reduction in ΔN causes a reduction in the gain coefficient.

To quantify this effect, let us consider a simple atomic system, where the two lasing levels are indicated by 1 and 2. For such a system the gain coefficient is given by [70]

$$\gamma(\nu) = (N_2 - N_1)\frac{c^2}{8\nu^2\pi n_r^2\tau_{sp}}\, g(\nu) \tag{2.8}$$

where τ_{sp} indicates the recombination lifetime due to the spontaneous transitions, while $g(\nu)$ refers to the atomic lineshape function. N_1 and N_2 are the population density respectively of the lower and higher energy levels involved in the transition.

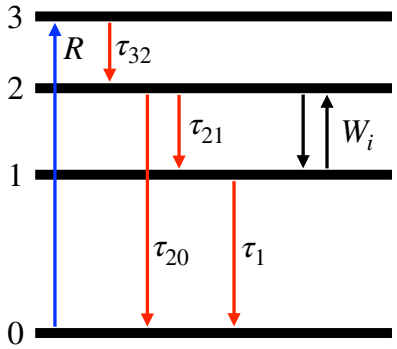

FIGURE 2.3: Energy level and transitions in a four level laser system. The total lifetime of the level 2 is τ_2, where $1/\tau_2 = 1/\tau_{20} + 1/\tau_{21}$. The decay from level 3 to level 2 is taken to be instaneous so that pumping to level 3 is equivalent to pumping to level 2.

The time evolution of both the two population densities is described by the rate equations, which account for the injection rates and the spontaneous and stimulated transition rates (reported in fig. 2.3)

$$\begin{aligned}\frac{dN_2}{dt} &= R - \frac{N_2}{\tau_2} - (N_2 - N_1)W_i \\ \frac{dN_1}{dt} &= -\frac{N_1}{\tau_1} + \frac{N_2}{\tau_{21}} + (N_2 - N_1)W_i\end{aligned} \tag{2.9}$$

where R refers to the external pumping rate, populating the higher energy levels. N_2/t_2 and N_1/t_1 indicates the recombination rates towards lower levels. N_2/τ_{21} describes the spontaneous transition rate from level 2 to level 1. It includes both the radiative and nonradiative contribution. This last in most systems is negligible and $\tau_{21} \approx \tau_{sp}$. $N_2 W_i$ refers to the stimulated emission transition rate, while $N_1 W_I$ indicates the induced absorption rate[3]. At steady state condition, the population densities are constant with time, $dN/dt = 0$ and eqs. 2.9 reduce to

$$\begin{aligned}\Delta N = N_2 - N_1 = \frac{R\tau_2 - (\tau_2/\tau_{sp}R)\tau_1}{1 + \left[\tau_2 + (1 - \tau_2/\tau_{sp})\tau_1\right] W_i} = \\ = \frac{\Delta N_0}{1 + \tau_s\, W_i}\end{aligned} \tag{2.10}$$

where $\Delta N_0 = R\tau_2 - (\tau_2/\tau_{sp}R)\tau_1$ is the population inversion density in absence of the optical field, when $W_i = 0$, and $\tau_s = \left[\tau_2 + (1 - \tau_2/\tau_{sp})\tau_1\right]$.

[3]For a monochromatic optical field of frequency ν and intensity I, $W_i = I\,\frac{g(\nu)\,c^2}{8\pi n^2 h\nu^3\tau_{sp}}$

Finally eq. 2.10 can also be written as

$$\Delta N = \frac{\Delta N_0}{1 + I_0/I_s} \tag{2.11}$$

where

$$I_s = \frac{8\pi n^2 h\nu}{\tau_s/\tau_{sp}\lambda^2 g(\nu)} \tag{2.12}$$

is a material parameter called saturation intensity and corresponds to the intensity level at which ΔN is reduced at half the small signal value ΔN_0.
From eq. 2.8, it follows that the gain coefficient shows the same intensity dependence

$$\gamma(\nu) = \frac{\gamma_0(\nu)}{1 + I_0/I_s} \tag{2.13}$$

where for a simple two level system

$$\gamma_0 = \frac{\Delta N_0 \lambda^2}{8\pi n_r^2 \tau_{sp}}\, g(\nu) \tag{2.14}$$

is called the small-signal gain coefficient.
The last equality holds only for homogeneous system, where all the atoms can be considered equivalent. In an inhomogeneous atomic system, individual atoms are distinguishable and have a unique energy transition. The whole system can be thought as consisting of collections of atoms, each of them behaving as a homogeneously broadened medium. The overall lineshape function counts for the contributions of all the different subset of atoms and it is defined by [70]

$$g(\nu)d\nu = \left[\int_{-\infty}^{+\infty} p(\xi) g^{\xi}(\nu) d\xi\right] d\nu \tag{2.15}$$

where $g^{\xi}(\nu)$ refers to the lineshape function describing the subset of atoms ξ, while $p(\xi)$ indicates the probability of finding an atom in the subset ξ.
The solution of the rate equations, relative to the subset ξ, yields

$$\Delta N^{\xi} = \frac{N_0 p(\xi)}{1 + \tau_s W_i^{\xi}(\nu)} \tag{2.16}$$

From this result, it can be demonstrated [70] that the gain coefficient is given by

$$\gamma(\nu) = \frac{\Delta N_0 c^2/\nu^2 \Delta\nu}{16\pi n^2} \int_{-\infty}^{+\infty} \frac{p(\nu_\xi) d\nu_\xi}{(\nu - \nu_\xi)^2 + (\Delta\nu)^2 + (\tau_s \lambda^2 I_0 \Delta\nu/16\pi^2 n^2 h\nu)} \tag{2.17}$$

The integration leads to

$$\gamma(\nu) = \frac{\gamma_0(\nu)}{\sqrt{1 + I_0/I_s}} \tag{2.18}$$

where I_s it the saturation intensity.
The comparison of the equations describing the gain saturation mechanism for both

an homogeneous and inhomogeneous broadened medium, shows that the decrease in the gain coefficient happens faster for the former.
The total power gained from an optical amplifier, P, can be found by solving the following differential equation, integrating it for the whole length of the amplifier, L.

$$\frac{dP}{dz} = \gamma P \tag{2.19}$$

where γ is given by eq. 2.13 or by eq. 2.18 depending on the material, and the frequency dependence has been neglected for simplicity.
Eq. 2.19 can only be solved in two limiting cases. When $P << P_s$, the gain saturation can be neglected, the gain is the small gain coefficient and the solution of the differential equation is given by the following simple formula

$$\ln\left[\frac{P_L}{P_0}\right] = \gamma_0 L \tag{2.20}$$

from which it follows that $P_L = e^{\gamma_0 L} P_0 = G P_0$, where G is the optical gain.
When $P >> P_s$, the gain operates under heavily saturated conditions and the solution of eq. 2.19 leads to the following expression for the power at the output of the amplifier

$$P_L = P_0 + \gamma_0 P_s L \tag{2.21}$$

The active medium simply increases the incident power by a constant signal, independent of the amplifier input.
For all the remaining cases eq. 2.19, has to be solved numerically. Besides the use of standard differential equation solvers, we developed a simple way to numerically evaluate the amplified power. This last consists in dividing the amplifier into N segments, each of them L/N long and with a small signal gain coefficient equal to $\gamma_0^N = \gamma_0/N$, as sketched in fig. 2.4.

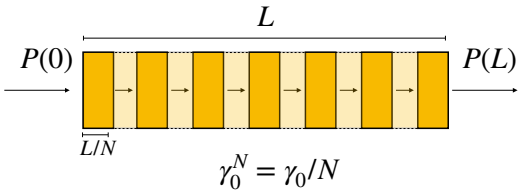

FIGURE 2.4: Sketch of the amplifier division into several segments for the numerical model implementation.

The gained power at each step will be the input power of the subsequent segment. If the number of steps is sufficiently large, the power at the output of the chain corresponds to the power gained from the entire amplifier. Fig. 2.5a shows that the error of this simplified model with respect to a standard solver is negligible when $N > 100$. Furthermore, fig. 2.5b shows that the computational time employed by the model remains orders of magnitude lower than the one employed by a differential equation solver, also for higher values of N.
Finally, figure 2.6 shows the gain as a function of the input power, obtained by the numerical solution of eq. 2.19, for an amplifier with a small signal gain equal to

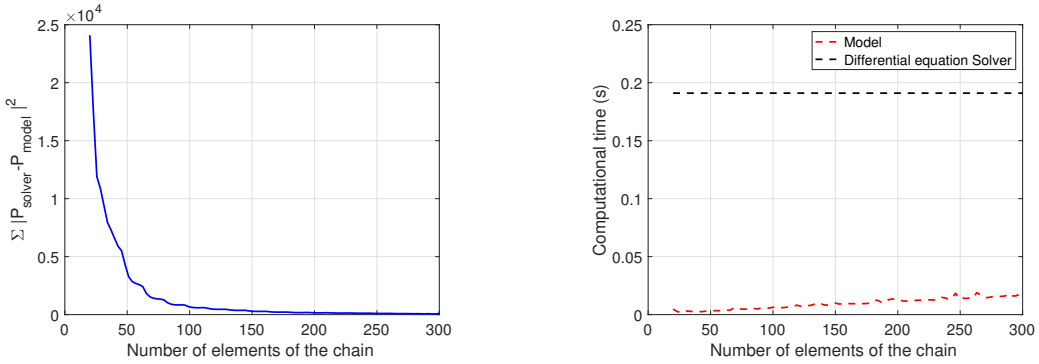

(A) (B)

FIGURE 2.5: (a): Error of the proposed numerical approximation with respect to the solution obtained from a standard differential equation solver, as a function of the number of segments in which the gain medium has been divided. (b): The red dashed curve indicates the computational time of the proposed approximation, while the black dashed curve refers to the time employed by a commercial differential equation solver.

$G_0 = 30dB$ and a saturation power of $P_s = 18dBm$.

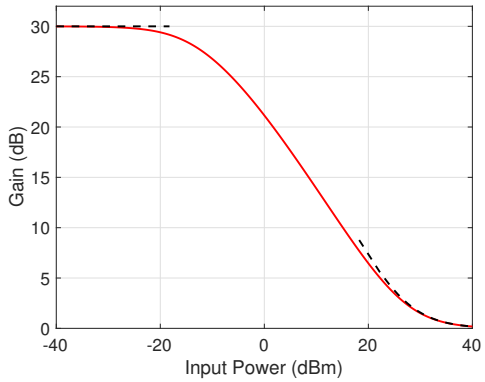

FIGURE 2.6: Gain saturation as a function of the input power of the amplifier. The black dashed lines indicate the two limiting case for which an analytical solution is possible.

For a SOA the rate equations for the carrier density $N(z)$ assumes the following form [70]

$$\frac{d\Delta N}{dt} = \frac{I}{eV} - R_{rec} - a(\Delta N - \Delta N_T)\, P \tag{2.22}$$

where I refers to the injection current, while $V = LA$ is the volume of the active region. R_{rec} is the transition rate that accounts for both radiative and nonradiative recombination processes, depleting the carriers. Finally, a is a temporal growth coefficient while P denotes the photon power inside the active region. This last is obtained by the following differential equation

$$\frac{dP}{dt} = \Gamma a(\Delta N - \Delta N_T)\, P - \frac{P}{\tau_p} \tag{2.23}$$

with τ_p being the photon lifetime The solution of eqs. 2.22 and 2.23 in the steady-state condition leads to the results obtained for the simpler atomic system. The main difference regards the saturation power, which for a SOA depends also on the carrier recombination rates, on the waveguide geometry and on the confinement factor.

2.3 Design for lateral confinement

The amplifier design is crucial for a further increase of the overall performance of the device. An important contribution to the SOA losses result from the spread of the optical energy in the regions outside the active layer. These last are quantified by the confinement factor Γ, previously introduced in eq. 2.3 for a 3 layer slab waveguide. Different strategies can be adopted to control the carrier and the light confinement. In gain-guided SOA lateral variations of the gain are used for the confinement, while index-guided design exploits the refractive index variation to confine light and carriers. The chip design also influences the modal distribution of the optical field propagating in the active waveguide.
The geometry of the SOAs used in this thesis consists of a ridge waveguide (RW). A schematic of the SOA cross section is shown in fig. 2.7.

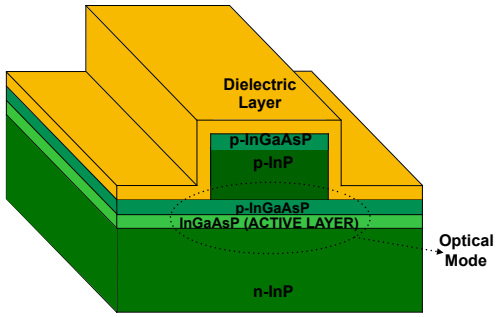

FIGURE 2.7: Schematic diagram of the cross a ridge SOA

Because the current injection is limited to the active region beneath the ridge, a good lateral confinement can be achieved. The optical waveguiding occurs because of the difference between the refractive indexes of the semiconductor materials ($\sim$ 3.2 to 3.5) and of the dielectric layer (typically SiO_2 or Si_3N_4 and $\sim$ 1.5 to 1.8)[75] on the sides of the ridge. RW SOA also operates in a single spatial mode.
The fabrication process of RW SOA is relatively simple and involves one epitaxial growth, followed by the rigde etching. Finally the metal contacts are deposited and the end facets are cleaved and coated.

2.4 Facet design for low reflectivity SOA

In a ideal TW SOA, the facet reflectivity of the amplifier should be less than 0.01%. Because of the large refractive index of semiconductors, the facet reflectivity is very high. Fig. 2.8 shows the facet reflectivity as a function of the refractive index for

several semiconductor materials.

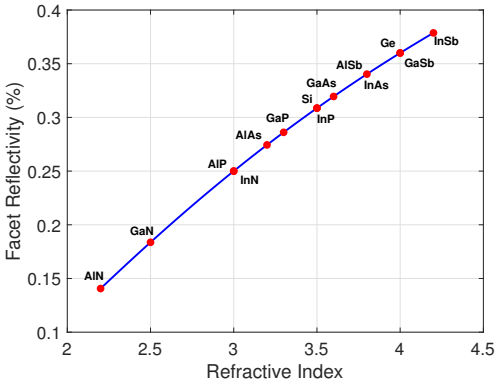

FIGURE 2.8: Reflectivity at the semiconductor facet due to the refractive index difference with the surrounding air. Results reported for photon energies closed to the bandgap energy and a temperature of $300K$. Adpated according to the results reported in [74].

Such high values of reflectivity can be reduced by an antireflection dielectric coating [77]. In addition, slanting the waveguide off the semiconductor facet avoids back coupling in the waveguide of the reflected optical mode. Figure 2.9 shows the principle of the tilted facet amplifier, which is used in this thesis.

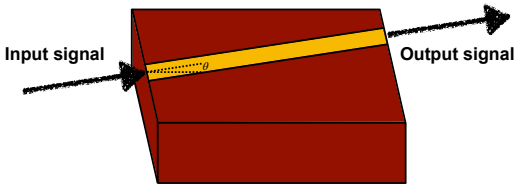

FIGURE 2.9: Schematic of the tilted facet amplifier.

Higher the tilting angle, higher will be the reflectivity reduction. Although, the increase of the tilting angle could lead to the excitation of the higher order modes and a compromise needs to be reached. The optimum design allows the achievement of optical gain as high as $30dB$ [75].

2.5 SOA characterization

The cavity design proposed and studied during this PhD work is based on commercial SOAs. For this reason, the first experimental tests were devoted to the characterization of the main properties of the purchased SOA.
The SOA is the BOA1007H model, sold by Thorlabs [78], and consists of an highly efficient InP/InGaAsP Quantum Well (QW) structure. The chip is mounted onto an heatsink, as reported in fig. 2.10a, to further protect the amplifier from the degradation effects associated with high temperature. The optical mode confinement is achieved thanks to a ridge waveguide, which is tilted with respect to the amplifier facets, shown in fig. 2.10b, to lower the residual reflectivity. The current is applied to

the anode and cathode of amplifier through wires bonding, also visible in the photo.

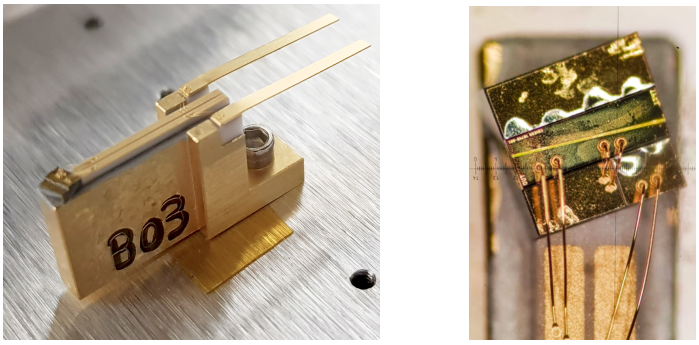

(A) (B)

FIGURE 2.10: (a): Photo of the amplifier with its heatsink. (b) Top view of the amplifier chip. It can be noted the tilted waveguide.

Table 2.1 indicates the main specifications of the amplifier, reported by the vendor.

Amplifier Specs	**Typical Value**
Operating Current	$I = 600$ mA
Center Wavelength	$\lambda_c = 1550$ nm
Small Signal Gain	$G_0 = 30$ dB
Saturation Output Power [4]	$P_s = 18$ dBm
Chip Length	$L = 1.5$ mm
Waveguide Refractive Index	$n_r = 3.2$
Beam Divergence Angle Fast Axis	$\theta_{FA}^{FWHM} = 26° \div 42°$
Beam Divergence Angle Slow Axis	$\theta_{SA}^{FWHM} = 10° \div 30°$

TABLE 2.1: Vendor Specification of the SOA amplifier

2.5.1 Temperature control

Since the gain coefficient, and consequently the whole operation of the amplifier, strictly depends on the temperature of the amplifier junction[5], temperature of the the whole chip needs to be controlled. For this reason the amplifier was placed above a copper mount, under which a thermo-electric cooler (TEC) is placed. A second copper support was placed below the TEC, as sketched in fig. 2.11a. Then the whole system was fixed to an aluminum plate through two plastic holders, to avoid thermal bridges, and placed onto a rotational and three axis translation stage, as reported in fig. 2.11b.

[4]The saturation output power is defined as the output power at the exit of the amplifier when the saturated gain decrease to half of the small signal gain. The value is related to the saturation power through the following relation $P_s^{out} = \frac{G_0 \log 2}{G_0 - 2} P_s$ [79].

[5]Eq. 2.2

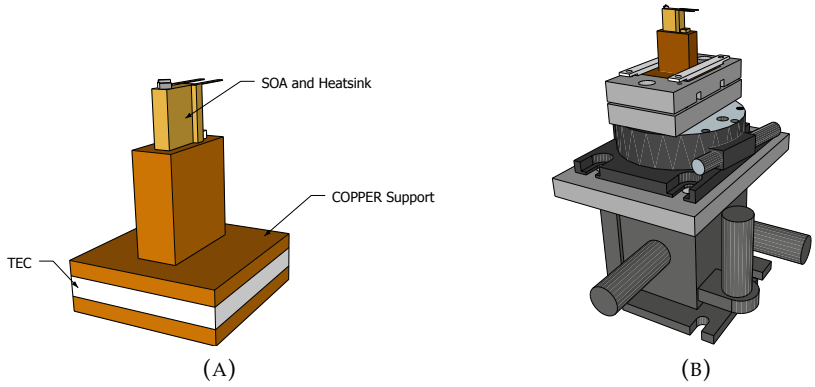

FIGURE 2.11: (a): Sketch of the mounting plates for the TEC stage. (b) Mechanical support of the amplifier.

The TEC is controlled via a driver module commanded through an evaluation board. The driver employs a proportional–integral–derivative (PID) controller which enables a fast temperature setting and a better stability of the temperature. The PID circuit controls in a feedback loop an error signal, which is the difference between the current temperature value and the set one. The error signal is sent to a control device, which in turn is fed back into the circuit. The result is an actively stabilization of the circuit which is able to operate at the set point value. The proper setting of the controls in the PID circuit depends on the environmental condition. Errors can cause severe oscillation in the system, leading to thermal instability.
The temperature is measured through a thermo-resistor of $10k\Omega$ and, typically is set at 20 °C. The measured variations are of the orders of $1mK$.

2.5.2 Optical beam

The rectangular shape of the amplifier active region cause the emission of an elliptical beam, reflecting the structure of the waveguide. The modes propagating into the waveguide are not exactly Gaussian modes, however a Gaussian approximation can still be used, with a negligible error [80]. Furthermore, the different dimensions of the ridge profile in the directions parallel and perpendicular to the active layer, influence the far field beam divergence, which is different for the two propagating directions. The axis for which the divergence is higher is called the fast axis, while the other is referred to as the slow axis, as represented in fig. 2.12.

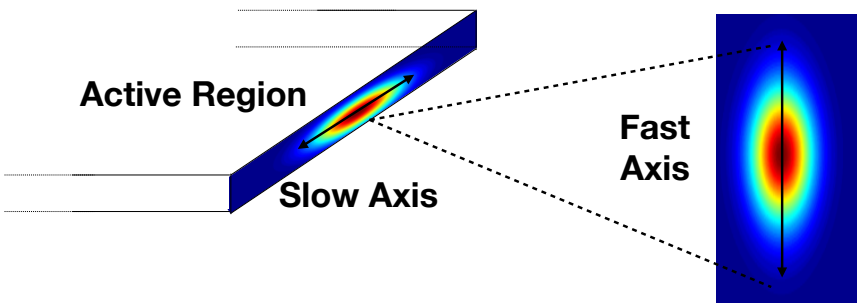

FIGURE 2.12: Computed beam profile emitted from a SOA in the near and far field. The emitted beam is elliptical and highly divergent.

Because of the very large divergence, optics is used to compensate them. Lenses are used to collect and collimate the light coming from the amplifier with an aspherical surface to correct for the spherical aberration and a numerical aperture (NA) higher than the SOA numerical aperture. This last is estimated as

$$NA_{SOA} \approx \sin(\theta_{FA}/2)^{6} \tag{2.24}$$

where θ_{FA} is the fast axis divergence.
A good strategy for choosing the collimation lens is to pick a lens with a NA at least twice of the NA of the emitted beam. Referring to the value reported from the amplifier vendor, a NA of approximately 0.3 was estimated, while the NA of the chosen lens was declared to be equal to 0.7. The beam profile was collected using a scanning-slit profiler. In the device, two slits scan subsequently along the two beam directions and across the full cross section of the beam. Then, the transmitted light is collected by a photodetector, for each position of the two slits. The intensity measurements are then used to reconstruct the beam profile. Figure 2.13 shows an example of the beam profile collected after the collimation lens.

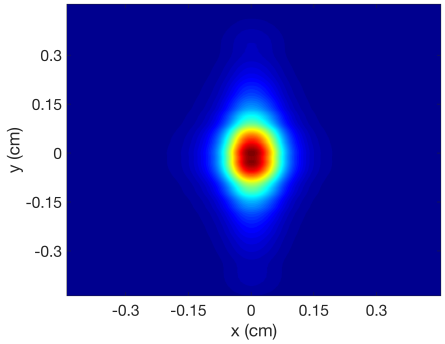

FIGURE 2.13: Schematic of the tilted facet amplifier.

2.5.3 Amplified spontaneous emission measurements

In a SOA, the photons emitted because of the spontaneous emission process undergo amplification. The emitted radiation is referred to Amplified Spontaneous Emission (ASE) and it is considered as a fundamental source of noise for the amplifier. Nevertheless, the ASE is also the radiation responsible for starting the laser operation. For this reason, the knowledge of the ASE of the amplifier is important to determine the properties of the laser emission.

The ASE emitted from the SOA is collected by the aspherical lens and send first to a thermal power sensor. Figure 2.14a shows the ASE optical power as function of the injection current on the SOA. The ASE power linearly increases with the injection current, as expected from eq. 2.7, for values of the injection current ranging from $\sim 100mA$ to $\sim 450mA$. For higher values of the driving current saturation effects

[6] Laser diode industry uses the FWHM divergent angle to specify the beam divergence, while in the optical community the $1/e^2$ intensity divergence is more often used. Here θ_{FA} refers to the full angle, while often the divergence half-angle is used.

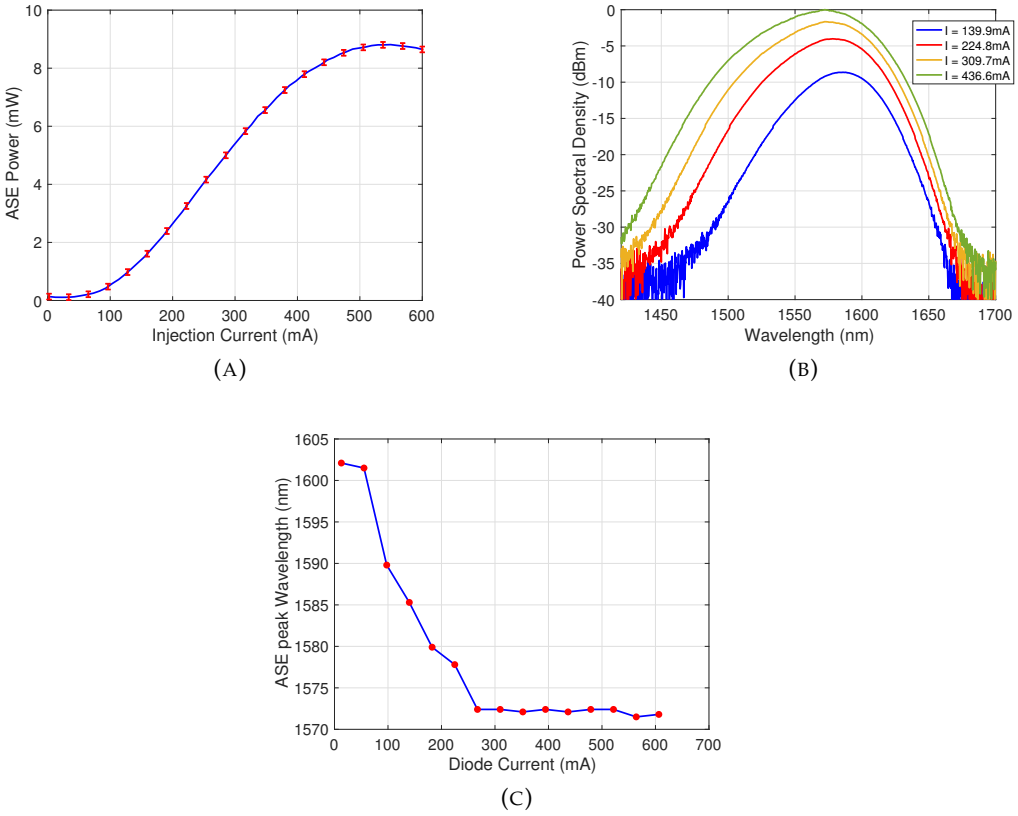

FIGURE 2.14: Experimental Results: (a): ASE Power as a function of the injection current. The errors associated with the experimental data are due to the sensitivity of the power meter. (b) Emission Spectra of the ASE, for different values of injection current. (c): ASE peak wavelength as a function of the driving current.

occur.
Spectral measurements of the ASE were done by coupling the light to the fiber, which in turn is coupled to an Optical Spectrum Analyzer (OSA). The measurements were taken with a resolution of $1nm$ and a Video Bandwidht (VBM) of $1KHz$. Figure 2.14b shows the emission spectra collected for different values of the injected current.
The ASE spectra, as clearly visible in fig. 2.14c shifts toward shorter wavelength with the increase of the injection current. This is caused by the band-filling effect [81] caused, in turn, by the increase in the carrier density, with the injection current.

2.5.4 Gain measurements

Fundamental for the correct modeling of the laser performance is the determination of the gain saturation behavior of the SOA. Figure 2.15a shows a sketch of the experimental set-up.
An external pigtailed laser is sent to a Variable Optical Attenuator, VOA to continuously vary the power of the input signal. In our set-up the VIAVI Multiple Application Platform MAP-200 VOA was used. Because of the polarization dependence of the SOA gain, the signal is sent to a polarization controlling stage, to control the input light polarization. The light is coupled in the SOA. Because of the small dimension of the active region, the coupling lens is mounted on micro-translators to

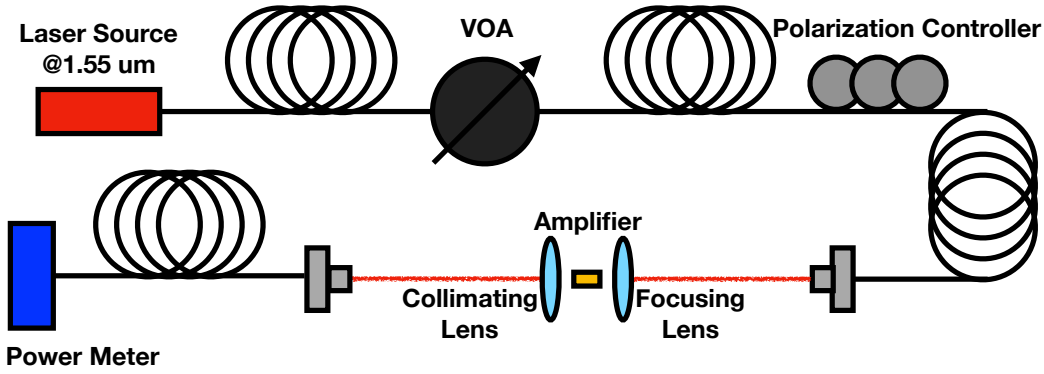

(A)

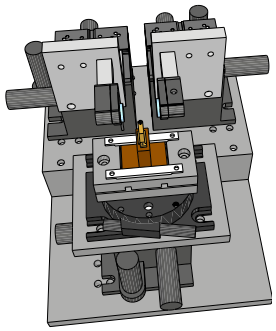

(B)

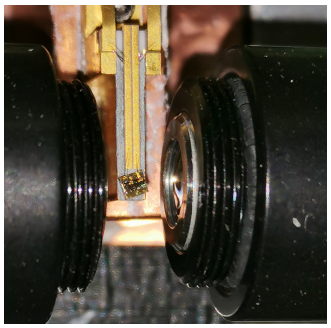

(C)

FIGURE 2.15: (a): Scheme of the experimental set-up. (b) CAD of the Gain Block. (c) Image of the coupling stage.

optimize the coupling. This lens was a focusing aspherical lens, whose effective focal length is $f_{ef} \approx 3.15mm$. The high divergent amplified beam, exiting from the amplifier, is collected through a second aspherical lens, fiber coupled and sent to a VIAVI MAP Optical Power Meter module. The collection of the SOA and the two lenses will be referred to as gain block in the following. Figure 2.15b shows a 3D cad of the realized support where the gain block is visible, while fig. 2.15b reports a photo which shows a detail of the gain block with the two mounted lenses.
The minimum detectable power from the VIAVI power meter is equal to $-100dBm$, while the maximum power that can be send to the instrument is equal to $13dBm$. To avoid damages of the sensor, neutral density filters were placed in front of the power meter. The coupling losses were measured for each current value, when the VOA attenuation was equal to $0dB$. The measured losses are reported in fig. 2.16.
The different values of losses, with the injected current in the SOA, can be attributed to variations in the beam profile which alters the coupling condition or to misalignment during the measure.
Figure 2.17a shows the measured output power as a function of the input power on the SOA, while fig. 2.17b reports the gain of the SOA as a function of the measured output power, for different values of the injection current
The gain saturation behavior is clearly visible. For low values of input power, the gain is equal to the small signal gain. This last slightly differs from the value reported from the vendor, in table 2.1, and can be attributed to some differences in the coupling of the input signal with the SOA and in the collection of the amplified signal.

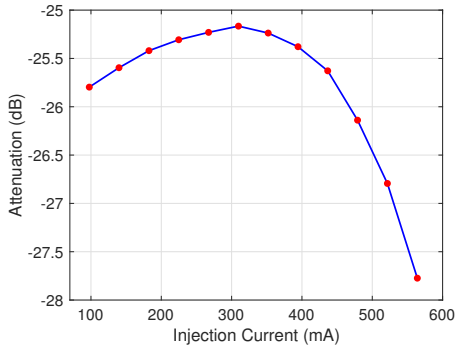

FIGURE 2.16: Coupling losses between the VIAVI power meter and the amplified signal.

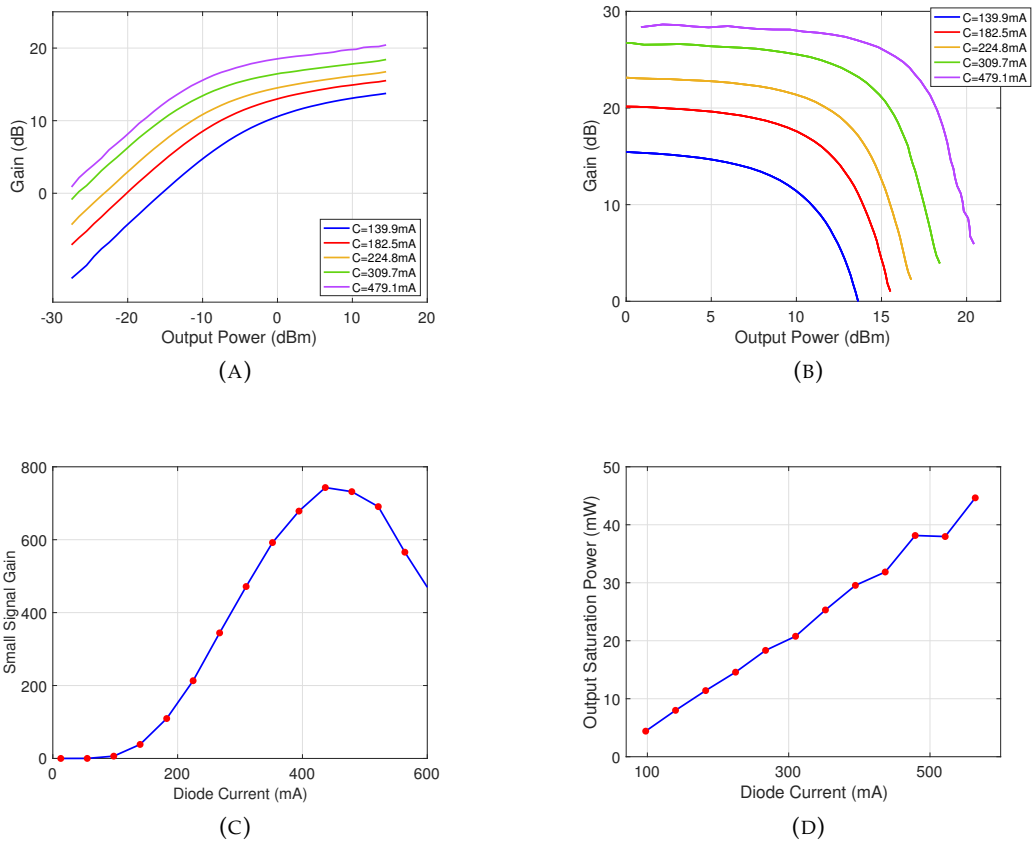

FIGURE 2.17: Experimental Result: (a) Measured output power as a function of the input power. (b): Gain curves as a function of the measured output power, for different values of the injection current. The experimental data are corrected for the coupling losses at the power meter. The error bars are contained within the red dotted points. (c): Small signal gain as a function of the injection current. (d): Saturation output power as a function of the injection current.

Figure 2.17c shows the small signal gain, G_0, dependence on the injection current. The measured behavior is similar to the one observed for the ASE power (fig. 2.14a). G_0 linearly increase with the current, as soon the current reaches the value at which the transparency condition is achieved, which is approximately equal to $\sim 100mA$.

Also in this case, for driving current higher than $\sim 450mA$ saturation effects occur. In fig. 2.17d, the changes in the saturation output power with the injected current are reported. A clear linear dependence is visible.

2.6 Nonlinear gain compression

Figure 2.6 reports a comparison between a measured gain curve and the one obtained by the numerical solution of the differential equation in eq. 2.19 (see fig. 2.6). It is observed a disagreement between the experimental results and the theoretical predictions for large output powers.

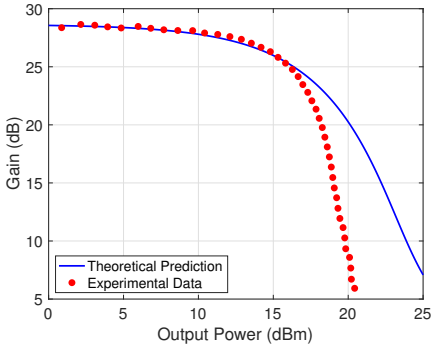

FIGURE 2.18: Comparison between the experimental data and the theoretical model.

This deviation can be attributed to the so called nonlinear gain compression, typical in SOA [82]. The exact origin of this gain nonlinearity is not fully understood and furthermore difficult to measure in an experiment. Among the possible reasons there are Spectral Hole Burning (SHB), Carrier Heating (CH), two-photon absorption (TPA) and two-photon induced free carrier absorption (FCA) [83]. The nonlinear behavior is caused by the carrier generated because of one of these phenomena. Furthermore, it is important to underline that, because of the Kramers-Kronig relation [84], also the semiconductor refractive index is influenced by the variation of the carrier density [85].
To identify the phenomenon responsible for the gain nonlinearity in our SOA, we analyzed separately the contribution imparted by SBH or CH and the one imparted by both TPA and FCA.
SHB refers to the formation of a dip in the gain spectrum. The phenomenon is caused by the instantaneous carrier depletion due to a high power signal. The consequent carrier recombination fills the empty states of the band through scattering process. The characteristic time scale of the whole process is around $100fs$. On the other hand, CH describes the fact that under non equilibrium condition the carrier temperature, appearing in the Fermi distribution function, may be different from the crystal lattice temperature. The temperature increase causes a redistribution of the carriers which relax back to the crystal temperature on a timescale of $1ps$. Typically the two phenomena are described multiplying the constant a in Eqs. 2.22, 2.23 by the gain scaling factor [86]

$$f(P) = 1 - \epsilon P \tag{2.25}$$

to represent an equivalent gain saturation. The value of ϵ is a phenomenological parameter, usually experimentally evaluated.
In this work we followed the work in [87] to evaluate the nonlinear contribution in the gain coefficient. The carrier relaxation, caused by one, or both, of the phenomena mentioned above, is described within the density-matrix formalism and approximated as a transition, of frequency ω_T, of a single two level system. The response of the semiconductor to the applied optical field, is expressed by the susceptibility in the form

$$\chi = -\int_a^{\infty} \frac{1+\Delta^2}{1+\Delta^2+P} \quad \frac{f(\Delta)}{\Delta - i}\, d\Delta \tag{2.26}$$

where Δ indicates the detuning between the transition frequency, ω_T and the optical field frequency, ω_0, defined as

$$\Delta = (\omega_T - \omega_0)\tau_{rel} \tag{2.27}$$

where τ_{rel} stands for the carrier relaxation time. The function $f(\Delta)$ depends on the density matrix elements, which describes the system[7]. Finally, the lower limit of integration is defined as $a = (\omega_g - \omega_0)\tau_{rel}$, where ω_g refers to the band gap frequency. The susceptibility is expressed as the sum of a linear and a nonlinear contribution, $\chi = \chi_L + \chi_{NL}$. The two are both related to the linear and nonlinear gain, via the following expression

$$\chi = 2n(\Delta n - i\frac{\gamma}{2k_0}) \tag{2.28}$$

where k_0 is the wavevector while Δn express the refractive index changes that accompanies the gain, γ.
Using the analytical approach described in [87], to solve the complex integral in eq. 2.26, it is possible to obtain an approximate form for both the linear and nonlinear susceptibility. From this result, the following relation between the linear, γ_L and nonlinear gain, γ_{NL} can be easily determined,

$$\gamma_{NL} = -\frac{\gamma_L^{'}\, P/P_s}{\sqrt{1+P/P_s}(1+\sqrt{1+P/P_s})} \tag{2.29}$$

where $\gamma_L^{'}$ is the saturated gain given by eq. 2.18. The total gain coefficient is the sum of the contributions, $\gamma_T = \gamma_L + \gamma_{NL}$, where γ_L is the saturated gain given by eq. 2.13.
In addition, it was suggested[87] that for input powers close to the saturation power, the gain departs from the value given by eq. 2.18. For this reason, the following expressions for the total gain coefficient were proposed

$$\begin{cases} \gamma_T = \dfrac{1}{1+P/P_s} & \mathrm{P} < \mathrm{P_s} \\ \gamma_T = \dfrac{1}{1+P/P_s}\left(1 - \dfrac{P/P_s}{(1+\sqrt{1+P/P_s})}\right) & \mathrm{P} \geq \mathrm{P_s} \end{cases} \tag{2.30}$$

[7] The reader can consult [88] for further details on the density matrix

where P indicates the input power on the SOA.
In eq. 2.30 we suggest that the nonlinear effects, associated with carrier relaxation, have an impact on the gain saturation when the signal power at the input of the amplifier is equal or overcome the saturation power. Under this condition, the gain saturates inhomogeneously.
Eq. 2.30 gives the gain coefficient, the total gain is found using the numerical approach outlined in section 2.2. Figure 2.19 compares the experimental results (dotted curves) with the theoretical prediction (solid curves), when the gain coefficient is the one expressed in eq. 2.30. The values of γ_0 and P_s used in the simulation model are those experimentally measured and reported in figs. 2.17b, 2.17c. A good agreement is clearly visible for different values of the injection current.

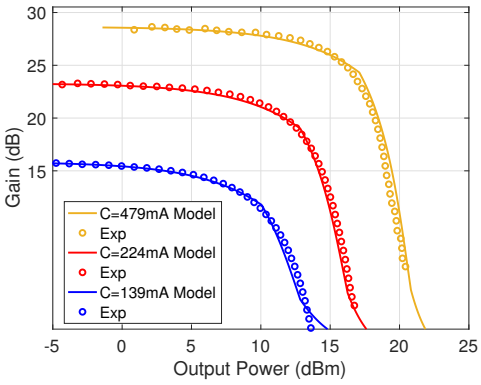

FIGURE 2.19: Comparison between the experimental data and the theoretical model.The dotted curves indicates the experimental data, while the solid curves are obtained by numerically solving the differential equation in eq. 2.19 when γ is the one in eq. 2.30. The different colors refers to different values of injection current.

The other possible process, for the nonlinear gain compression, is associated to TPA[89]. TPA is a nonlinear absorption process, characterized by the simultaneous absorption of two photons. This cause instantaneous transitions of electrons from the valence band to high energy states in the conduction band. TPA can be described by a power dependent absorption coefficient

$$\alpha_{TPA} = \frac{\beta_{TPA}}{A_m} P \tag{2.31}$$

with β_{TPA}, the two photon material coefficient, while A_m the beam modal area.
Furthermore, TPA causes a secondary loss mechanism resulting in the creation of free carriers (FC), whose absorption cause a further decrease of the amplified signal. By solving the rate equation governing the TPA process, it can be shown that in steady state conditions, the density of the generated FC is given by the following

$$n_{FC} = \frac{\beta_{TPA} P^2 \tau}{A_m^2 h\nu} \tag{2.32}$$

where τ is the lifetime of the TPA-generated carriers.Finally, the loss coefficient associated with FCA is given by

$$\alpha_{FCA} = \sigma_{FCA} n_{FC} \tag{2.33}$$

with σ_{FCA} being the FCA cross section of the TPA-generated carriers[89]. Eq. 2.33 can also be written as

$$\alpha_{FCA} = \frac{\beta_{FCA}}{A_m^2} P^2 \tag{2.34}$$

where

$$\beta_{FCA} = \frac{\beta_{TPA} \tau_{TPA}}{\sigma_{FCA} h\nu} \tag{2.35}$$

Considering both the TPA and FCA, the total gain coefficient of the amplifier can be expressed by

$$\begin{aligned} \gamma_T &= \gamma_L - \alpha_{TPA} - \alpha_{FCA} \\ &= \gamma - \frac{\beta_{TPA}}{A_m} P - \frac{\beta_{FCA}}{A_m^2} P^2 \end{aligned} \tag{2.36}$$

where γ is the saturated gain coefficient in eq. 2.18. Also in this case, the numerical approach presented in section 2.2 was used to evaluate the total gain, G.
The two loss coefficients were determined from the experimental data, by fitting the simulated total gain to the experimental gain. The fitting was performed using the optimization algorithm **ParticleSwarm** in *MATLAB*. Particle swarm is a population-based algorithm. The particles move within a the boundary region in steps. At each step the objective function is evaluated, until the best location is found. In our study this last corresponds the values of β_{TPA} and β_{FCA} that better fit the experimental results. The algorithm function tolerance, that expresses the relative changes in best objective function, was set equal to $1e-4$. Figure 2.20a shows the comparison between the theoretical model and the experimental data. Also in this case a good agreement is reached. In fig. 2.20b and in fig. 2.20c the values, returned from the optimization procedure, of the two loss coefficients divided by the modal area are reported.

From fig. 2.20b it appears that the obtained values of the TPA absorption coefficient, divided by the modal area, are scattered around a mean value. This is expected, since β_{TPA} is a material coefficient. The scattering of the data can be attributed to some errors in the measurements or to some variation in the the modal area. This last can be caused by some variations in the effective index, because of both temperature changes or carrier density variations, with the injection current. This variation could influence the waveguide mode which in turn changes the modal area. At the end, we can estimate $\beta_{TPA}/A_m \simeq (3.33 \pm 1.18) \times 10^{-5} (mW)^{-1}$. From the values of the beam divergence reported from the vendor, the modal area, defined as

$$A_m = \frac{\left(\int\int |E(x,y)|^2 dxdy\right)^2}{\int\int |E(x,y)|^4 dxdy} \tag{2.37}$$

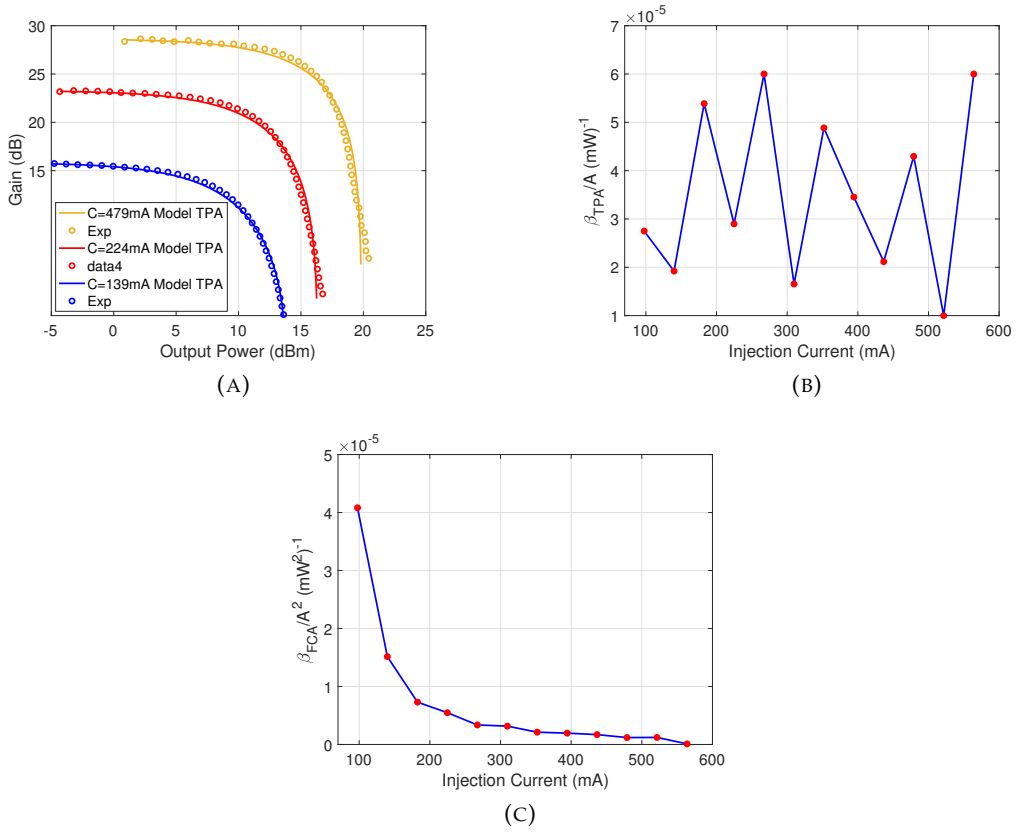

FIGURE 2.20: (a): Comparison between the experimental data and the theoretical model, based on eq. 2.36. The dotted curves indicates the experimental data, while the solid curves are obtained by the model of the SOA gain. The different colors refers to different values of injection current. (b): β_{TPA}/A_m vs the injection current, deduced by the fit. (c): β_{FCA}/A_m^2 vs the injection current, deduced by the fit.

can be assumed of the order of $10^{-7}m^2$. Therefore, an approximate value of $\beta_{TPA} \approx 3cm/GW$ is found. Typical values of the TPA absorption coefficients, reported in literature range around an higher order of magnitude with respect to the value here reported [89, 90].
The results reported in fig. 2.20c shows that β_{FCA}/Am^2 decreases with the increase of the injection current. This behavior is not fully understood. Because of the complexity of the carrier dynamics in semiconductor, the correct explanation needs the theoretical model explaining the interaction between the TPA-generated and the injected carrier.
The considerations made up to now, seem to prove the inappropriateness of the TPA model in the understanding of the experimental nonlinear gain compression. We can therefore suppose that the responsible process of the gain nonlinearity is either SHB or CH. The final prove should come from an experimental outcome. However, this last needs demanding experimental techniques. Among these, we mention pump and probe measurements. A pulsed pump source is to measure the time scale of the nonlinear saturation, which differs depending on the process[83]. For CW input signal the measurement of SOA photo-luminescence emitted radiation because of the nonlinear process can give more information on TPA[89].

Chapter 3

Interferometric Semiconductor Optical Amplifier

The Interferometric Optical Amplifier (ISA) represents one of the fundamental block of this thesis work. An ISA is realized by placing a SOA into one arm of an interferometer, which could be either a Michelson or a Mach-Zender interferometer [91]. This chapter presents the fundamental properties of an ISA, highlighting the major advantages and disadvantages in their use. The experimental characterization is also presented.

3.1 ISA modeling using a matrix approach

In our design, a semiconductor optical amplifier is placed into one arm of a Mach-Zender Interferometer (MZI).

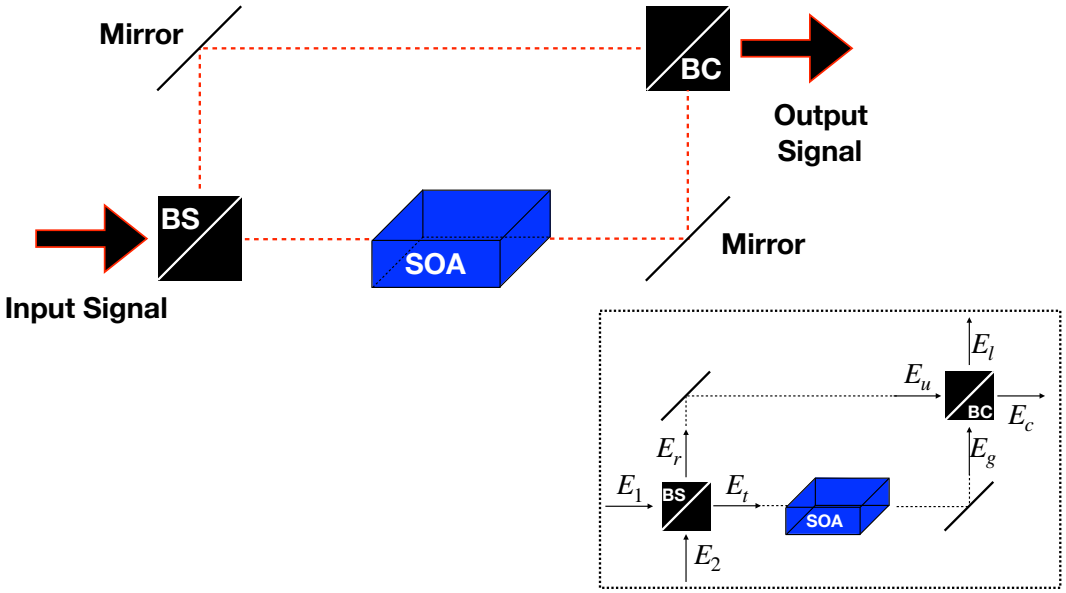

FIGURE 3.1: Scheme of the proposed ISA. The inset indicates the propagating fields. BS stands for the separating Beam Splitter, while BC indicates the Beam combiner

In literature [92] similar structures, containing amplifiers on both the arms of the interferometer, are used for scaling up the amplified power of an incoming optical field. The resulting output signal is the results of the constructive interference of

the fields, amplified by the two SOA. Other applications can be found in integrated optics, where SOAs incorporated into MZI or Michelson interferometer have been used for demultiplex high speed optical signals [93] or to realize optical logic AND gate [94].
A scheme of the proposed ISA, is reported in fig. 3.1, where the inset highlights the naming of the propagating fields. In the ISA here proposed, a portion of the incoming beam will travel unperturbed, while a second portion will undergo amplification. At the output port of the interferometer, the two beams will be coherently combined together by a second beam splitter, which acts as a beam combiner. The idea which motivates this thesis work, is to use the upper arm of the interferometer to reduce the amount of power incident on the SOA. This power reduction translates into a higher gain of the SOA. Furthermore, the use of a combination of beam splitters and beam combiners, allows the implementation of a cascade of sequential ISA, impossible with standard amplifiers, because of gain saturation.
To study the behavior of the ISA, the scattering matrix formalism was adopted. Here, optical elements and propagation are described by a specific matrix [74]. More in details, the fields at the input and at the output of the beam splitter, in fig. 3.1, are described by the following relation

$$\begin{pmatrix} E_t \\ E_r \end{pmatrix} = \begin{pmatrix} t_{bs} & i\,r_{bs} \\ i\,r_{bs} & t_{bs} \end{pmatrix} \begin{pmatrix} E_1 \\ E_2 \end{pmatrix} = \mathbf{R_{BS}} \begin{pmatrix} E_1 \\ E_2 \end{pmatrix} \tag{3.1}$$

where $|r_{bs}|^2 = R_{bs}$ and $|t_{bs}|^2 = T_{bs}$, such that $|r_{bs}|^2 + |t_{bs}|^2 = 1$, with R_{bs} being the beam splitter reflectivity.
The field propagation, described by the propagation constant k, in both the upper and the gain arms is described by

$$\begin{pmatrix} E_g \\ E_u \end{pmatrix} = \begin{pmatrix} i\sqrt{G}e^{-ikd_1}\, e^{-ikn\,L_g} & 0 \\ 0 & i\,e^{-ikd_2} \end{pmatrix} \begin{pmatrix} E_t \\ E_r \end{pmatrix} = \mathbf{P} \begin{pmatrix} E_t \\ E_r \end{pmatrix} \tag{3.2}$$

where d_1 and d_2 refer, respectively, to the lengths of the gain and upper arms, L_g indicates the active medium length, while n_r its refractive index. The active medium amplification on the signal field is described by the multiplication factor $\sqrt{G}$. The i factor accounts for the $\pi/2$ phase shift imparted by the plane mirrors.
The field relation at the beam combiner is described by

$$\begin{pmatrix} E_c \\ E_l \end{pmatrix} = \begin{pmatrix} i\,r_c & t_c \\ t_c & i\,r_c \end{pmatrix} \begin{pmatrix} E_g \\ E_u \end{pmatrix} = \mathbf{R_C} \begin{pmatrix} E_g \\ E_u \end{pmatrix} \tag{3.3}$$

Finally, the matrix describing the whole system is given by the product of the three individual matrices, and the relation between the input and the output fields of the ISA is found to be

$$\begin{pmatrix} E_c \\ E_l \end{pmatrix} = \mathbf{R_C}\,\mathbf{P}\,\mathbf{R_{BS}} \begin{pmatrix} E_1 \\ E_2 \end{pmatrix} = \mathbf{H} \begin{pmatrix} E_1 \\ E_2 \end{pmatrix} = \begin{pmatrix} hh_{11} & h_{12} \\ h_{21} & h_{22} \end{pmatrix} \begin{pmatrix} E_1 \\ E_2 \end{pmatrix} \tag{3.4}$$

In our scheme, we inject the signal $P_{in} = P_1$ at the entrance of the ISA and we look at the amplified beam at the straight ISA output port. Therefore, at the entrance of the initial beam splitter only the field E_1 is present. Then, we can compute the optical powers P_c and P_l

$$\begin{aligned} P_c = |E_c|^2 = |h_{11}E_1|^2 = |-\left[e^{-ik(d_1+n\,L_g)}\sqrt{G}t_{bs}r_c + e^{-ikd_2}t_c r_{bs}\right]|^2 P_1 \\ P_l = |E_l|^2 = |h_{21}E_1|^2 = |i\left[e^{-ik(d_1+n\,L_g)}\sqrt{G}t_{bs}t_c - e^{-ikd_2}r_c r_{bs}\right]|^2 P_1 \end{aligned} \tag{3.5}$$

Let us suppose for the moment that the interferometer is perfectly balanced in terms of the optical path, which means that $d_2 = d_1 + nL_g = d$. In this situation the fields propagating in the two separate paths interfere constructively. Eq. 3.5 simplifies into

$$\begin{aligned} P_c = |\left[\sqrt{G}t_{bs}r_c + t_c r_{bs}\right]|^2 P_1 \\ P_l = |\left[\sqrt{G}t_{bs}t_c - r_c r_{bs}\right]|^2 P_1 \end{aligned} \tag{3.6}$$

Ideally, we would like to have all the power only in one port of the beam combiner, $P_{out} = P_c$. This is equivalently to say that the combining efficiency between the two fields reaches 100%. Indeed P_l does not contributes to the amplified signal, and represents a source of losses. The optimum condition, $P_l = 0$, is achieved when $|h_{21}|^2 = 0$, or equivalently when

$$\frac{t_c}{r_c} = \frac{r_{bs}}{t_{bs}}\frac{1}{\sqrt{G}} \tag{3.7}$$

Therefore, the no loss condition imposes a well defined relation between the reflectivity of the beam splitter and of the combiner composing the interferometer, depending on the value of the total gain.
As evident from eq. 3.6, the ISA can be thought of as an effective active medium, giving an amplification to an incoming signal, such that the total output power is given by

$$P_{out} = P_c = G_{eff}\,P_{in} = |h_{11}|^2 P_{in} \tag{3.8}$$

where G_{eff} is called the ISA effective gain and describes the amplification factor of the signal power at the c port of the beam combiner.
Similarly, the amplification factor of the power at the l port is defined according to

$$P_l = L_{eff}\,P_{in} = |h_{21}|^2 P_{in} \tag{3.9}$$

and under the ideal condition is null.
Figures 3.2a and 3.2b show the behavior of the SOA gain, G, and of the ISA effective gain, G_{eff}, as a function of the output power of the amplifier, for different values of the beam splitter reflectivity.

The increase of the BS reflectivity means that at the same input signal, less power is sent to the SOA. As expected, the use of a higher beam splitter reflectivity implies a higher gain for the SOA amplifier, with respect to the standard behavior, for the same value of input power. As clearly visible in fig. 3.2a, the saturation behavior of the amplifier changes, and the saturation output power increases with the increase of the beam splitter reflectivity, as shown in fig. 3.2c. As a drawback, the increase of the beam splitter reflectivity decreases the effective gain, G_{eff}, especially for low

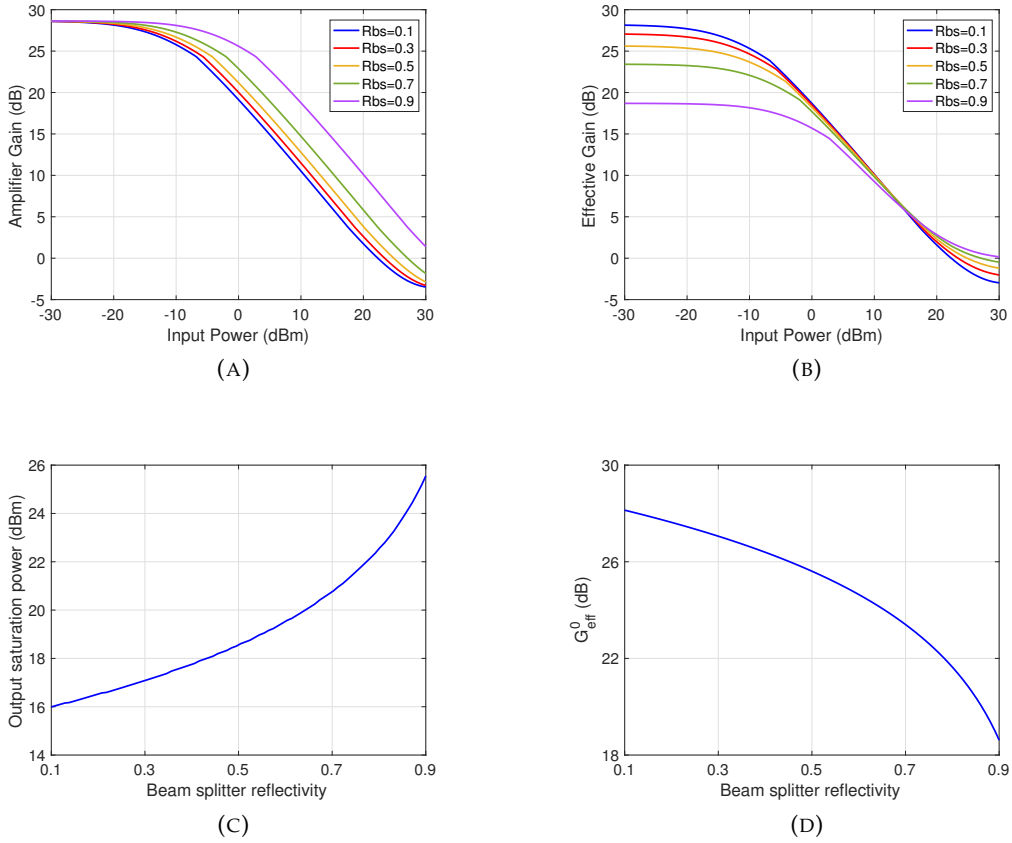

FIGURE 3.2: (a): SOA Gain in the ISA, as a function of the input power, for different values of the beam splitter reflectivity. (b) ISA effective gain, as a function of the input power, for different values of the beam splitter reflectivity. (c) SOA output saturation power as a function of the beam splitter reflectivity. (d) Small Signal Effective Gain as a function of the beam splitter reflectivity. The same injection current of $500mA$ was used in the SOA.

power input signals. As shown in fig. 3.2d, the small signal ISA effective gain, G^0_{eff}, decreases by increasing the beam splitter reflectivity. The reduction occurs because the portion of light undergoing amplification decreases and the power at the output of the amplifier reduces.
To summarize, the use of an higher value of beam splitter reflectivity shows a reduction of the overall performance of the amplifier with respect to the standard amplifier, for low power input signal. Nevertheless, the increase of the saturation output power improves the amplifier response to high power signal. Furthermore, this scheme offers two major advantages. First, all the degradation processes, occurring in the active medium, associated with high power are reduced. Secondly when the major portion of the beam travel unperturbed, the implementation of a sequential cascade of amplifier is possible.

3.2 Sequential cascade of ISAs

An example of a sequential cascade of ISAs is shown in fig. 3.3a. The whole sequence can be viewed as a unique effective active medium, whose amplification is

described by an effective gain, G^c_{eff}.

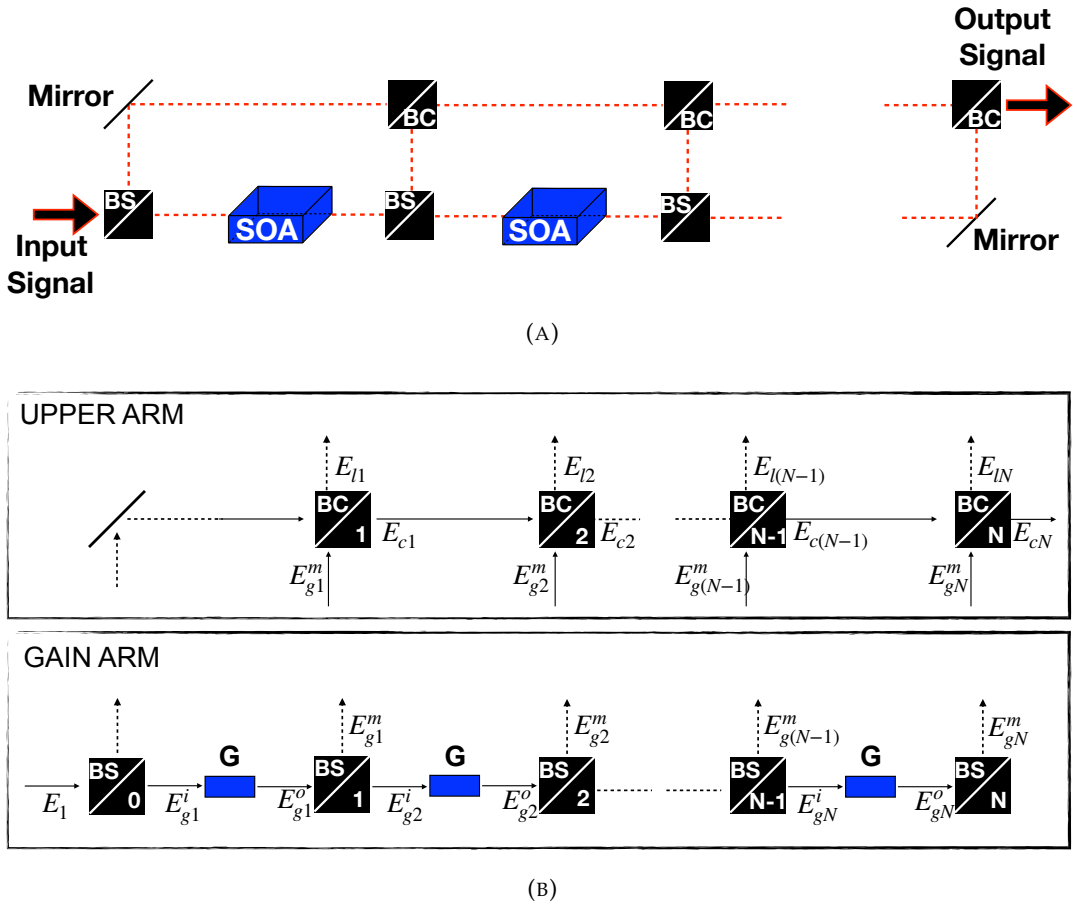

FIGURE 3.3: (a): Scheme of an ISAs sequence. (b) Details on the fields propagating in the ISA. The upper inset refers to the gain arm, while the lower inset to the upper arm.

To simplify the study of the field propagation in the whole sequence, some approximations were made. First, let us suppose that the optical paths in the two interferometer arms are perfectly balanced, so that the condition of constructively interference always occurs. Secondly, let us suppose the SOA saturated gain to be equal for each amplifier, composing the sequence. This situation is equivalent to say that the power incident on the Nth amplifier is identical to the power incident on the $(N-1)th$ amplifier. The consequence is a well defined relation for the reflectivities of the beam splitters composing the sequence. The lower inset in figure 3.3b indicates the field propagating in the gain arm of the ISA sequence. E_1 is the field at the input of the chain, the index i indicates the optical field at the amplifier entrance, o the amplified output field, while the index m refers to the beam portion traveling toward the upper arm.
The first beam splitter is the one fixing the amount of power entering in the SOAs. Then, since we assume equal input power to all the amplifier,

$$P^i_{gN} = P^i_{g1} = |E^i_{g1}|^2 = |t^{rbs}_0 E_1|^2 \tag{3.10}$$

where the constructive interference condition allows us to neglect the phase factor

associated with the field propagation.
The field at the input of the Nth amplifier, E^i_{gN}, is related to the output field of the $(N-1)th$ amplifier, $E^o_{g(N-1)}$ by

$$E^i_{gN} = t^{rbs}_N E^o_{g(N-1)} = t^{rbs}_N \sqrt{G}\, E^i_{g(N-1)} \tag{3.11}$$

It is easy to show that, the condition $E^i_{gN} = E^i_{g(N-1)}$ translates into the following relation

$$t^{bs}_k = \frac{1}{\sqrt{G}} \tag{3.12}$$

where $n = 1, 2, .., N-1$, with N being the number of amplifiers composing the ISA sequence. At the end of the chain, $t^{bs}_N = 0$ so the whole amplified power can be combined with the field traveling in the upper arm.
Finally, the last assumption implies, similarly to the case of the single amplifier, that E_{lN} is equal to zero, at the beam combiners. From the relations outlined in the previous section, we know that $E_{c1} = h^{n=1}_{11} E_1$, where $h^{n=N}_{jj}$ labels the elements of the matrix which describes the $N-th$ stage. The fields at the successive combining stage, indicated in the upper inset of fig. 3.3b, obeys the following equations

$$\begin{aligned} E_{c2} &= t^c_2 E_{c1} + i r^c_2 E^m_{g2} \\ E_{l2} &= i r^c_2 E_{c1} + t^c_2 E^m_{g2} \end{aligned} \tag{3.13}$$

where $E^m_{g2} = i\, r^{bs}_2 E^o_{g2}$. The two fields can be easily related to the input field, by

$$\begin{aligned} E_{c2} &= \left[t^c_2 h^{n=1}_{11} - r^c_2\, r^{bs}_2 \sqrt{G} t^{bs}_0 \right] E_1 = h^{n=2}_{11} E_1 \\ E_{l2} &= \left[i r^c_2 h^{n=11}_{11} + i t^c_2\, r^{bs}_2 \sqrt{G} t^{bs}_0 \right] E_1 = h^{n=2}_{21} E_1 \end{aligned} \tag{3.14}$$

The introduction of $h^{n=2}_{11}$ allows the generalization of the previous formulas for the $N-th$ stage of the sequence. In fact,

$$\begin{aligned} E_{cN} &= h^{n=N}_{11} E_1 \\ E_{lN} &= h^{n=N}_{21} E_1 \end{aligned} \tag{3.15}$$

where

$$\begin{aligned} h^{n=N}_{11} &= t^c_N h^{n=(N-1)}_{11} - r^c_N\, r^{bs}_N \sqrt{G} t^{bs}_0 \\ h^{n=N}_{21} &= i r^c_N h^{n=(N-1)}_{11} + i t^c_N\, r^{bs}_N \sqrt{G} t^{bs}_0 \end{aligned} \tag{3.16}$$

As for the single stage ISA, the no loss condition imposes a well defined relation for the beam combiner reflectivities, given by

$$\frac{t^c_N}{r^c_N} = -\frac{h^{n=N}_{11}}{r^{bs}_N \sqrt{G} t^{bs}_0} \tag{3.17}$$

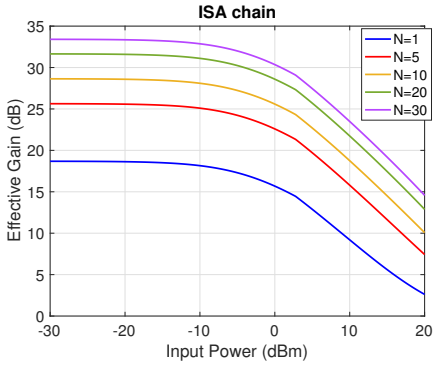

FIGURE 3.4: ISA sequence effective gain, as a function of the input power, when $R_0^{bs} = 0.9$, for different values of N.

where we remember $h_{11}^{n=1} = -\left[r_1^{bs}\ \sqrt{G}\ t_0^{bs}\ r_1^c + t_1^c\ r_0^{bs}\right]$.

Finally, we can define the sequence effective gain as the ratio between the power gained at the end of the chain and the input power,

$$G_{eff}^{seq} = \frac{P_c^N}{P_1} = |h_{11}^{n=N}|^2 \tag{3.18}$$

Analogously, the signal gain at the l port of every beam combiners in the sequence is equal to

$$L_{eff}^{seq} = \frac{P_l^N}{P_1} = |h_{21}^{n=N}|^2 \tag{3.19}$$

which in the ideal condition are null at every stage.
Figure 3.4 shows the effective gain as a function of the input power, for different number of SOAs composing the sequence, when the first BS reflectivity is equal to $R_0^{bs} = 0.9$. Both the small signal gain coefficient and the saturation output power increase with the increase of the number of elements of the sequence. A comparison with a linear sequence of SOAs, clarifies the advantages of the proposed solution. As reported, in fig. 3.5a and fig. 3.5b the small signal effective gain for a SOA sequence is higher that the one of the ISA sequence.
However, the plateaus reached in both the G_{eff}^0 and P_s^o curves, indicates that a further increase in the number of elements does not improve the performance of the cascade. Furthermore, the SOAs sequence have some advantages only for very low input power, meaning that, because of gain saturation, the maximum achievable output power is limited. On the contrary for the ISA sequence the high power operation is preferred. As reported in fig. 3.6 the maximum output power, extracted at the end of the sequence, linearly increases with the number of active media. The injection current is assumed to be equal to $500mA$ for all the SOAs. In chapter 2 we showed that this value of injection current corresponds to a small signal gain of $G_0 = 28.5dB$ and to a saturation power of $P_s = 18dBm$, when the input wavelength is equal to $\lambda = 1.55\mu m$.

The obtained results prove the potential of ISAs for power scaling applications.

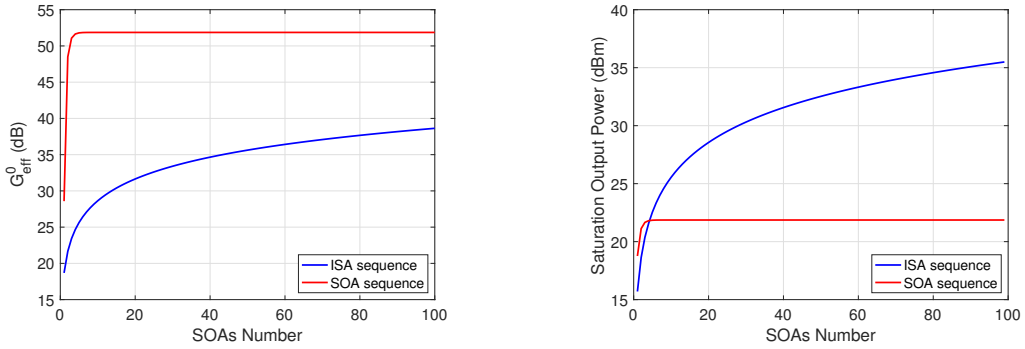

(A) (B)

FIGURE 3.5: (a): Small signal effective gain as a function of the number of elements composing the sequence. The blue curve refers to the ISA sequence when $R_0^{bs} = 0.9$, while the red one to the SOA sequence. (b):Saturation output power for the ISA sequence (blue curve), when $R_0^{bs} = 0.9$, and SOA sequence (red curve) with the increase of N.

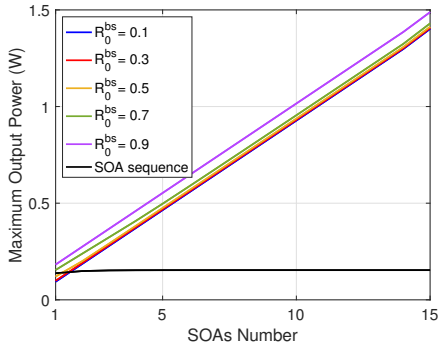

FIGURE 3.6: Maximum achievable power at the output of the sequence for both a SOA and ISA sequence, for different values of R_0^{bs} reflectivity.

3.3 Role of BS and BC reflectivities

To prove the effectiveness of the proposed architecture, additional considerations have been made. First, the reflectivity of the beam combiners and splitters need to assume well defined values to verify both the no loss condition at the beam combiners and the equal gain condition for each SOA. Figure 3.7a and fig. 3.7b shows the optimum R_n^{bs} and R_n^c values as a function of the input power, described respectively by eq. 3.12 and eq. 3.17. The simulation were performed assuming a total number of element, composing the chain equal to $N = 10$. The injection current is equal to $500mA$ for every SOA in the sequence. While R_i^{bs} are the same for each $n = 1,..N$ stage, the different curves in fig. 3.7b refer to the different $n-th$ stages. From the graphs it follows that to exploit the full potentiality of the device, optical components with power dependent reflectivity should be used. This is difficult to achieve. Moreover the signal power, that needs to be amplified is not known a priori. As an example of the working of the ISA sequence, we fixed the reflectivity of the various

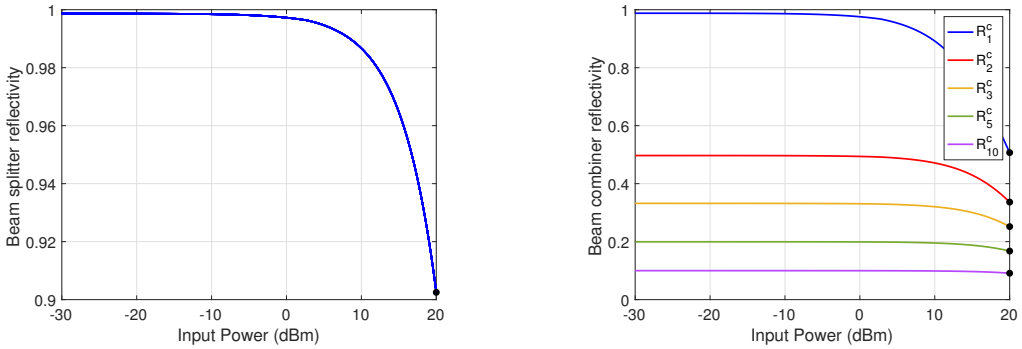

(A) (B)

FIGURE 3.7: (a): Beam splitter reflectivity as a function of the input power. The values are the same for each stage in the ISA sequence. (b): Beam combiner reflectivity as a function of the input power. The different curves refers to different stages in the ISA sequence.

components, at a certain value. Because we are interested in high power operation, we fixed both R_i^{bs} and R_i^c to the ideal value at the maximum value of the input power, the black dots in fig. 3.7a and fig. 3.7b.
This choice inevitably causes a decrease of the combining efficiency and an increase of the power at the l ports of the beam combiners at each sequence stages. In our design, these last represent losses. As a consequence, the behavior of the effective gain changes.Fig. 3.8a and fig. 3.8b shows how the non optimal choice of the reflectivities changes the behavior of the effective gain and increases the power losses at the combiner stages, especially for low input power. However, for high power operation, the gain resembles the ideal behavior and the losses reduce remarkably. This further confirms the capability of the device to scale up the amplified power of an input signal.

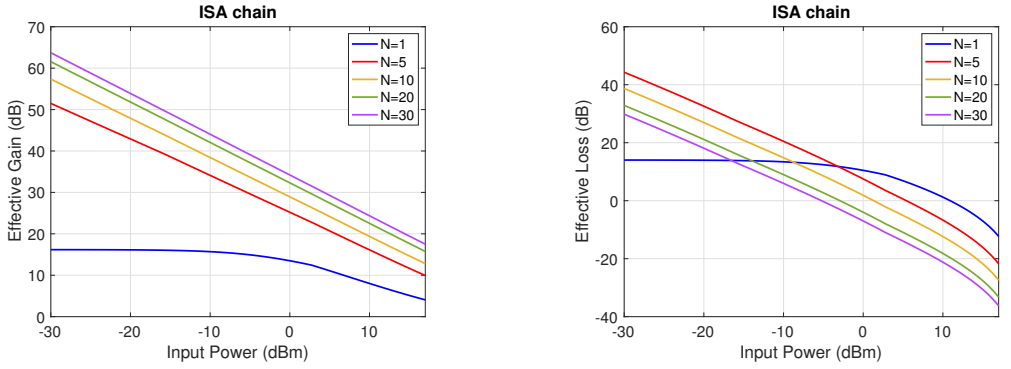

(A) (B)

FIGURE 3.8: (a): ISA sequence effective gain, when the beam splitters and combiners reflectivities move away from the ideal value. (b): ISA sequence gain evaluated at the l port of the last beam combiner, when the beam splitters and combiners reflectivity moves away from the ideal value. The different curves refer to a different of number of elements composing the sequence.

Another relevant test is to look for effects due to a distribution of reflectivity values.

For this reason, we introduced a normal distribution of errors in the reflectivity values in R_n^{bs} and R_n^c, at every stage in the ISA sequence.

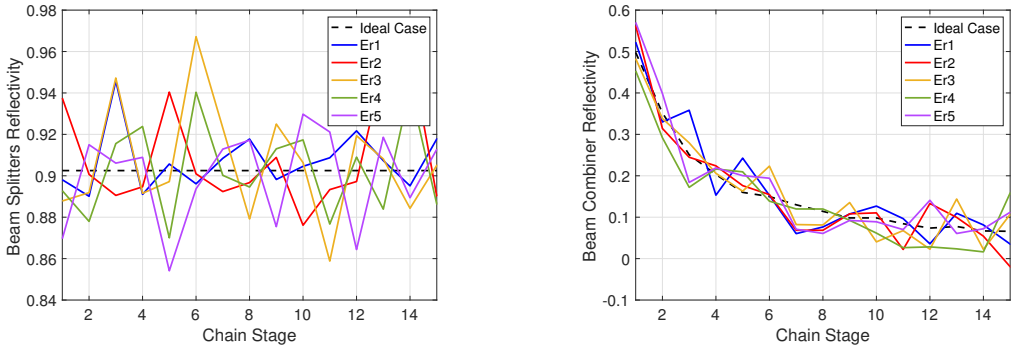

(A) (B)

FIGURE 3.9: (a):Beam splitters reflectivity as a function of the sequence stage. The dashed curve indicates the optimum values. (b): Beam combiners reflectivity as a function of the sequence stage. The dashed curve indicates the optimum values.

The simulation were performed by adding to the ideal values of R_n^{bs} and R_n^c, in the $n-th$ stage, a random scalar error drawn from the standard normal distribution, ranging from -0.1 to 0.1. The simulation were run several times. in order to analyze more than one error configuration. In each configuration the error introduced in both R_n^{bs} and R_n^c is different. The solid curves in fig. 3.9a and fig. 3.9b indicate the used values in both R_N^{bs} and R_N^c, while the dashed line shows the ideal values.
Figure 3.10 reports the output power does not depend significantly on the actual values of the reflectivities. This shows the robustness of the proposed idea.

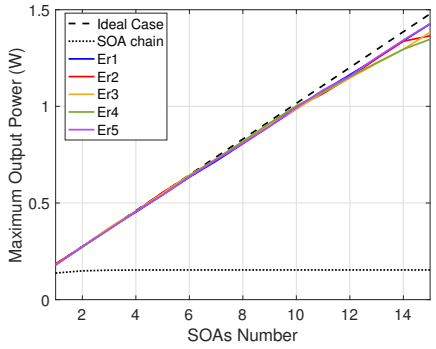

FIGURE 3.10: Maximum output power extracted from the whole sequence as a function of the SOA elements composing the sequence for various reflectivity distributions.

3.4 Effective gain and phase difference

Up to now, we have always suppose the amplifier to work under the ideal condition of constructive interference. This implies that the phase of the field propagating in

the gain arm is equal to the phase of the field propagating in the upper arm. Such a condition, if no other processes causing a phase change are present, translates into having the two optical paths equal one to each other. However, this condition is rarely met.
For simplicity, let us consider only the single stage ISA. Similar considerations hold for the multi-element sequence. Let us indicate with d_1 the length of the gain arm. During its propagation the beam travels through the active medium, imparting on it a phase shift equal to $, k\, n\, L_g$, where L_g is the length of the amplifier, while n its refractive index. If d_1 and d_2 indicate the two arm lengths, a null phase difference is reached when

$$\delta d = d_2 - d_1 = n\, L_g \tag{3.20}$$

which for our SOA is approximately equal to $\delta d \approx 0.48cm$.

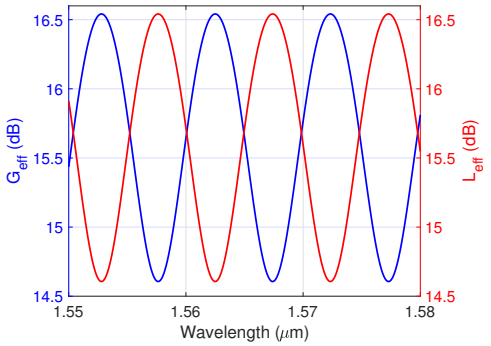

FIGURE 3.11: (a): Isa effective gain (the blue curve) and Gain at the l port of the beam combiner (red curve) as a function of the signal wavelength, for a fixed value of the input power, $P_{in} = 0.001mW$. Here we fixed $R_{bs} = 0.9$ and $R_c = 0.5$ and $\Delta d = 0.025cm$. Different values of δd influences the free spectral range of the interference fringes.

Managing such a path difference, could be far from trivial from an experimental point of view. First any environment fluctuations impact on δd. Then, the refractive index of semiconductor materials changes with both the temperature , the injection current and the input power. For this reason, without an active control feedback system and in a free space configuration, as in our case, the control of the phase difference turned out to be very difficult.
Therefore, it is useful to consider the impact of a phase difference in the model. This causes the presence of some losses at the beam combiner, and a decrease of the effective gain. Under this condition, the two ISA coefficients, in eq. 3.8 and in eq. 3.9, assume the following form

$$\begin{aligned} G_{eff} &= |e^{-i\,k\,\Delta d}\sqrt{G}\, t_{bs}\, r_c + t_c\, r_{bs}|^2 \\ L_{eff} &= |e^{-i\,k\,\Delta d}\sqrt{G}\, t_{bs}\, t_c - r_c\, r_{bs}|^2 \end{aligned} \tag{3.21}$$

where $e^{-i\,k\,\Delta d}$ indicates the additional phase caused by the different optical paths. Interference fringes appears as shown in fig. 3.11, where a $\delta d = 0.025cm$ was assumed. The simulation were performed assuming an ISA input power of $0.001mW$, at which the single stage ISA effective gain assumes its maximum value, as shown in

fig. 3.2b. The input signal wavelength is equal to $1.55\mu m$, while the injection current is assumed equal to $500mA$.
Key parameter in the understanding of the ISA performance is the visibility, V, defined as

$$V = \frac{I_{max} - I_{min}}{I_{max} + I_{min}} \tag{3.22}$$

where I_{max} and I_{min} indicates the maximum and minimum values, of either G_{eff} and L_{eff}. The visibility quantifies the interference contrast and assumes values between 0 and 1. The ISA should operates in the condition $V = 1$, for both the effective gain and the effective loss, which allows the possibility of having $P_l = 0$. For all other conditions some losses will be always present.
Moreover, the power dependence of the gain, valuated at both the beam combiner

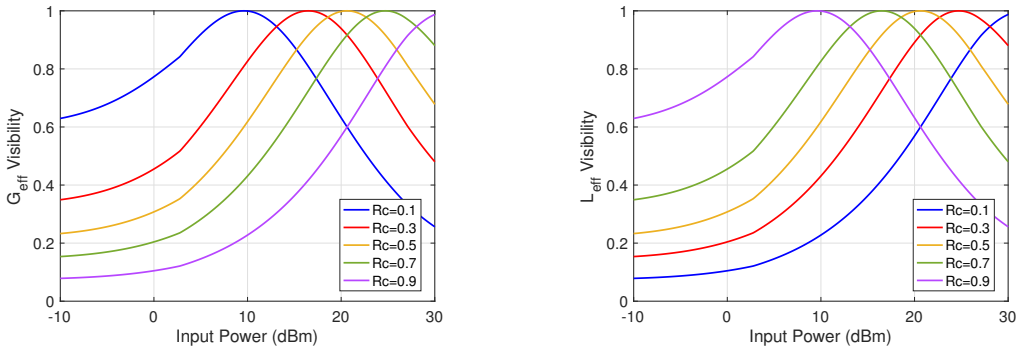

(A) (B)

FIGURE 3.12: (b): G_{eff}visibility as a function of the input power, for different value of the beam combiner reflectivity, when $R_{bs} = 0.9$. (c): L_{eff} as a function of the input power, for different value of the beam combiner reflectivities, when $R_{bs} = 0.9$.

ports, is reflected also in the visibility. From the graphs reported in figs. 3.12a and 3.12b it is evident that $V = 1$ is reached for specific values of the input power, depending on the reflectivity of the optical components in the ISA. It also appears that, for the single stage amplifier, only when $R_c = 0.5$ the visibility curves, for both G_{eff} and L_{eff}, follow the same trend with the input power. Finally, because of the wavelength dependence of the SOA gain coefficient (expressed by eq. 2.2 in Chapter 2) the visibility is expected to be affected also by the input signal wavelength.
These considerations lead to the conclusion that the ISA configuration must be carefully chosen. However, the advantages of the ISA and of the ISAs sequence, still remains also in non ideal conditions.

3.5 Experimental result

To prove the validity of the model a single stage ISA was setting and experimentally tested. Fig. 3.13 shows a photo of the realized device. A tunable laser source is

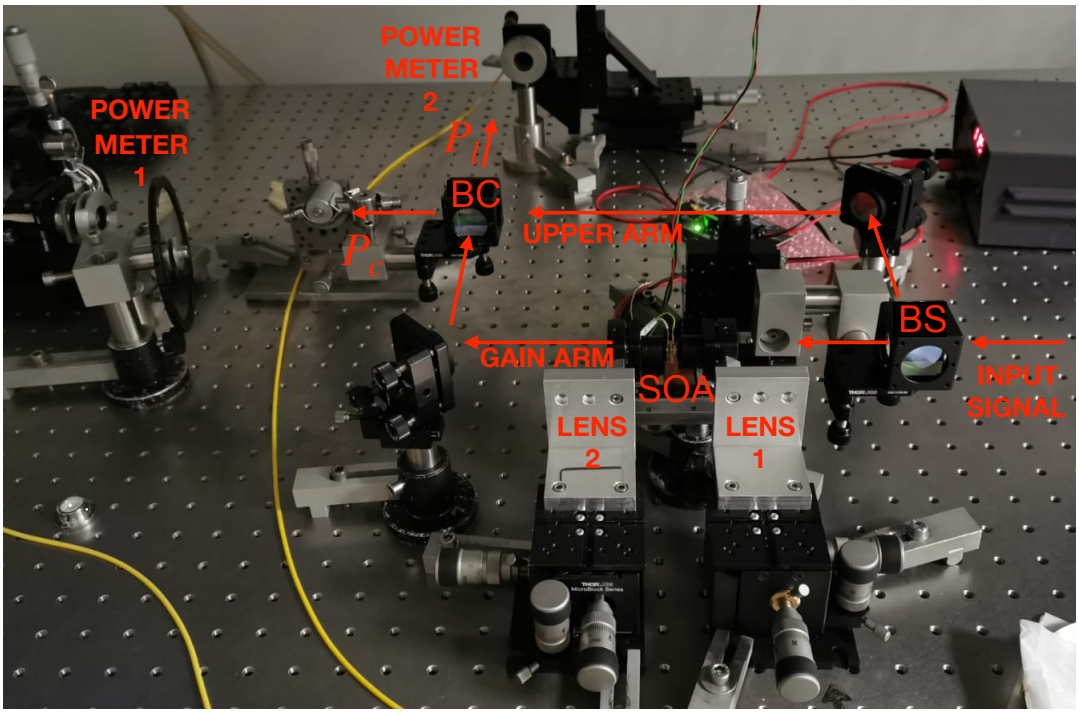

FIGURE 3.13: Photo of the tested ISA.

amplified by an Erbium Doped Fiber Amplifier (EDFA) and is sent on the first beam splitter. Here, 10% of the incoming radiation travels towards the amplifier, while the 90% travels unperturbed in the upper arm. The two fields are finally combined back together into a beam combiner. Two fiber-coupled power meters measure the radiation coming from the two exits of the beam combiner. The measures were taken by varying both the signal wavelength and the signal power. This last was done using a VOA. A polarization controller stage guarantees the appropriate beam polarization to achieve the maximum gain. Similar to the gain measurements, presented in Chapter 2, neutral density filters are place in front of the power meters. Figure 3.14 shows the collected output power as a function of the signal wavelength for two different ISA configurations. The upper panels show the experimental results obtained for a $70 \div 30$ beam combiner, while the lower panels refer to the $50 \div 50$ beam combiner. The left and right panels report the measurements for two input signals, $P_{in} = 17.2dBm$ and $Pin = -12.75dBm$. It is evident the power dependence of the visibility fringes, for both the two configurations. Furthermore, the results confirm the expected behavior of the two power visibilities for different values of the beam combiner reflectivity. In details, the combing (P_c) and loss (P_l) arm visibilities differ when $R_c = 0.7$, while equal to each other for $R_c = 0.5$. This equality remains also for different values of the input power. This result confirms the simulated predictions reported in fig. 3.12.
The ISA effective gain was measured for different value of the injection current, as reported in fig. 3.15a. To highlight the different saturation behavior of the ISA, with respect to the SOA, the same measurements were repeated by blocking the upper arm of the interferometer. Fig. 3.15b shows the obtained results.

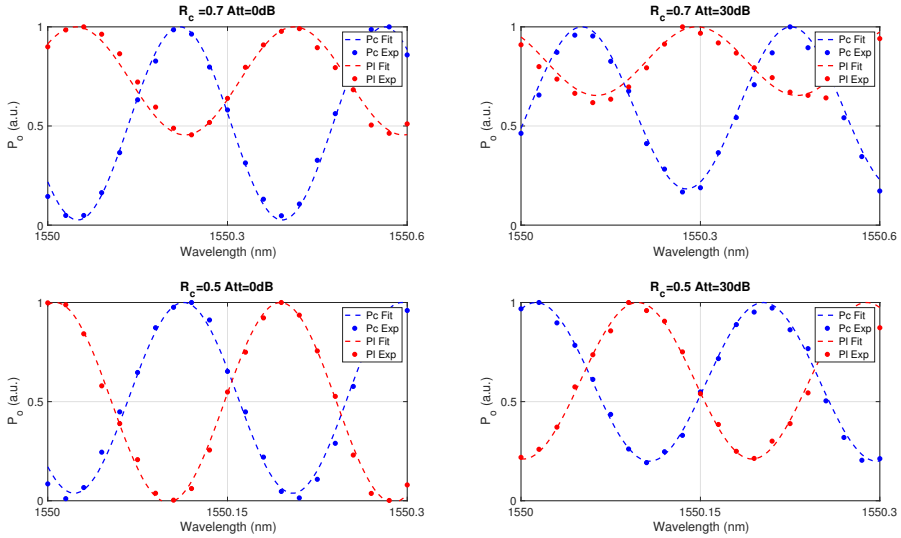

FIGURE 3.14: Normalized measured output power, at the two exits of the beam combiner, (P_c the blue curve and P_l the red curve). The upper panels for $R_c = 0.7$, while the lower panels for $R_c = 0.5$ configuration. The dots indicate the experimental points, while the dashed curves the fitted results. The measurements were taken at different values of the signal attenuation. The left panels refers to the condition of null attenuation, while the right power are the measurements obtained when an attenuation of $30dB$ is applied to the input signal.

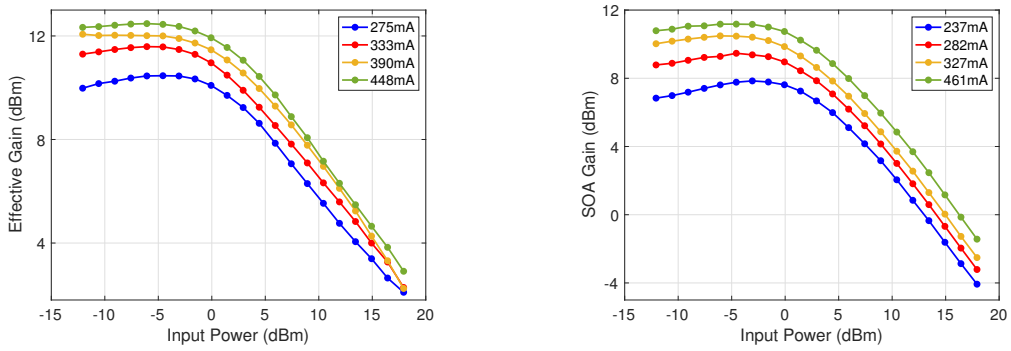

(A) (B)

FIGURE 3.15: (a): ISA maximum Effective gain as a function of the input power when $Rc = 0.5$ and $R_{bs} = 0.9$. The different curves refers to different values of the SOA injected current, at a wavelength corresponding to the maximum value of the output power, P_c (b): SOA gain as a function of the input power, measured at the exit of the beam combiner. The different curves refers to different values of the SOA injected current, at a wavelength corresponding to the maximum value of the output power, P_c.

A different behavior is clearly visible. The differences between the two curve, especially for values of input power closed to P_s, confirm the advantage of the ISA in the saturation regime.

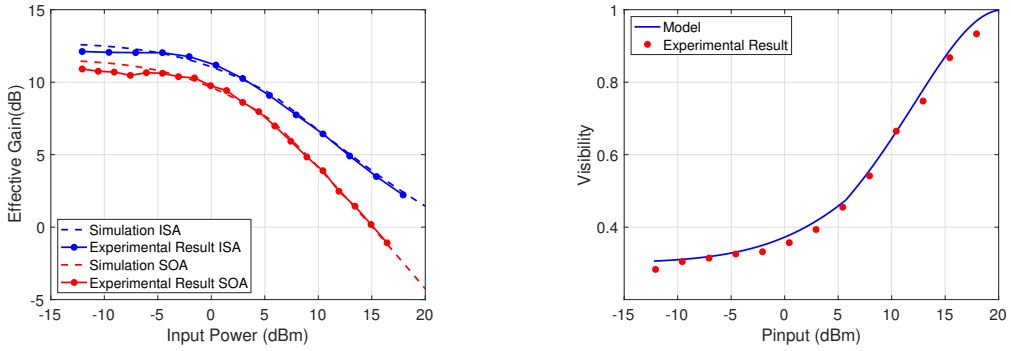

(A) (B)

FIGURE 3.16: (a): Comparison between the experimental results (dotted points) and the expected results (dashed lines) for both the ISA (blue curves) and SOA (red curves) gain when the injection current is equal to $400mA$. Here the SOA gain is measured by blocking the free arm of the interferometer. (b): Comparison between the obtained and the predicted combining arm visibility. The blue curve indicates the theoretical results, while the red points the experimental measurements, when the injection current is equal to $400mA$. The value of G_0 and P_s used in the simulation are those obtained experimentally.

Finally, the obtained experimental results were compared with the model predictions. To simulate the experimental conditions, we include in the model the measured losses at each optical components. The losses due to both the filter attenuation and the fiber coupling are equal to $\alpha_g = (-45.18 \pm 0.01)dB$ and $(\alpha_u = -45 - 54 \pm 0.01)dBm$ for the signal traveling respectively in the gain and in the upper arm of the interferometer. We measured a value of propagation losses equal to $\alpha_{pu} = (-1.03 \pm 0.01)dB$ when the signal travels in the upper arm of the interferometer, while we estimate $\alpha_{pg} = (-0.85 \pm 0.01)dB$ for the gain arm propagation losses.

Figure 3.16a and figure 3.16b shows the comparisons for both the maximum value of effective gain, the SOA gain and the visibility. Here, the SOA gain is measured by blocking the free arm of the interferometer and the values have to be corrected for the losses imparted by the use of the beam splitter and the beam combiner. Nevertheless, fig. 3.16a highlights the difference in the saturation behavior of the two amplifiers. The agreement between the experimental and expected results confirms the reliability of the elaborated model and the discussion we did in the previous section.

Based on the validation of the ISA model, we now turn to the design of a laser cavity which uses the ISA as gain stages.

To our knowledge, this the first demonstration of an unbalanced ISA, for power amplification. A similar concept was developed and proved in [92], and shown in fig. 3.17. The interferometric power amplifier consists of a MZ interferometer, with a SOA in each interferometer arms. Both the BS and BC are $3dB$ combiners. The authors reported the ISA gain saturation behavior which differs from the SOA saturation behavior, consistently with the results here presented. In [91], solutions to further increase the number of amplifier were proposed. Nevertheless, the use of SOAs in both of the two interferometer arms limits the scaling capability of the ISA sequence, because gain saturation occurs. Our design is expected to be superior,

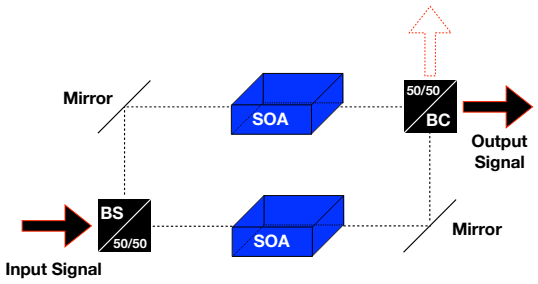

FIGURE 3.17: Interferometric Power Amplifier scheme proposed in [92].

when several SOAs compose the sequence. Indeed, because of the input power reduction, a higher number of SOAs can be used in the sequence, with respect to the design in fig. 3.17. This results in a higher amplified power at the end of the sequence.

Chapter 4

Laser Resonator

A laser device comprises an optical amplifier and optical resonator. While the first initiates and sustains the light emission, the optical resonator provides the feedback, to maintain the laser oscillation. This chapter deals with the fundamental properties of optical resonators and laser systems. The fundamental steps for a correct design of the laser resonator proposed are presented. Then the design we used in this thesis is presented. Finally, the experimental results of a semiconductor external cavity laser are shown. In this chapter a SOA s used as gain stage.

4.1 Passive optical resonator

An optical resonator consists of a collection of mirrors. Multiple reflections confine and store light in forms of standing waves, called the modes of the resonator. The field $E(x, y, 0)$, entering the resonator represents a cavity mode if, after a complete round trip, it reproduces itself. The self-consistency condition is expressed by the following equation

$$E(x, y, L) = \sigma \exp\left[-i\, k\, L\right] E(x, y, 0) \tag{4.1}$$

where L indicates the total cavity length, while σ is the mode eigenvalue.
According to the scalar diffraction theory (reported in Appendix B.), eq. 4.1 becomes [95]

$$E(x, y, L) = \sigma E(x, y, 0) = \int\int K(x, y, x', y')\; E(x', y', 0) dx'\, dy' \tag{4.2}$$

where the kernel function K accounts for the field propagation within the optical system. The eigensolutions of eq. 4.2, $E_{lm}(x, y, 0)$, describe the modal distribution of the field sustained in the optical cavity. Their complex eigenvalues, σ_{lm}, return both the round-trip diffraction losses and the mode resonance frequency.
A resonator is said to be stable when, after n multiple reflections, the optical ray remains confined into the cavity. For unstable resonators, the beam will diverge indefinitely away from the resonator axis. For every resonator a stability region can be identified. Indeed, a free space optical resonator can be identified by a matrix,

$$M = \begin{pmatrix} A & B \\ C & D \end{pmatrix} \tag{4.3}$$

describing the transformation of an arbitrary ray, when propagating into the cavity. The matrix element A, B,C and D depends on the geometry of the resonator. The relation between the kernel function K and the cavity matrix M is expressed by eq.

B.14 reported in Appendix B
The ray propagation after n reflections is described by the $n-th$ power of the matrix M. If M^n does not diverge by increasing n, the resonator is stable. From the Sylvester's theorem [96], M^n is given by the following formula

$$\begin{pmatrix} A & B \\ C & D \end{pmatrix}^n = \frac{1}{\sin\theta} \begin{pmatrix} A\sin n\theta - \sin(n-1)\theta & B\sin n\theta \\ C\sin n\theta & D\sin n\theta - \sin(n-1)\theta \end{pmatrix} \tag{4.4}$$

where $\cos\theta = \frac{A+D}{2}$.
The resonator is stable when θ is real. This condition implies that

$$\left|\frac{A+D}{2}\right| < 1 \tag{4.5}$$

At the boundary of the stability region, $|A+D| = \pm 2$, the resonator is said to be conditionally stable.
It can be shown that for stable resonators, with infinite apertures, the Hermite-Gaussian or Laguerre-Gaussian modes are the eigensolutions of the propagation equation 4.2, depending on the resonator symmetry [97]. Furthermore, since a Gaussian beam can be fully described by its complex q parameter while its propagation is described by the ABCD law[1] the self-consistency condition in eq. 4.1 transforms into the following second order equation

$$Cq^2 + (D-A)q + B = 0 \tag{4.6}$$

Depending on the mirrors arrangement and their curvature radius different types of resonator configurations can be distinguished. The configuration of interest, for the purpose of this thesis work, is depicted in fig. 4.1 and is referred to as a travelling-wave folded ring resonator.

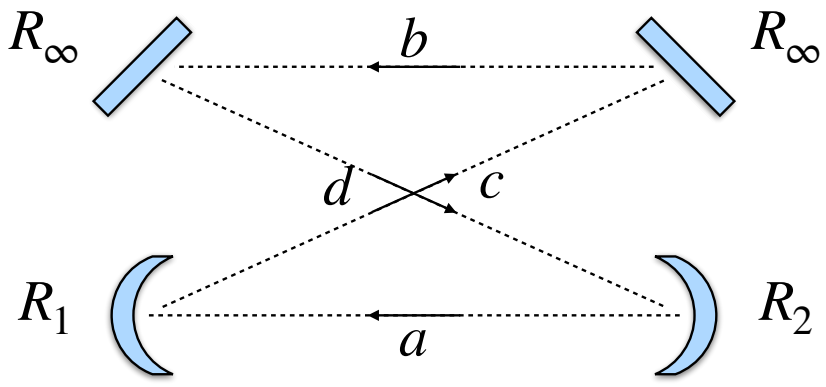

FIGURE 4.1: Sketch of a folded ring resonator, consisting of two plane mirrors and two spherical mirrors.

It consists of two plane mirrors and two spherical mirrors, whose radii are indicated with R_1 and R_2. When $R_1 = R_2 = R$, the resonator is symmetric. This resonator can be made unidirectional, which is a necessary condition in our design. The folded

[1] see Appendix C

geometry relaxes the geometrical constraints due to the length of the cavity and the incidence angle on the curvature mirrors.
Figure 4.2a shows an example of the stability diagram for such a resonator.

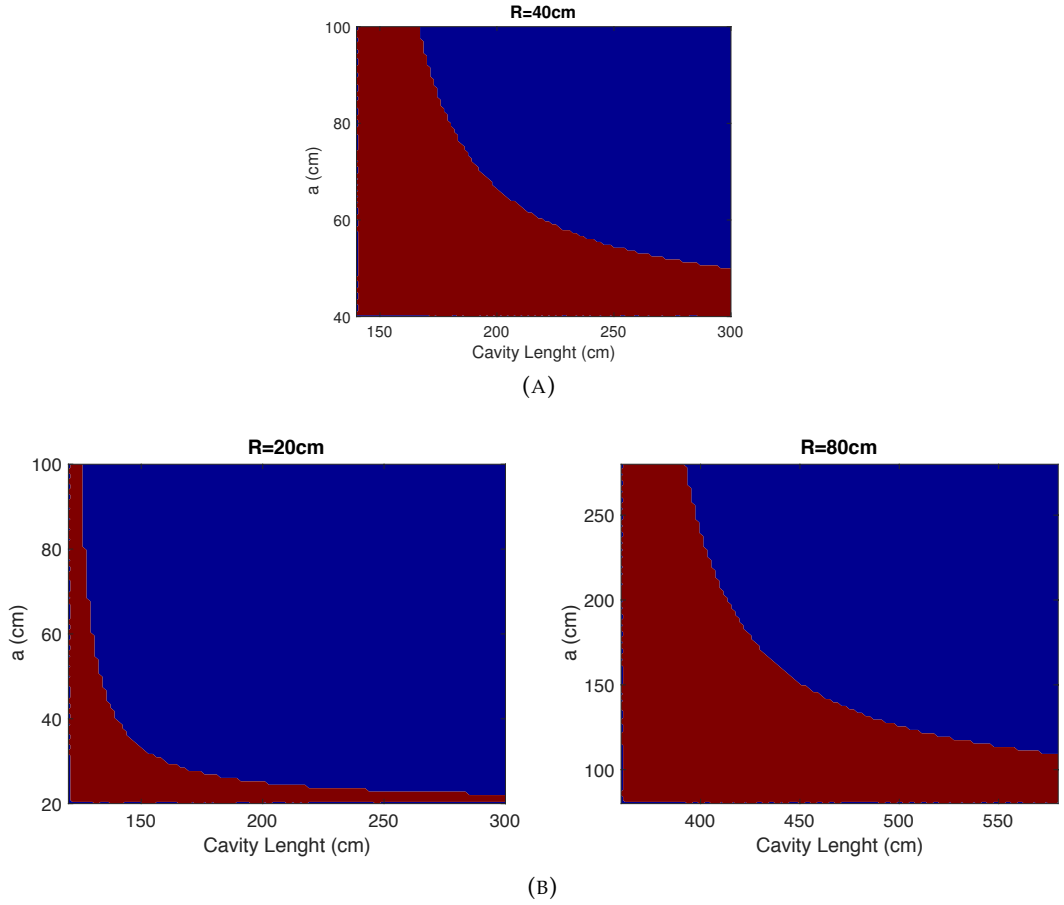

(A)

(B)

FIGURE 4.2: (a): Stability diagram for a symmetric folded ring resonator. The graph was obtained for a fixed value of the mirrors curvature radius, $R = 40cm$. The red regions are those for which the resonator is stable. (b): Stability diagram for two different values of curvature radius, $R = 20cm$ and $R = 80cm$.

The map was obtained by varying both the distance between the two spherical mirrors, a, and the total cavity length, $l = a + b + c + d$, for a fixed value of the mirrors curvature radius, $R = R_1 = R_2$. The red regions refer to all the configurations in which the resonator is stable. In fig. 4.2b, we can observe that a decrease in the mirror curvature radius causes a shrinkage of the stability region, while bigger radii extend the region also for longer cavity.
An example of the modes sustained by the cavity in one of these configuration is shown in fig. 4.3a, where $a = b = 50cm$ and $c = d = 55cm$
The eigenvalues associated with the resonator modes are given by the following amplitude factor [95]

$$\sigma_{lm} = \frac{1}{[A + B/q]^{1+l+m}} \tag{4.7}$$

where the indexes l and m represent the mode orders.

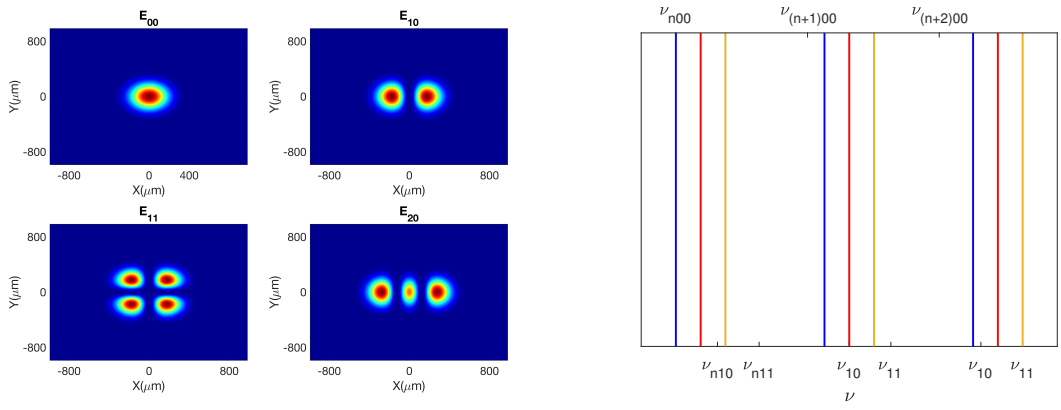

(A) (B)

FIGURE 4.3: (a): Modal distribution of the resonator in fig. 4.2a in one of the configuration in which is stable. (b): Mode spectrum of a folded ring resonator.

The total phase shift imparted on the resonator modes consists of two contributions. A first one is related to the field propagation within the optical cavity, while the second is associated with the phase of the complex eigenvalue. It can be easy demonstrated that, if $L = a + b + c + d$ is the total cavity length, each mode resonates at the following frequencies [95]

$$\nu_{nlm} = \frac{c}{L}\left[n + \frac{\Phi_{lm}}{2\pi}\right] \tag{4.8}$$

where the index n is the longitudinal mode order, while Φ_{lm} indicates the eigenvalue phase. Figure 4.3b shows the mode spectrum of one of the stable configuration of the folded ring resonator. The blue lines refers to the n index, while the red and the yellow lines respectively to the l and m indexes. Higher the frequency spacing between the different modes, lower is the competition among them. Mode competition can cause frequency instabilities and mode hopping.
The presence of any kind of limiting apertures in the resonator, introduces some diffraction losses. The squared module of the eigenvalues is related to the diffraction losses of each mode, after a complete cavity round trip. When no limiting apertures are present, the diffraction losses are all null, and an infinite number of modes coexist in the resonator. When an aperture is present, the modal structure can be significantly altered and, can only be found by the numerical solution of the integral equation 4.2. Among the possible numerical strategies we mentioned the Fox-Li iteration method [98] or the Prony method [99].

4.2 Mode excitation

When many modes coexist, the resonator output will be the result of the mode superposition. An ideal resonator should avoid the mode competition and oscillate in a single mode. The resonator modal oscillation, if no active media are placed within it, is started by an input laser beam, also called seed, inserted through the resonator output coupler (OC). The input signal can be expressed by a linear combination of

the resonator eigenmodes. To favor the excitation of a single mode, the input beam should be perfectly aligned to the resonator optical axis and should match as well as possible the resonator mode to be excited [100].
The power overlap integral [101] quantifies the amount of signal input power, whose field is $E_{in}(x,y)$, coupled to the lm resonator mode. It is defined as

$$\Gamma_{lm} = \frac{|\int\int E^*_{lm} E_{in} dxdy|^2}{\int\int |E_{lm}|^2 dxdy \quad \int\int |E_{in}|^2 dxdy} \tag{4.9}$$

and ranges between 0 and 1. $\Gamma_{lm} = 1$ means that all the input power is coupled to the lm mode, which will be the only one resonating into the cavity.
The easiest way to match the input signal to one of the resonator modes is with one or more lenses.
The passive folded ring resonator, depicted in fig. 4.2a was experimentally tested in one of its stable configuration. The curvature radius of the used spherical mirrors is equal to $R_1 = R_2 = R = 40cm$. The output coupler (OC), from which the field can exit the resonator, consists of a variable polarized beam splitter, placed between the two curved mirrors. For angles of incidence higher than 15°, the spherical mirrors introduces some astigmatism. A beam is said to be astigmatic when the focusing position is different for the x and y directions. This angle condition imposes some geometrical constraints on the cavity geometry, in particular on both c and d. For the realized resonator $a = b = 50\,cm$ and $c = d = 55\,cm$. To measure the exact profile of the excited resonator mode a $4f$ imaging system was used between the OC and the beam profiler, with $f = 7.5cm$. The modal matching between the input signal beam and the resonator modes was obtained by using a couple of lenses, with focal lengths $f_1 = 20cm$ and $f_2 = 10cm$, as shown in fig. 4.4.

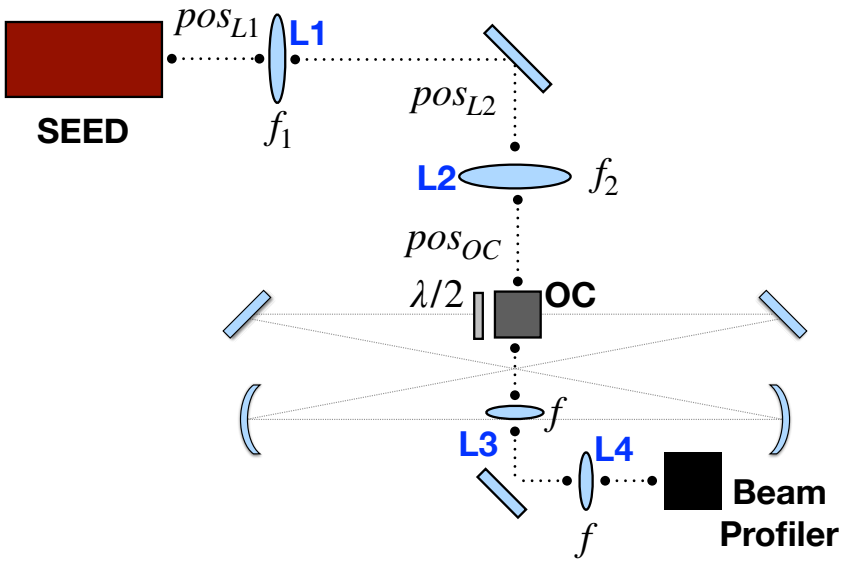

FIGURE 4.4: Sketch of the set-up for mode matching.

When the input Gaussian beam propagates through such a optical system its q-parameter is modified according to the ACBD law[2] with A, B, C and D, being the elements of the following matrix

[2] $q_1 = \frac{Aq_0 + B}{Cq_0 + D}$

$$M = \begin{bmatrix} 1 & pos_{OC} \\ 0 & 1 \end{bmatrix} \begin{bmatrix} 1 & 0 \\ -1/f2 & 1 \end{bmatrix} \begin{bmatrix} 1 & pos_{L2} \\ 0 & 1 \end{bmatrix} \begin{bmatrix} 1 & 0 \\ -1/f1 & 1 \end{bmatrix} \begin{bmatrix} 1 & pos_{L1} \\ 0 & 1 \end{bmatrix} \tag{4.10}$$

where pos_{L1} indicates the first lens distance from the input beam, pos_{L2} the distance between the two lenses, while pos_{OC} the OC position with respect to the second lens. The variation of these parameters allow the transformation of the input laser beam into the desired one. Figure 4.5a shows the variation of the beam width, along the optical system for a given distance. The comparison between the simulated behavior and the experimental data proves the robustness of the model. Figure 4.5b shows the variation of the input beam width as a function of the distance between the two lenses. The dashed line indicates the target profile to efficiently excite the 00 mode of the resonator at the OC position.

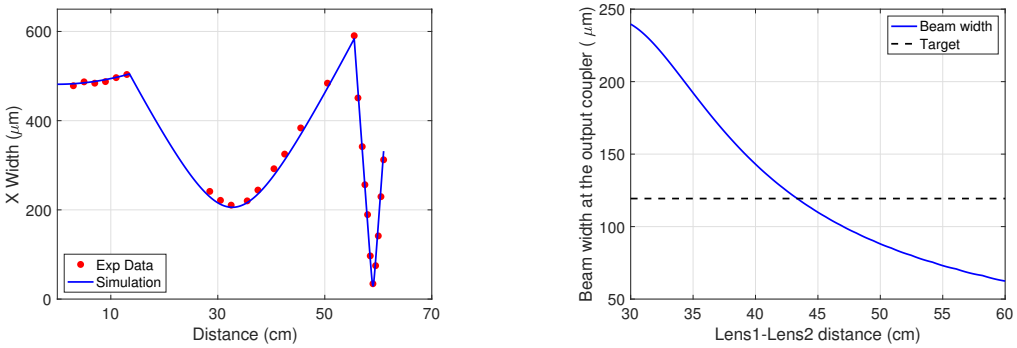

(A) (B)

FIGURE 4.5: (a): Beam width when the input signal propagates through the 2 lens system. The solid blue curve indicates the simulation results, while the red points reports the measured values. (b): Simulated variation of the beam width as a function of the distance between the two lenses. The dashed black curve indicates the target beam profile.

For this particular configuration, the fundamental mode of the resonator is excited when the first lens is placed at $10cm$ from the input of the signal beam, the second lens is $43cm$ far from the first lens and OC is $15cm$ distant from the second lens. Table 4.1 summaries the used lenses, including their focal length, their diameter and the position with respect to the previous lens.

Lens	Focal Length (cm)	Diameter (cm)	Position (from the previous lens)
L_1	20	5	10[3]
L_2	10	5	43
L_3	7.5	2.5	pos_{OC} + 7.5
L_4	7.5	2.5	15

TABLE 4.1: Summary of the lenses used in the experimental set-up.

The profile at the end of the $4f$ imaging system was measured using a scan-slits

[3]Here the position is referred with respect to the seed laser source.

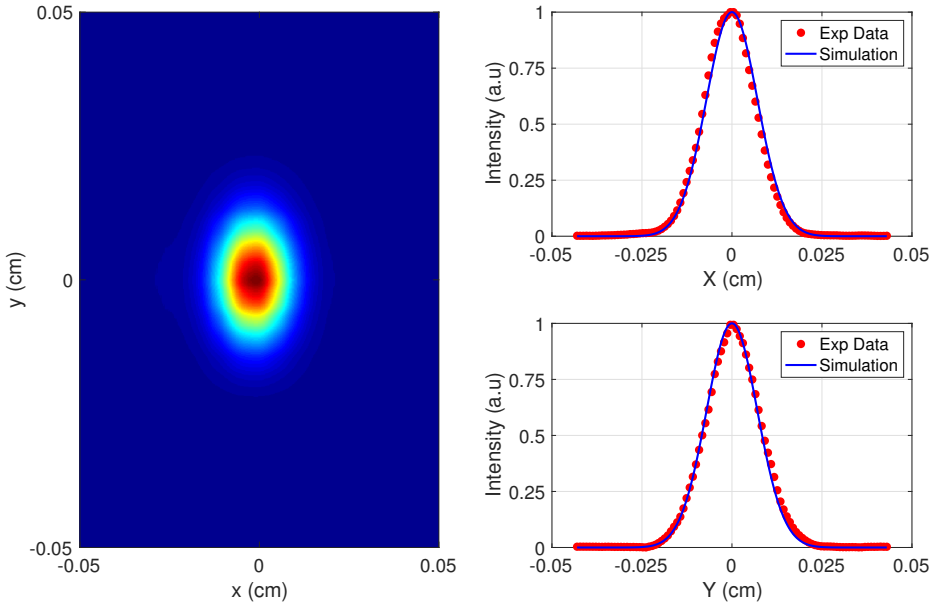

FIGURE 4.6: Beam Profile at the resonator output, when the input beam is mode matched to the fundamental mode of the resonator. The right insets shows a good agreement between the experimental data and the simulation prediction, when $\lambda = 1.55\,\mu m$.

beam profiler. Because the OC is a polarizing beam splitter, it was possible to eliminate the seed contribution in the measurement. Indeed, the beam splitter transmit the TE polarization, while reflects a TM polarized beam. The input beam polarization was varied such that it is almost completely sent into the cavity. After a cavity round trip, before hitting the OC, the beam encounters a half wave plate, whose rotation sets the portion of the beam that will remain into the cavity. Therefore, in the stationary condition, the beam circulating within the cavity will be TE polarized, while the one exiting from the cavity will be vertically polarized. As a consequence the beam profiler measures two contributions. The first one, horizontally polarized, comes directly from the input beam, after the first transmission from OC. The second contribution comes from the resonator modes. A polarizer filter, in front of the beam profiler, cut the contribution of the input beam, allowing the measurements of only the resonator modes.
Figure 4.6 shows the measured profile of the fundamental mode at the output of the cavity. The panels compare the beam profile in the two directions with the simulated prediction.
If the frequency mode spacing is sufficiently large the excitation of higher order modes could be reached simply by tuning the input laser frequency. However, for the implemented resonator the total cavity length is quite long. This causes the higher order modes frequency spacing to be lower than the minimum frequency tuning of the input laser source. Nevertheless, it can be shown [102] that a transverse displacement of the input beam with respect to the resonator optical axis can cause the excitation of several eigenmodes.

Figure 4.7 shows the measured beam profile at the resonator output for different input beam displacements imparted in one or both the two directions, while fig. 4.8 represents the comparison between the model and the measurements. Also for higher order modes, the model is able to reproduce the experiment, where also the

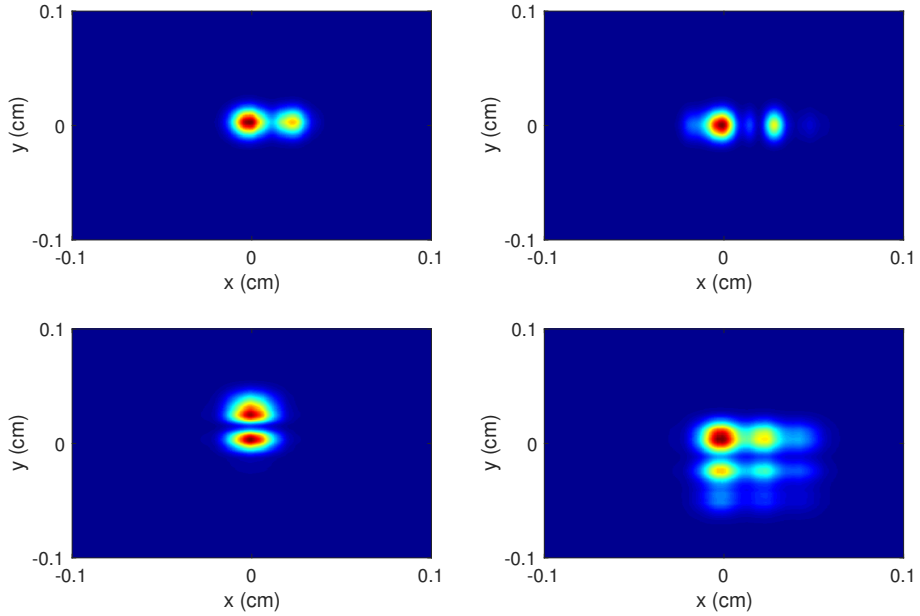

FIGURE 4.7: Measured beam profile at the cavity OC, for different displacements of the input beam.

mode phases have been taken into account.

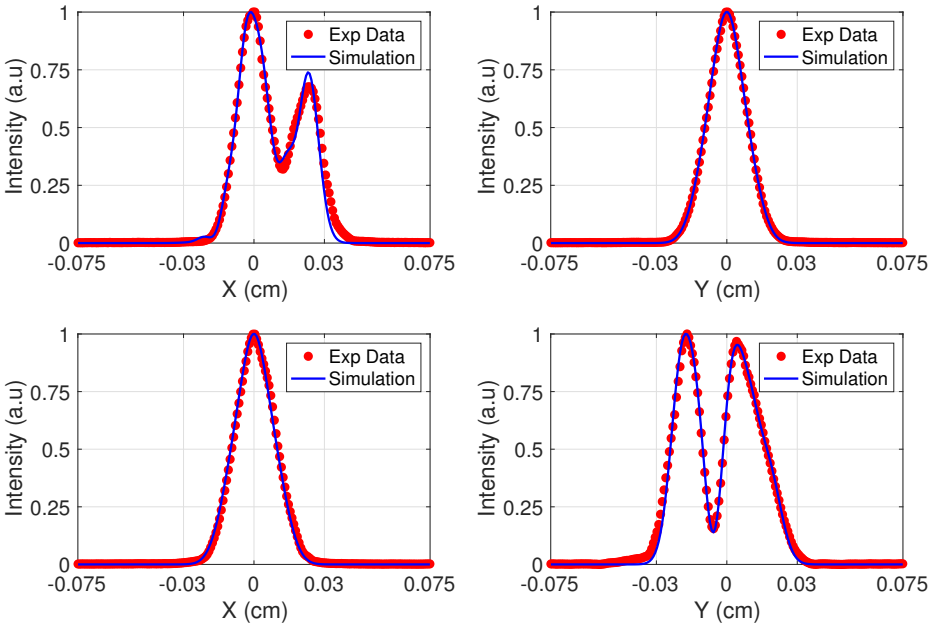

FIGURE 4.8: Profiles in the both x and y directions for two of the modes in fig. 4.7. The red points indicates the experimental values, while the solid blue curves refer to the simulation model.

4.3 External cavity semiconductor laser

Typically in semiconductor lasers, the optical cavity providing the feedback loop to sustain the laser oscillation, is implemented by cleaving the facets of the semiconductor crystal. As a consequence, the semiconductor material acts simultaneously as the active medium and the resonator. This solution results in very compact and easy to use device. However, it makes impossible to overcome some limitations of laser diodes and to improve their performance.
A solution comes from the external cavity laser (ECL). An ECL refers to any configuration in which the resonator structure is longer than the semiconductor itself. Several types of ECLs can be realized and can be organized in three different classes [103], reported in fig. 4.9. The most common and easiest to align is the extended-

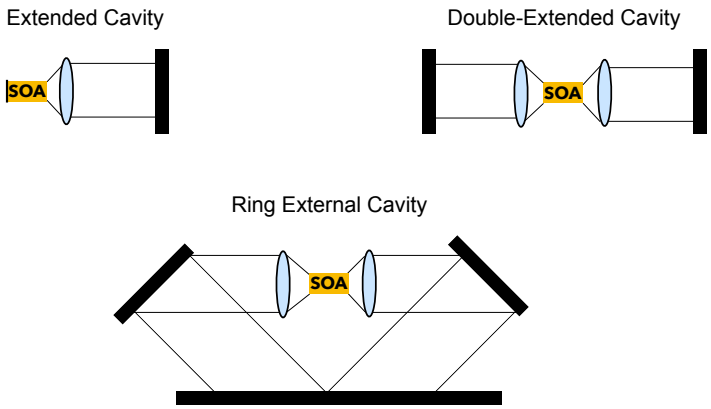

FIGURE 4.9: Different ECLs geometries

cavity configuration. It comprises a semiconductor amplifier where only one of the two facets is either uncoated or has a highly reflecting coating. This last acts as the second mirror of a Fabry-Perot cavity. In the double-ended external cavity, antireflection coatings are present on both the amplifier facets. The emission exiting from the amplifier is retroreflected into the respective emission facet. The most complicated ECL design is the ring external cavity laser. The SOA is placed within a ring resonator and the light emission from one facet is coupled, after a round trip, to the opposite facet. Differently from the other design this configuration can be made unidirectional by inserting an optical isolator into the cavity. In this thesis work, the SOA is placed into the folded ring resonator, described in the previous sections.
As previously mentioned, to reduce the competition between higher order transversal modes, the frequency spacing between them should be as large as possible. For an ECL, the presence of the SOA guiding structure acts as a spatial filter. Depending on the dimension of the optical waveguide, the oscillation of higher order transversal modes can be avoided and the laser device can guarantee single mode operation. These considerations cannot be made for the longitudinal modes, since they depend on the total cavity length.
Therefore, for an ECL, because of the active waveguide, the field is forced to resonate in a well definite mode. For this reason, the stability region for such a resonator is identified as all the possible configurations, in which the coupling losses between the waveguide field and the cavity field are small. By cavity field we mean the SOA emitted field, after a cavity round trip. The coupling losses are evaluated from the power overlap integral, defined in eq. 4.9. For an ECL, the stability depends not only

on the geometrical properties of the cavity, but also on the focusing and collimating lens positions, which are used to couple the cavity field to the gain stage.

4.3.1 ECL modeling: Nonparaxial beam propagation

To design the resonator geometry, we need to identify the stability region. It is then necessary the study of the field propagation within the resonator. Therefore, the exact determination of the beam profile of the field when propagates in the SOA is needed.
As already said, the resulting mode is strongly affected by the waveguide structure and, for commercial SOAs, this is often a proprietary technology. Nevertheless, at a first approximation, the SOA waveguide mode can be thought as Gaussian mode, defined by the following expression,

$$E(x,y) = \frac{1}{\sqrt{q_x(z)}} \exp\left[-ik\frac{x^2}{2q_x(z)}\right] \frac{1}{\sqrt{q_y(z)}} \exp\left[-ik\frac{y^2}{2q_y(z)}\right] \tag{4.11}$$

where q_x and q_y are the complex q-parametersr[4] in the two directions, x and y.
To account for the non ideal behavior the complex q-parameter, of a beam with waist w_0 and divergence angle θ_0 at wavelength λ, the following expression is used [104]

$$\frac{1}{q_{x,y}} = \frac{1}{R} - \frac{i\lambda M^2}{\pi w_{x,y}^2} \tag{4.12}$$

where $M^2 = \theta_{0x,y} w_{0x,y}/(\lambda/\pi)$ quantified the beam quality, while R and w refer respectively to the beam radius and beam width in a given position along the propagation direction. For a perfect Gaussian beam $M^2 = 1$. To fully determine the SOA field, the knowledge of $w_{0x,y}$ is needed.
The high value of the divergence angle, θ_0, typical for this amplifier, makes the paraxial approximation no more valid for describing the field propagation. The correct description of the field propagation within a certain optical system, for a generic field, can be directly derived from the solution of the Helmholtz equation.
According to the Rayleigh-Sommerfeld diffraction theory[5], the propagation of a field from the point $P_0 = (x_0, y_0)$ in the z_0 plane, to the point $P_1 = (x_1, y_1)$ in the z_1 plane, is given by the following equation [105]

$$E_1(x_1, y_1, z_1) = \frac{i}{\lambda} \int\int_A E_0(x_0, y_0, z_0) \frac{e^{-ikr_{01}}}{r_{01}} \cos(\theta)\, dx_0\, dy_0 \tag{4.13}$$

where the integral is evaluated over the aperture surface A in fig. 4.10. The index 0 indicates the input plane, while the index 1 refers to the observation plane. $r_{01} = \sqrt{(x_1 - x_0)^2 + (y_1 - y_0^2) + (z_1 - z_0)^2}$ is the spatial distance between the two points, while θ is the angle between the vector $\vec{r_{01}}$ and the versor normal to the input plane, $\hat{n}$.
The integral equation in eq. 4.13 needs to be numerically solved. Besides the direct integration methods, Fast Fourier Transform (FFT) algorithms, which are commonly implemented in the evaluation of Fresnel Integral, can offer a valid alternative for an efficient and rapid solution.

[4] See Appendix C
[5] See Appendix B for more details

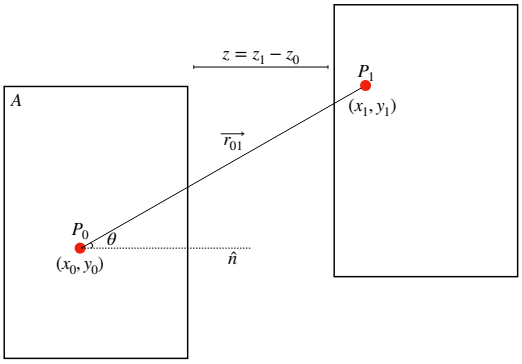

FIGURE 4.10: Illustration of the system of the Rayleigh-Sommerfeld theory

Indeed, the integral in eq. 4.13 can also be expressed in the following form

$$E_1(x_1, y_1, z_1) = \frac{iz}{\lambda} \int\int_A \frac{\exp(-ik\sqrt{(x_1 - x_0)^2 + (y_1 - y_0)^2 + z^2})}{(x_1 - x_0)^2 + (y_1 - y_0)^2 + z^2} E_0(x_0, y_0, z_0)\, dx_0\, dy_0 \tag{4.14}$$

where $\cos\theta = z/r_{01}$ and $z = z_1 - z_0$ is the distance between the two planes.
From eq. 4.14 it is evident that the Rayleigh-Sommerfeld diffraction integral can be viewed as a linear convolution between the field $E_0(x_0, y_0, z_0)$ and the kernel function $g(x_1 - x_0, y_1 - y_0, z)$, defined by

$$g(x, y, z) = \frac{iz}{\lambda} \frac{\exp(-ik\sqrt{x^2 + y^2 + z^2})}{x^2 + y^2 + z^2} \tag{4.15}$$

According to the convolution theorem[106], the Fourier Transform of the convolution of two functions is equal to the product of their individual Fourier Transforms, Therefore, eq. 4.14 transforms into

$$E_1 = \mathcal{F}^{-1}\left[\, \mathcal{F}\left[E_0\right]\, \mathcal{F}\left[g\right] \right] \tag{4.16}$$

From a computational point of view, we always deal with discrete series [107]. The discrete convolution assumes the following form

$$E_0 * g = \sum_{k=-N/2+1}^{N/2} E_0^k\, g^{j-k} \tag{4.17}$$

where $-N/2 \leq k \leq N/2 + 1$. In this case, the convolution theorem states that for a given periodic signal, completely determined by its N values, its convolution with a function of finite duration, N, is the product of the two Discrete Fourier Transforms and assumes the following form

$$DFT\left[E_0 * g\right] = DFT[E_0]\; DFT[g] \tag{4.18}$$

where DFT refers to the Discrete Fourier Transform of the data sequence. However, the discrete convolution theorem is based on the assumption that the signal is periodic. For this reason, the expression in eq. 4.18 is also called circular (or cyclic)

convolution. For aperiodic signals, the result obtained from eq. 4.18 may substantially differ from the correct one expressed by eq. 4.17, which is also referred to as linear convolution. Nevertheless, FFT algorithms can still be implemented with the use of the expedient of zero-padding [108]. The method here used, consists in the extension of the signal E_0 from N to $M = 2N$ elements by padding symmetrically the data series with $M/2$ null points at both the two ends. Then, the impulse response g is evaluated through its analytical expression, for all the M points. The final result is given by the Inverse FFT of the product of the FFTs of the two individual functions, E_0 and g. The observation field will be a numerical series of M points. However, the points of interest are only the N central values, those ranging from $-N/2$ to $N/2-1$. The procedure is also generally called linearization of the convolution.
Let us call L_0 the size of the initial plane and L_1 the size of the observation plane. If N is the total number of points, the sampling intervals will be $\delta_0 = L_0/N$ and $\delta_1 = L_1/N$, respectively for the initial and the observation planes. As clarified in Appendix D, FFT algorithms, already implemented in many commercial software, impose a well defined relation between the coordinate space variables and the spatial frequency variables. The implication is that the discrete form of eq. 4.16 can be solved only if $L_0 = L_1$ [109], and the coordinate axes are equally sampled. Of course, when the propagation distance increases or when the beam divergence is high, the consequence will be either an under-sampling of the input field or an excessive computational effort.
Nevertheless, the adoption of the Scaled Fourier Transform (SFT) [110, 111, 112] can still allow the use of FFTs, also when L_0 is different from L_1. First, we need to derive the discrete form of the diffraction integral.
The coordinate values of the input field x_0 belong to the interval $[-L_0/2, L_0/2]$, and the function E_0 is sampled in N points such that $x_0^{n_0} = n_0\,\delta_0$. Similar consideration can be made also for the observation coordinate space, whose values are given by $x_1^{n_1} = n_1\,\delta_1$. Analogously for the y-coordinate , $y_0^{m_0} = m_0\,\delta_0$ and $y_1^{m_1} = m_1\,\delta_1$. The indexes n_0, m_0 and n_1, m_1 go from $-N/2$ to $N/2-1$. The distance between the two points becomes

$$r_{n_0n_1,m_0m_1} = [(n_1\delta_1 - n_0\delta_0)^2 + (m_1\delta_1 - m_0\delta_0)^2 + z^2]^{1/2} \tag{4.19}$$

Eq. 4.14 transforms into

$$E_1(n_1,m_1) = \frac{i\,z}{\lambda} \sum_{n_0=-N/2}^{N/2-1} \sum_{m_0=-N/2}^{N/2-1} E_0(n_0,m_0)\,\frac{\exp(-i\,k\,r_{n_0n_1,m_0m_1})}{r^2_{n_0n_1,m_0m_1}}\delta_0^2 \tag{4.20}$$

The kernel function is further modified by introducing two scale factor α_0 and α_1. If $\delta = \max(\delta_0,\delta_1)$, then $\alpha_0 = \delta_0/\delta$ and $\alpha_1 = \delta_1/\delta$ [110]. It follows that the kernel function can be defined by the unique sampling parameter δ, according to

$$g(n_0n_1,m_0m_1) = \frac{i\,z}{\lambda}\,\frac{\exp(-i\,k\,\sqrt{(\alpha_1n_1-\alpha_0n_0)^2\,\delta^2 + (\alpha_1m_1-\alpha_0m_0)^2\,\delta^2 + z^2}}{(\alpha_1n_1-\alpha_0n_0)^2\delta^2 + (\alpha_1m_1-\alpha_0m_0)^2\delta^2 + z^2} \tag{4.21}$$

Finally the discrete form of the Rayleigh-Sommerfeld diffraction integral assumes the following form

$$E_1(n_1,m_1) = \sum_{n_0=-N/2}^{N/2-1} \sum_{m_0=-N/2}^{N/2-1} E_0(n_0,m_0)g(n_0n_1,m_0m_1)\delta_0^2 \tag{4.22}$$

which can still be expressed by a convolution, if the SFTs are used. To prove this statement, let us call F_0 the SFT[6] of E_0, while H refers to the DFT of the Kernel function. If eq. 4.22 is indeed a convolution, the observation field will be given by the Inverse SFT of the product between F_0 and H,

$$E_1(n_1, m_1) = \frac{1}{M} \sum_{p=-M/2}^{M/2-1} \sum_{q=-M/2}^{M/2-1} F_0^{\alpha_0}(p, q) H(p, q) \omega_M^{-\alpha_1 m_1 p} \omega_M^{-\alpha' n_1 q} \tag{4.23}$$

with M being the total number of points after the linearization, while $\omega_M = \exp(-i2\pi/M)$. By substituting the expression for F_0 and H, the following result is obtained

$$\begin{aligned} E_1(n_1, m_1) = \frac{1}{M^2} \sum_{p=-M/2}^{M/2-1} \sum_{n_0=-M/2}^{M/2-1} \sum_{m_0=-M/2}^{M/2-1} E(n_0, m_0) \omega_M^{\alpha_0 n_0 p} \omega_M^{\alpha_0 m_0 q} \\ \sum_{n=-N/2}^{N/2-1} \sum_{m=-N/2}^{N/2-1} g(n, m) \omega_M^{np} \omega_M^{mq} \omega_M^{-\alpha_1 n_1 p} \omega_M^{-\alpha_1 m_1 q} \end{aligned} \tag{4.24}$$

After some manipulation, it can be easily shown that the previous result is transformed into

$$E_1(n_1, m_1) = \sum_{n_0=-N/2}^{N/2-1} \sum_{m_0=-N/2}^{N/2-1} E_0(n_0, m_0) g(\alpha_1 n_1 - \alpha_0 n_0, \alpha_1 m_1 - \alpha_0 m_0) \tag{4.25}$$

which is indeed the convolution between E_0 and g.
At this point, some consideration has to be made. The first regards the computational windows of both the initial and observation planes. An improper sampling causes aliasing errors. A good strategy, at least in a first approximation, could be having a window whose extent is larger than at least four times the width of the beam that has to be evaluated. For a 2D elliptical beam profile, as in our case, the window size differs for both the X and Y directions. The beam width can be easily determined for the known initial field, but become a difficult task after the propagation through a certain optical system, especially when the beam is far from being a purely Gaussian beam. The strategy, here adopted, is to choose the observation plane according to the expected width of a Gaussian beam, having the same beam waist of the initial field, after the propagation through the same optical system, that can be easily determined. In this way, we can assure a proper sampling for both the initial and observation fields, keeping the same number of points, also for very long propagation distances.
Secondly, the total number of points needs to be chosen in order to guarantee the correct sampling of the kernel function. From the sampling theorem, we can state that a data series is properly sampled if the maximum frequency is less than half the sampling rate. The responsible of the oscillations in the kernel function is the exponential in eq. 4.21. After the linearization procedure, this can be written in the following form

$$\Phi(n, m) = k \left(n^2\delta^2 + m^2\delta^2 + z^2\right)^{1/2} \tag{4.26}$$

Then the frequency measured in cycle/pixel units is given by

[6] See Appendix D for the complete description

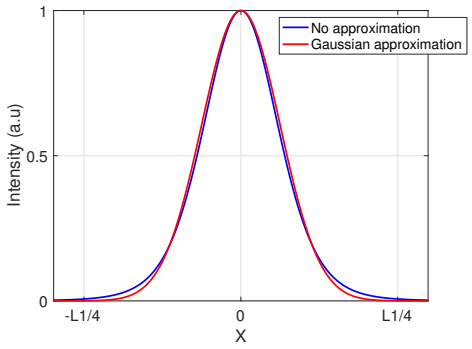

FIGURE 4.11: Beam Intensity profile of a gaussian beam with $1\mu m$ beam waist,$\lambda = 1.58\,\mu m$. The blue curve is obtained using the diffraction integral formula, while the red curve describes the Gaussian propagation law. The difference is an estimate of the error committed when using the paraxial approximation.

$$\nu(n) = \frac{1}{2\pi}\frac{d\Phi}{dn} \qquad \nu(m) = \frac{1}{2\pi}\frac{d\Phi}{dm} \tag{4.27}$$

The maximum frequency is achieved for $n, m = M/2$.

It follows that the minimum number of points is given by

$$N_{min} = \frac{2}{\lambda}\frac{\max(L_0, L_1)^2}{\left[\max(L_0, L_1)^2 + z^2\right]^{1/2}} \tag{4.28}$$

and depends on the size of the computational space grid and on the propagation distance z.

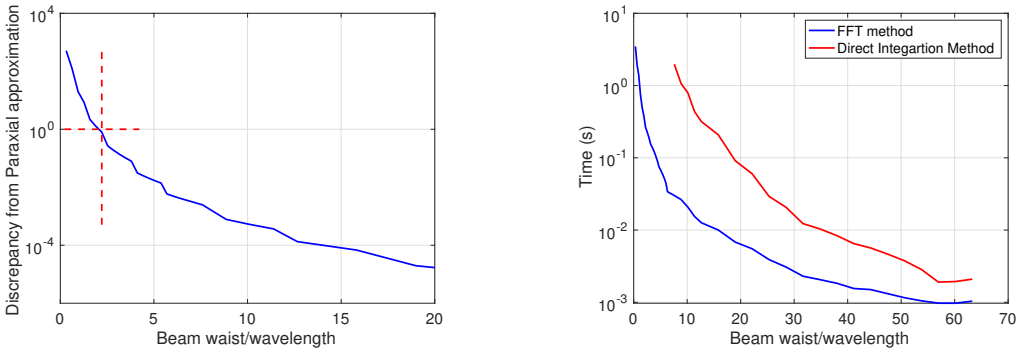

(A) (B)

FIGURE 4.12: (a): Discrepancy between the diffraction integral results and the paraxial approximation as a function of the beam waist. The red dashed curves indicates the point in which the error starts to become negligible. This occurs when $w_0 \approx 1.7\lambda$. (b): Computational time employed by the simulation for the resolution of the diffraction integral. The blue curve is obtained by the implementation of the FFT algorithm, while the red curve with the direct numerically integration of eq. 4.13.

Fig. 4.11 shows the difference between a nonparaxial beam, the blue curve in the image, described with the diffraction integral, and a paraxial beam, described by the Gaussian formula. Figure 4.12a clarifies that the paraxial approximation stops to be accurate when the initial beam waist is less than approximately 1.7 times the beam wavelength. This point is highlighted in the image by the red cross. Finally, fig. 4.12b reports the computational time employed by the FFT resolution model, and compares it with the time used by the direct integration resolution method, for the same number of points. A significant increase in the computational velocity is observed, when the FFT algorithms are used.

4.3.2 Aspheric lens description

The most important optical elements present in the cavity are lenses, and an appropriate description within the wave optics formalism is needed.
A lens is said to be thin if the coordinate points of a ray entering the lens are the same also for the lens exiting position. In a purely way-optics formalism, a thin lens simply imparts on the incident wave a phase delay proportional to the lens thickness. Therefore, all the lens properties can be fully described by the lens thickness function, $\Delta(x,y)$, which describes the variation of the lens geometry in space. If Δ_0 is the maximum thickness, the total phase delay suffered by the optical wave in passing through the lens is given by [105]

$$\Phi(x,y) = k\, n_l\, \Delta(x,y) + k[\Delta_0 - \Delta(x,y)] \tag{4.29}$$

where n_l is the refractive index of the lens material. The factor $k[\Delta_0 - \Delta(x,y)]$ accounts for the phase delay introduced by the remaining free space regions.
If the lens consists of tho spherical surfaces of curvature radius, R_1 and R_2, it can be easily shown that, within the paraxial approximation, the lens thickness function becomes

$$\Delta(x,y) = \Delta_0 - \frac{x^2+y^2}{2}\left(\frac{1}{R_1} - \frac{1}{R_2}\right) \tag{4.30}$$

where the sign of the radius of curvature is determined according to the convention, that a convex surface has a positive radius of curvature, while a concave surface has a negative radius of curvature. Defining the lens focal length as

$$f = (n-1)\left(\frac{1}{R_1} - \frac{1}{R_2}\right) \tag{4.31}$$

and substituting into eq. 4.29, the field at the output of the lens will be given by

$$E_l(x,y) = \exp\left[i\frac{k}{2f}(x^2+y^2)\right]\; E_0(x,y) \tag{4.32}$$

where $E_0(x,y)$ indicates the field at the input plane of the lens, while E_l the field at the output plane of the lens.
When the maximum thickness of the lens can be compared with the curvature radii of its surfaces, the lens is said to be thick. After the propagation through a thick lens, a wave exits at a different position with respect to the entrance point, and the

correct description cannot be reduced to a simple phase shift. However, most of the simplicity of the thin lens can be maintained by introducing the concepts of principal planes. Within the geometric optics formalism, after the ray tracing procedure, it can be easily shown that the effective focal length of the lens is given by the following expression

$$\frac{1}{f} = (n-1)\left[\frac{1}{R_1} - \frac{1}{R_2} + \frac{(n-1)\Delta_0}{nR_1R_2}\right] \tag{4.33}$$

which is also known as Lensmaker's equation. Because of this consideration, for spherical lenses within the paraxial approximation, the wave optics formalism could still be used if the expression obtained in eq. 4.33 is substituted in eq. 4.32.
Because of the very high divergence in the fast axis of the SOA emitted beam, spherical aberrations will typically occur when the beam encounters a lens. Spherical aberrations are a detrimental effect associated to the different behaviors of the rays when propagating through a lens, depending on the incidence position. The result is the presence of different focusing points, position dependent, which cause an overall degradation of the image produced by the lens.
A solution to correct for spherical aberrations is offered by aspheric lenses. An aspheric surface profile is often described by [113]

$$S(r) = \frac{r^2}{R\left(1+\sqrt{1-(1+\kappa)\frac{r^2}{R^2}}\right)} + a_4 r^4 + a_6 r^6 + ... \tag{4.34}$$

where $r = (x^2+y^2)^{1/2}$, R is the surface curvature radius while κ is the conic section. The coefficients α_i are called aspherical coefficients and describe the deviation of the surface from a perfect spherical one. The sketch in fig. 4.13 shows an example of an aspheric biconvex lens.

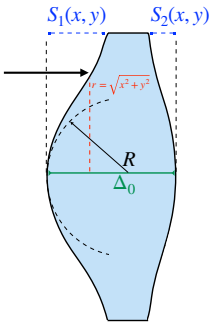

FIGURE 4.13: Sketch of an aspheric lens.

Typically, such complex surfaces are described and studied thanks to dedicated software, such as Zeemax [114, 115]. Here we propose a method, which can be implemented in the wave optics formalism presented before.
Similarly to the spherical case, the effect of a thin aspheric lens, can be imagined to be a simple phase delay, given by the following formula

$$\Phi(x,y) = \{n\left[\Delta_0 - S1(x,y) - S2(x,y)\right] + \left[S1(x,y) + S2(x,y)\right]\} \tag{4.35}$$

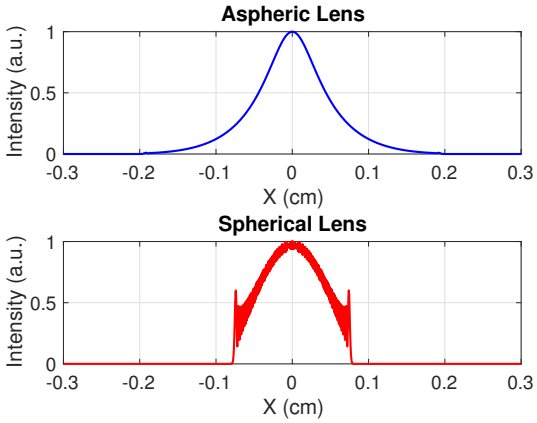

FIGURE 4.14: Comparison between the beam profile along the x direction for a beam waist of $w_0 = 1.5\mu m$, when $\lambda = 1.58\,\mu m$. The blue line refers to the simulated profile at the output of the aspheric lens, while the red curve to the simulated profile for the spherical lens. The superior performances of the first lens are clearly visible.

The lens output field become $E_l(x,y) = E_0(x,y)\exp(-i\,k\,\Phi(x,y))$.
For paraxial beam, the aspheric lens behaves identically with its spherical counterpart. The behavior changes as soon as the paraxial approximation fails. The curves in fig. 4.14 shows the difference in beam profile at the output of the lens, for an initial beam waist of $1.58\mu m$.
The advantages of the aspheric lens, described by the blue curve in the image, are clearly visible.

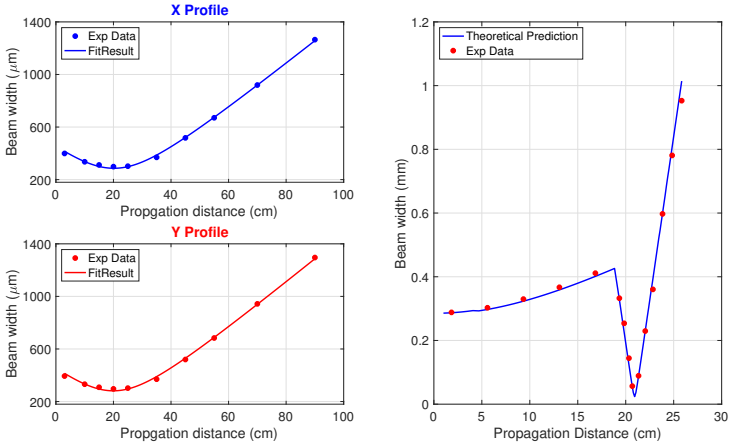

FIGURE 4.15: Experimental results (dots) and theoretical model (lines). The left panels show the fit, which allows estimating the beam waist. The right compares the experimental data (red points) with the simulated results, of the beam width measured at the output of the aspheric lens, as a function of the propagation distance. The lens is placed at a distance of 18.5 cm from the source waist position.

To validate these assumption,we experimentally tested the behavior of the *Thorlabs* AL2520 aspheric lens. The lens has an effective focal length of $f = 2.5cm$,a diameter

of $d = 2.5cm$, and a plane surface that allows the use of the thin lens approximation. A fiber coupled external source is sent to a fiber port. Through the measurement of the beam profile exiting from the fiber port, the laser beam waist was estimated. The left panels in fig. 4.15 show the result. Then, the beam profile at the output of the aspheric lens was measured. The red point is the right panel of fig. 4.15 indicates the measured beam width along the X direction. A similar behavior is found for the Y component. From the comparison with the simulated expected results, the blue curve in the graph, the used aspherical lens description is validated.
Both the high focal length and the small numerical aperture ($NA = 0.5$) of the tested lens, make the lens unusable for manipulating the high divergent SOA emitted beam. For this reason we mounted in our set-up a different aspheric lens, the C330TMD-C aspheric lens from *Thorlabs*. The curvature radii of the lens surfaces ($R1 = 2.97\,mm$ and $R2 = -2.72\,mm$) are very close to the lens thickness ($\Delta_0 = 3.2\,mm$). As a consequence, the thin lens approximation is no more valid. Unfortunately, we cannot reduce the effect caused by the lens thickness to a correction factor, as previously seen for the spherical case by eq. 4.33. To account for the lens thickness, we proposed an approach that links wave and ray optics.
The first step is the ray tracing evaluation of the path traveled by the optical beam when passing through the lens. The initial plane coincides with the lens position. According to the Snell refraction law, we can trace the beam position along the lens. As highlighted in fig. 4.16 the following relations hold

$$\begin{aligned} &\theta_{i1} = \theta_b + \theta_1 \\ &\sin(\theta_{i1}) = n_l \sin(\theta_{r1}) \\ &\alpha = \theta_1 - \theta_{r1} \\ &\theta_{i2} = \alpha + \theta_2 \\ &n_l \sin(\theta_{i2}) = \sin(\theta_{r2}) \\ &\beta = \theta_{r2} - \theta_2 \end{aligned} \tag{4.36}$$

where $\sin(\theta_1) = r_1/R_1$ and $\sin(\theta_2) = r_2/R_2$, where r_1 and r_2 describe the field position at the lens entrance and exit planes. The index i refers to the surface incidence angle, while r stands for the refraction.
Then, the thickness function, $\Delta(r)$ in eq. 4.29, is determined as the spatial distance

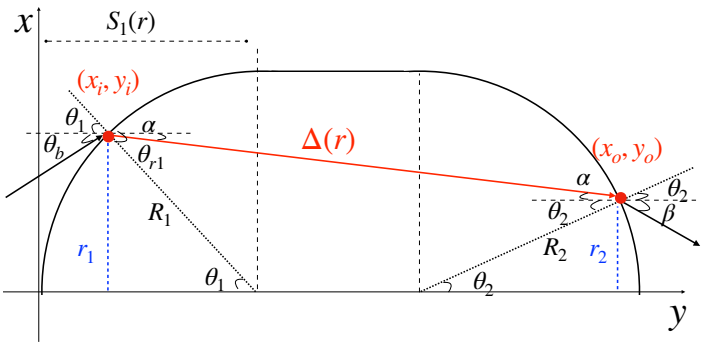

FIGURE 4.16: Relation between the angles defining the propagation of an optical ray into the lens.

between the beam coordinate points at the lens entrance, $(x_i = r_1, y_i)$ and the last beam position before it leaves the lens $(x_o = r_2, y_o)$. Both y_i and y_o are related to the field position, r_1 and r_2, through the lens surface profile function, $S(r)$ described by eq. 4.34.
It follows that, the lens thickness function is given by

$$\Delta(r) = \sqrt{(x_o - x_i)^2 + (y_o - y_i)^2} \tag{4.37}$$

The phase delay imparted by the lens on the propagating beam is found by substituting the result in eq. 4.37 into eq. 4.29. Besides the phase shift, the ray tracing procedure allows us to account for the different coordinate points at the output of the lens. The phase shift due to the propagation through the remaining free space region $\Delta^a(r) = \Delta^{a_1}(r) + \Delta^{a_2}(r)$ is evaluated in a similar way.

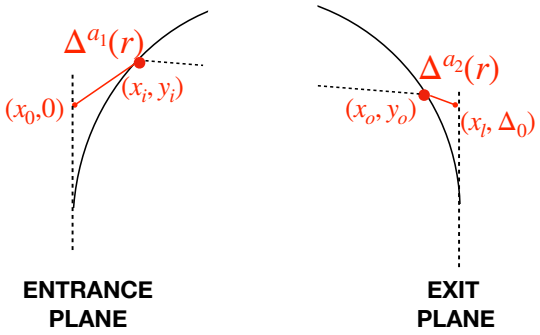

FIGURE 4.17: Diagram of the propagation through the free space regions

As reported in fig. 4.17, $\Delta^{a_1}(r)$ refers to the propagation from the lens entrance plane to the first lens surface, while $\Delta^{a_2}(r)$ to the propagation from the second lens surface to the exit plane. If $(x_0, 0)$ is the field point in the entrance plane,while (x_l, Δ_0) the field point in the exit plane $\Delta^{a_1}(r)$ and $\Delta^{a_2}(r)$ are given by

$$\begin{aligned} \Delta^{a_1}(r) &= \sqrt{(x_i - x_0)^2 + y_i^2} \\ \Delta^{a_2}(r) &= \sqrt{(x_o - x_l)^2 + (\Delta_0 - y_o^2)} \end{aligned} \tag{4.38}$$

where Δ_0 is the total lens thickness, while x_i is related to the beam divergence angle. Finally, the phase shift imparted by the lens on the propagating beam is given by

$$\Phi(r) = k\, n_l\, \Delta(r) + k\, \Delta^a(r) \tag{4.39}$$

with k wavevector and n_l lens refractive index.
Figures 4.18a, 4.18b shows some examples of ray tracing, for different values of the initial beam waist, at a given lens position. The red lines shows the lens behavior when the beam waist is equal to 300 μm, while the blue line trace the rays of a beam of waist equal to 5 μm. In fig. 4.18a, the incoming radiation is focused, independently of the lens position. We observed this behavior for values of beam waist higher than 50 μm. When the waist is further reduce, the lens collimates the rays, when placed at distance, approximately equal to the focal length, from the beam source, where the

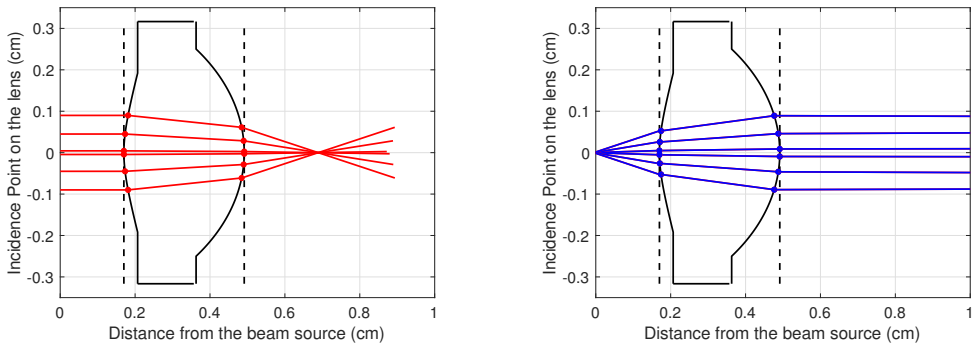

(A) (B)

FIGURE 4.18: (a): Example of Ray Tracing for a beam of waist $w_0 = 300\mu m$. (b): Ray Tracing for low values of source beam waist, $w_0 = 5\mu m$. The lens is able to collimate the highly divergent beam, for lens position close to the focal length of the lens.

waist is located. The dotted points indicate the intersections between the beam and the two lens surfaces, (x_i, y_i) at the entrance surface and (x_o, y_o) at the lens exit, in eq. 4.37.
The beam width was evaluated, as a function of the propagation distance after the lens. The width of a beam described by the field $E(x, y)$, is evaluated through the following formula[116]

$$w_x = \sqrt{4\frac{\int_{-\infty}^{\infty}\int_{-\infty}^{\infty} x^2 \left|E(x,y)\right|^2 dxdy}{\int_{-\infty}^{\infty}\int_{-\infty}^{\infty} \left|E(x,y)\right|^2 dxdy}} \tag{4.40}$$

An analogous relation holds for the y component. Differently from the well known expression of the Gaussian beam width, the expression in eq. 4.40 is valid also also for beams, that cannot be described within the Gaussian formalism.
The obtained results were compared with the behavior of a paraxial Gaussian beam, incident on a spherical lens of focal length equal to the effective focal length of the aspheric lens under testing. This last is, as declared by the vendor, equal to $f = 3.1mm$, at a wavelength of $0.83\mu m$. We account for the focal shift caused by the used wavelength of $1.58\mu m$, by evaluating the refractive index dispersion of the lens glass (D-ZK3), shown in figure 4.19. The red point indicates the wavelength of interest. From the lensmaker's equation an effective focal length of $f = 3.15mm$ is estimated.

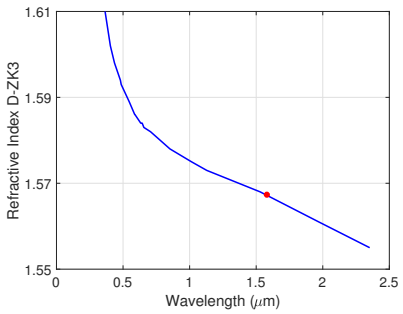

FIGURE 4.19: D-ZK3 refactive index as a function of the beam wavelength. The red point indicates the wavelength of interest.

As figure 4.20a, 4.20b show, the description seems to agrees pretty well with the Gaussian beam behavior (indicated by the dashed black lines), for several values of the initial beam waist.

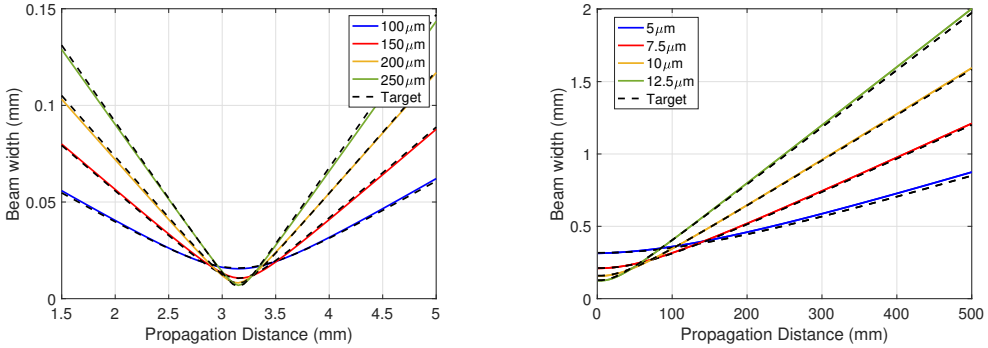

(A) (B)

FIGURE 4.20: (a): Beam width, as a function of the propagation distance after the lens. The different curves refer to different waist values, given in the legend. The black dashed lines indicate the expected behavior, from a full Gaussian modeling. (b): Beam width, as a function of the propagation distance after the lens. The different curves refer to different waist values. The black dashed lines indicate the expected behavior from a full Gaussian modeling. The values of propagation distance are referred to the center of the lens.

However, for a further decrease in the source beam waist, remarkable discrepancies between the lens model and the Gaussian behavior are observed, as shown in fig. 4.21a. The differences can be attributed to several reasons. A first reason could lie in the intrinsic difference between the Gaussian behavior, which is an approximate solution, and the non-approximated beam, direct solution of the Rayleigh-Sommerfeld diffraction integral. Indeed, the the beam profile considerably deviates from the Gaussian profile, as shown in fig. 4.21b.
Another reasons could lie in the model itself. A possible error can be the evaluation of θ_1 and θ_2[7], especially for values of r close to the lens boundary, and θ_b.
Another reason could be found in the approximation made to analytically find the intersection points between the optical ray and the lens. Here, we first supposed the surface is described by only the first term in eq. 4.34, as expressed by

$$S'(x) = \frac{x^2}{R\left(1+\sqrt{1-(1+\kappa)\frac{r^2}{R^2}}\right)} \tag{4.41}$$

Then, the contribution of the aspheric coefficients was included in a correction factor, δ

$$\delta = a_4 r^4 + a_6 r^6 + ... \tag{4.42}$$

which expresses the difference between S and S', at the lens input plane.

[7]The relations $\sin(\theta_{1,2}) = r/R_{1,2}$ in eq. 4.36 is valid for spherical surface. For an aspheric surface this relation is an approximate solution.

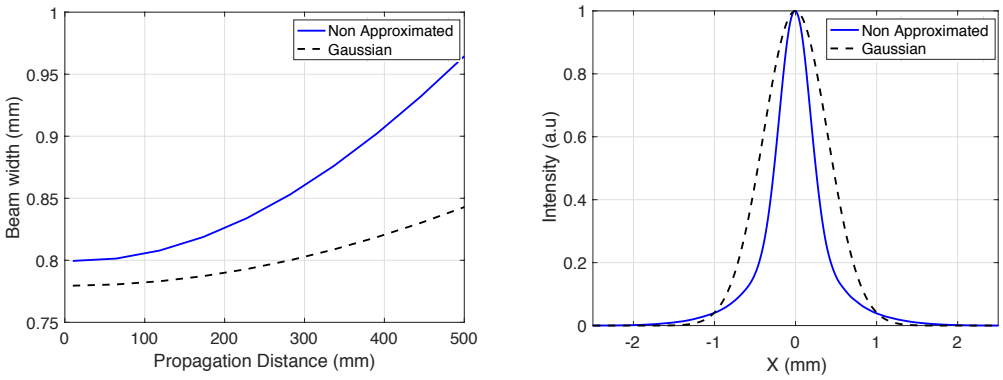

(A) (B)

FIGURE 4.21: (a): Beam width as a function of the propagation distance, for small beam waist. The discrepancy between the simulated result and a ideal gaussian beam (the dashed black line) are clearly visible. (b): Comparison between a Gaussian beam profile, at the exit of a spherical lens and the non-approximated beam, at the exit of the simulated aspheric lens.

Finally, the output coordinate points are given by the solution of the following equations

$$\begin{cases} m(x_o - x_i) = y_i + \dfrac{x_o^2}{R\left(1 + \sqrt{1 - (1+\kappa)\frac{x_o^2}{R^2}}\right)} + \delta \\ y_o = S(x_o) \end{cases} \tag{4.43}$$

where m is the angular coefficient of line going from (x_i, y_i) to (x_i, y_i), equal to

$$m = \tan(\pi/2 - \alpha) \tag{4.44}$$

A pragmatic way to validate the model is to compare the results with the experiment. However, as explained in the following section, this measurement is not easy to performed.

4.3.3 SOA beam

The estimate of the optical beam intensity profile, at the output of the waveguide in the active region of the SOA, is far from being trivial. Because of the high divergence of the beam, the aspheric lens needs to be carefully chosen. The chosen one (the Thorlabs C330TMD-C lens) has a numerical aperture equal to $NA = 0.7$ and an effective focal length of 3.15 mm. The high numerical aperture limits truncation effects, however such a short effective focal length makes difficult the exact determination of the beam profile due to the uncertainty on the lens position, which is accentuated in the implemented set-up because of the used lens mounts, as shown in fig. 2.15b. The bulky dimensions of the gain block make prohibitive an exact measure of the lens position. Furthermore, the lens positioning mechanical system is not stable in time, and small variations can considerably influence the results. The beam profile was measured at the lens output for several propagation distances and

for different values of the lens position. Figure 4.22 shows some of the measured profiles.

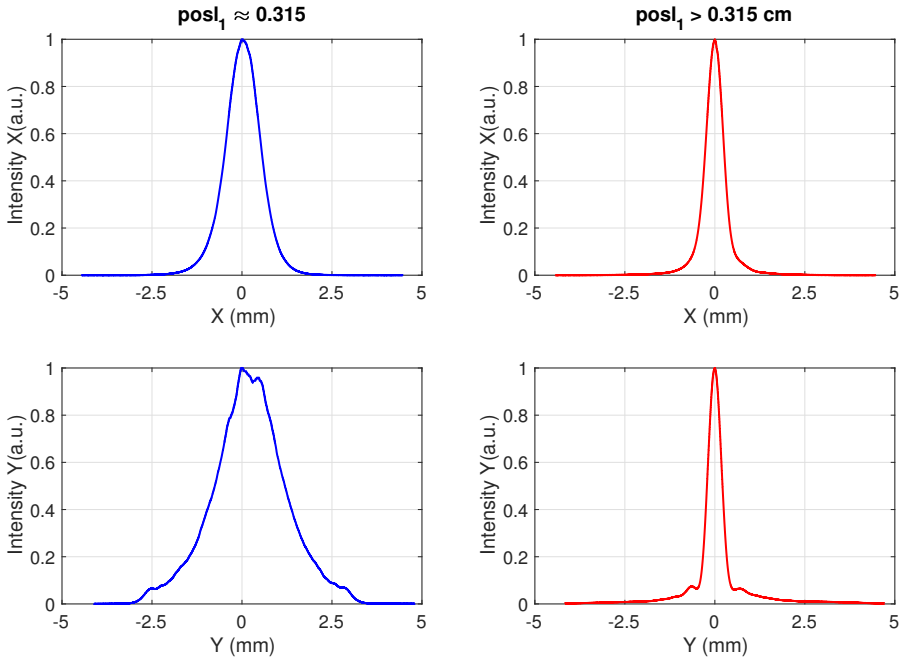

FIGURE 4.22: Examples of the profiles measured, for both the X (upper panels) and Y (lower panels) directions. The blue and red curves refer to two different lens positions, and are taken at two different distances from the lens, $d = 7.5cm$ for the blue curves and $d = 64cm$ for the red curves.

Here we assume that the X is parallel to the waveguide (slow axis), while Y is perpendicular (fast axis). From the data, we can observe that the X profile is more close to the Gaussian profile, than the one along the Y directions. This is due to the shape of the active waveguide (see fig. 2.12 in Chapter 2).
Figure 4.23 shows the behavior of the beam width as a function of the position, after the lens, for two different lens positions with respect to the SOA output facet.
We tried to fit the obtained data, using both the Gaussian propagation law and the proposed model, through an optimization algorithm. In the procedure, both the beam waist and the lens position were varied. The algorithm returns the couple of values, that better reproduce the experimental data.
Unfortunately, no models fit the data. This can be attributed to several reasons. The firsts are measurements errors. These last are, in turn, associated to the beam profiler position, or to variations of the lens position during the measure. Also a small tilt can influence the measure. A second reason is the SOA beam profile. As a matter of fact, it was always assumed that the beam quality equals the one of a Gaussian beam, meaning $M^2 = 1$. A different value of M^2 can significantly alter the beam propagation. Because of the experimental set-up, and in particular of the lens position system, the measure of the M^2 cannot be performed with the needed accuracy.
In order to give an estimate of the beam waist, we fit the measured beam profile, for several measures, taken approximately at the same lens position, with the diffraction model. Figure 4.24 shows an example of the comparison between the measured beam, the blue dotted curves, and the simulated beam, the red curves.

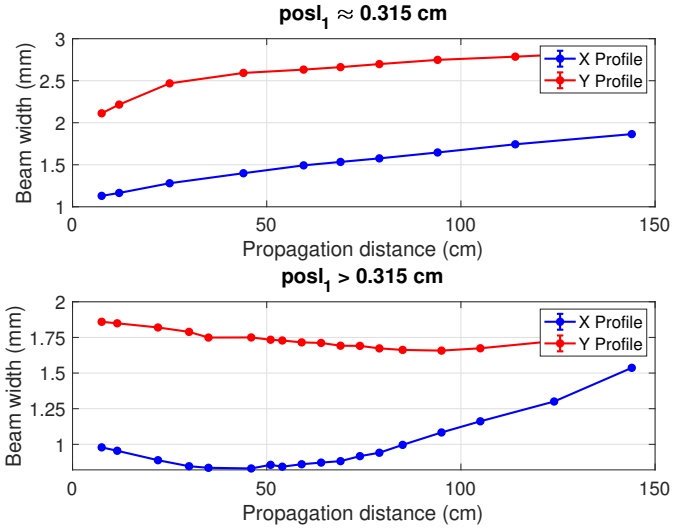

FIGURE 4.23: Beam width as a function of the propagation distance, for two different positions of the lens. The blue curves refer to the X profile, while the red ones are related to the Y direction.The error bars are contained in the experimental points.

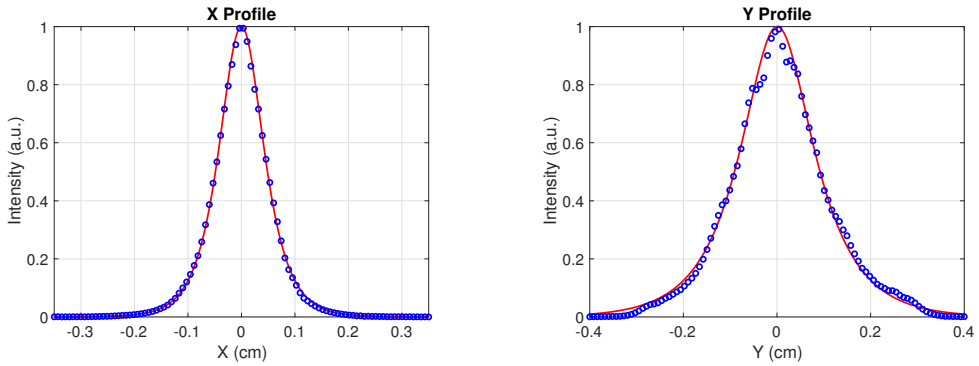

(A) (B)

FIGURE 4.24: (a): Comparison between the measured beam profile and the simulated one by the aspheric lens model, for the X component. (b): Comparison between the measured beam profile and the simulated one by the aspheric lens model, for the X component.

The beam waist was estimated as the mean value of the results obtained from the different fitting procedures. It was found $w0_x = (3.4 \pm 0.4)\mu m$ and $(w0_y = 2.5 \pm 0.6)\mu m$.

Then, we used these values to model the beam width evolution (figure 4.23) with the introduction of the M^2 propagation factor. Both M^2 and the distance between the lens and the location of the beam waist are fit parameters. Figure 4.25 shows the results. It is observed that the model reproduces correctly the X component, but it almost fails for the Y component.

The reason can be attributed to the failure of the initial assumption that the emitted profile can be approximated with a Gaussian one. The fit returned $M_x^2 = 2.33 \pm 0.06$ and $M_y^2 = 3.1 \pm 0.3$, while $pos_x = (3.157 \pm 0.1)mm$ and $pos_y = (3.152 \pm 0.001)mm$. The different values of the lens position with respect to the location of

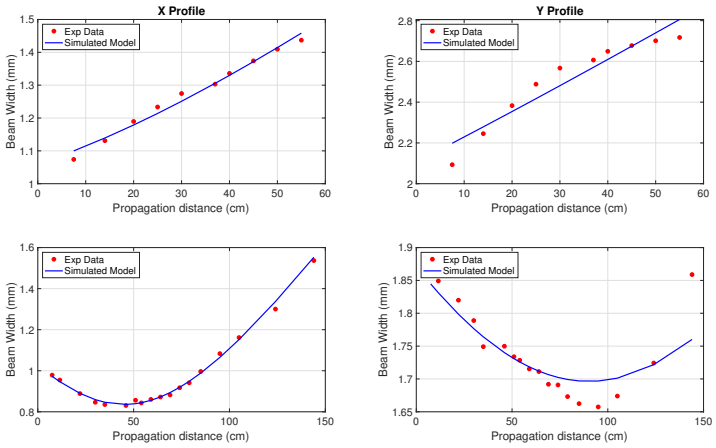

FIGURE 4.25: Beam width as a function of the propagation distance. The red points indicates the experimental data, while the solid blue curves the fit curves.

the beam waist, for the two components, correspond to an astigmatism of approximately equal to $5\mu m$, which is typical for diode laser [117].
To understand the origin of the fit failure for the Y component, we tried to measure the profile at the exit of the SOA without the use of the collimating lens. Because of the high beam divergence, only a single measure was taken, shown in fig. 4.26.

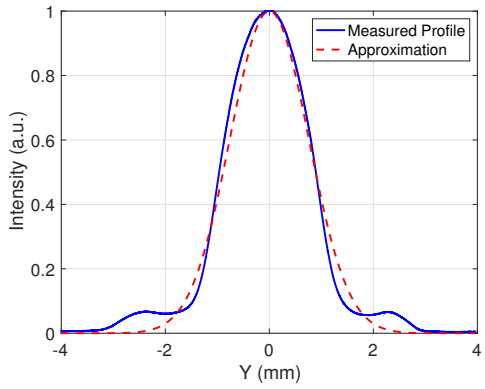

FIGURE 4.26: Measure of the Y component at the output of the SOA.

The presence of the two side lobes can influence remarkably the beam propagation and the error committed made assuming a Gaussian description, the red dashed line in fig. 4.26, cannot be considered negligible. The exact determination of the beam profile requires the knowledge of the waveguide structure, which for this amplifier was not knowing. Therefore, an approximate description is mandatory.

4.3.4 Laser design

The resonator stability region can be identified by evaluating the power overlap integral between the estimated SOA field and the beam obtained after a round trip along the cavity. The folded ring cavity consists of two equally curved mirrors (CMs), with a curvature radius equals to $R = 40cm$. A sketch of the ECL design is reported in fig. 4.27, where a indicates the distance between the two CMs, $c = d$ is the length

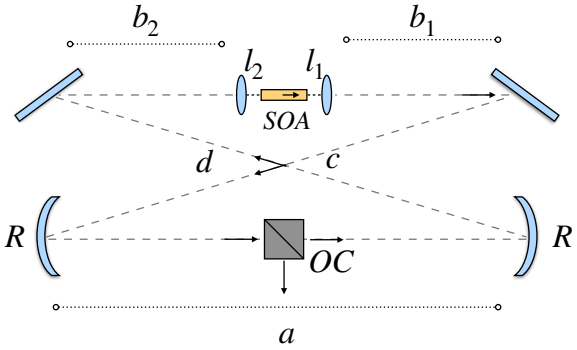

FIGURE 4.27: Sketch of the studied ECL.

of the diagonal arms, while b_1 and b_2 stand for the distance between the plane mirrors (PMs) and the two lenses. OC indicates the Ouput Coupler position. Finally, l_1 and l_2 are the two lens positions. The index 1 refers to the collimating lens, while 2 stands for the focusing lens, as highlighted in fig. 4.28. The lens collimating the SOA

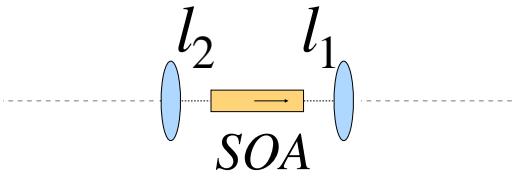

FIGURE 4.28: Gain block. SOA, collimating lens l_1 and focusing lens l_2

beam is placed at a position such as to collect the maximum amount of power and simultaneously minimize the beam divergence. Ideally, this situation corresponds to put the lens at a distance equal to the effective focal length, from the SOA emission facet. The focusing lens position is varied to maximize the coupling efficiency.
The power overlap integral, defined in eq. 4.9, is evaluated for different values of the cavity arm lengths. To reduce the variables, the cavity is designed in order to be symmetric. Therefore, $a = b_1 + b_2 + L + l_1 + l_2$, with L being the SOA length, and $c = d$. Figure 4.29a shows the obtained results, when both a and c are varied. The yellow regions correspond to the regions where the coupling efficiency reaches its maximum value. The corresponding resonator configurations identify the stability region. The map reflects the difference in the beam, emitted in the two different direction. According to the simulation model, the aspheric lens shows a slight focal shift for the Y profile, caused by the higher divergence angle. This surely affects the power overlap integral, and explains the obtained map. This means that also the collimating lens position, needs to be tuned to maximize the coupling in a given configuation. Figure 4.29b, shows the variation of the power overlap integral, in a given resonator configuration, for different values of the two lenses position. An interval of l_1 and l_2 which yields high power overlap integral is observed. It is important to mention that the absolute values of the coupling efficiency reported, are ideal values. According to our previous discussion, we expect to see in the experiment a variation of the coupling losses caused by the nonideality of the beam profile. The use of the simpler Gaussian propagation law returns values of coupling efficiency as high as 90%, which are not consistent with the measured result.
From the consideration made, it is clear that, in such a ECL the two lenses have a essential role. Both of them strongly influence the coupling efficiency, while the

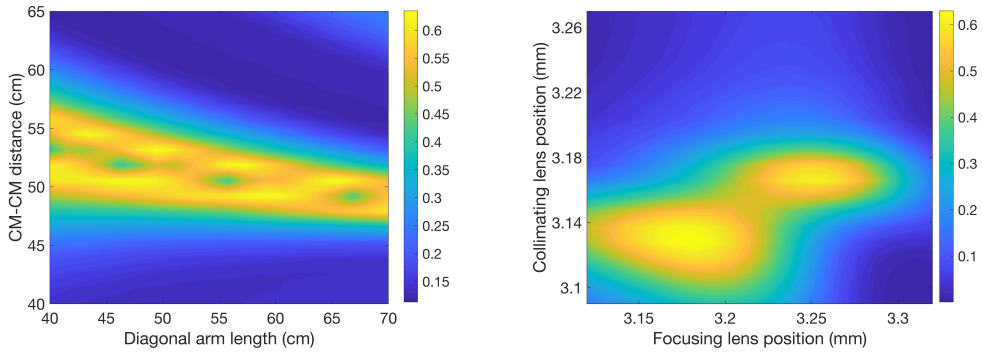

(A) (B)

FIGURE 4.29: (a): Power overlap integral for different values of the cavity arm lengths, and curved mirror distances. The position of the lenses were$l_1 = 0.316\,cm$ and $l_2 = 0.32\,cm$. These values are referred with respect to the center of the lens.The color bar on the right refers to power overlap integral values.(b): Power overlap integral as a function of the lens positions, when $a = 50cm$ and $c = d = 55cm$.

collimating lens entirely determines the beam characteristic at the output of the resonator.
To estimate the laser output power, the field evolution within the resonator, after several round trips is studied.

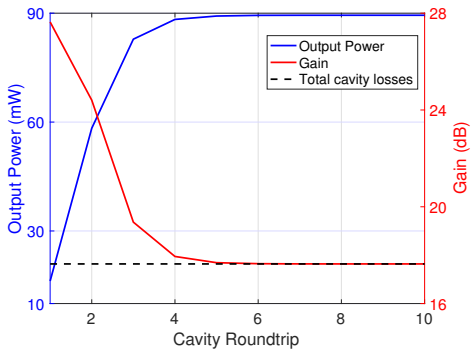

FIGURE 4.30: Laser output power (blue curve) and saturated SOA gain (red curve) as a function of the number of cavity roundtring along the resonator. the dashed black line indicates the total cavity losses. In the simulation we fixed $\lambda = 1.58\,mum$. The injection current was set to $500mA$, corresponding to $G_0 = 28dB$ and $P_s = 18dBm$. The cavity arms lengths are $a = 50cm$, $b_1 = a/2 - l_1 - L/2$, $b_2 = a/2 - l_1 - L/2$,$c = d = 55cm$, with $L = 0.15$ the SOA length . The lens position were fixed equal to $l_1 = 0.316cm$ and $l_2 = 0.325$. This last was chosen to maximize the power overlap integral.

The ASE emitted from the amplifier starts the laser oscillation and travels towards the OC. Here, according to the OC reflectivity, a first portion exits from the cavity, while the remaining travels towards the gain medium where it undergoes amplification. The field propagation is described through the diffraction integral in eq. 4.14. The aspheric contribution is described by the factor in eq. 4.39, while the phase imparted by the curved mirrors is given by the expression in eq. 4.29, where $f = R/2$.

The gain saturation is described through eq. 2.30.
We evaluate the losses imparted on the beam by each optical component in the cavity. The total losses during a cavity round trip were found to be equal to $\alpha_{cav} = -0.80 \pm 0.01 dB$.
Figure 4.30 shows the output power as a function of the beam roundtrips. A stationary state is reached, after ≈ 5 roundtrips. In such a state, the saturated gain reaches the value of the total cavity losses. The contribution to these last is given by the optical components, the SOA coupling condition and the OC reflectivity.

4.3.5 Experimental Results

The ECL was experimentally tested in one of its configuration. More in details, $a = 50\,cm$, $c = d = 55\,cm$, $b_1 + l_1 + b_2 + l_2 + L \approx a$, with $L = 0.15cm$ being the SOA length. The OC consists of a variable polarized beam splitter, which allows us to evaluate the laser performance as a function of the OC reflectivity. Furthermore, a free space optical isolator was placed in front of one of the two SOA facets, to force the beam propagation along a single direction, and cut the contribution of the ASE emitted in the opposite direction. The two lenses were aligned in order to maximize the laser output power. The laser power was collected at the cavity output, for different values of the SOA injection current. Figure 4.31 shows the results.

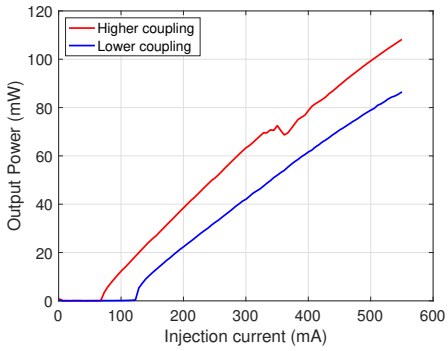

FIGURE 4.31: ECL Experimental results. Output Power as a function of the SOA injection current. The red curve refers to a low value of coupling losses, while the blue for larger coupling losses.

The two curves refer to two different coupling conditions. The red one is obtained when the lenses in the gain block maximize the power overlap integral. As expected, for the two cases, a clear threshold behavior can be identified. The value of the threshold current depends on the total cavity losses. It is therefore higher for the blue curve. A kink appears in the red curve [118]. The kink is one of the reasons for the power limitation in single mode diode lasers. Its appearance is associated with the simultaneous oscillations of higher order transversal modes. Their origin is caused by perturbations in either the SOA refractive index or in the gain profile. These, in turn, are due to the high power circulating in the SOA, which can provoke an increase of the temperature or inhomogeneities in the local carrier population. Since the coupling is lower for the blue curve, no kink is observed.
The laser emission spectra was collected as a function of the injection current.
The spectra were taken at by an OSA with a Video Bandwidth (VBW) equals to

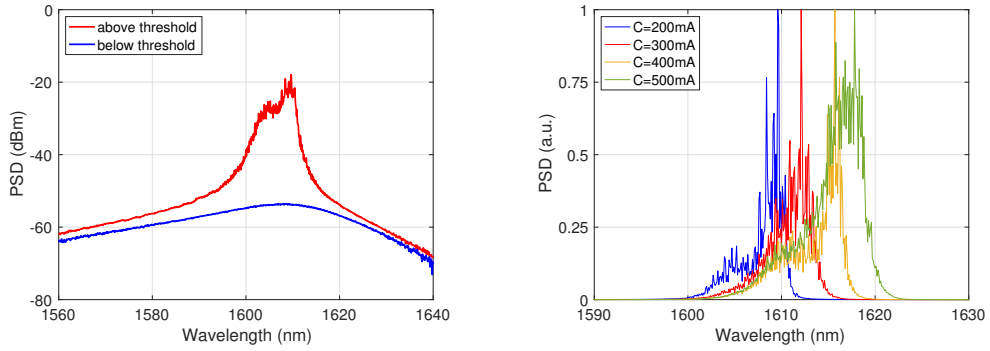

(A) (B)

FIGURE 4.32: (a): ECL Power spectral density (PSD) below (blue curve) and above (red curve) the threshold value of the injection current. The data are reported in logarithmic scale. (b): Emission spectra for several values of the injection current (linear scale). The spectra are normalized according to their maximum value.

$100Hz$ and a resolution of $0.05nm$. Figure 4.32a shows that the spectrum clearly narrows as soon as the injection current reaches the threshold value. Furthermore, the contribution of the different longitudinal modes of the cavity is visible, as shown in fig. 4.32b. The emission peak, with the increase of the injection current, shifts towards longer wavelength. The ECL peak shift can be associated with nonlinear phenomena, caused by the power increase, altering both the gain and the refractive index of the active medium. Finally, an increase of the emission bandwidth with the current is observed. The effect can be explained with the fact that, an higher value of the injection current corresponds to an higher gain for more wavelength components, within the gain emission profile of the SOA.

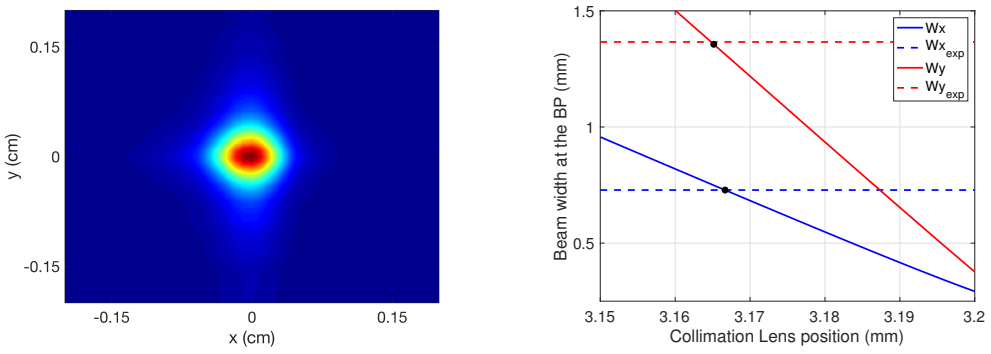

(A) (B)

FIGURE 4.33: ECL Beam Profile. (a): Laser beam profile, measured at $15cm$ form the OC. (b): Beam width for different values of the collimating lens position. The dashed lines indicate the measured value.

The laser beam profile, collected at a distance of $15cm$ from the output coupler, isshown in figure 4.33a. From this measure we can estimate the position of the collimating lens. Figure 4.33b shows the expected beam width as a function of the lens position. The dashed line indicate the measured value. The predictions and the measurements coincide when the collimation lens is at a distance of approximately

$l_1 \approx 3.166mm$, indicated by the black dots in the figure. From this value we can estimate the focusing lens position that maximize the power overlap integral. We found $l_2 \approx 3.25mm$, corresponding to a value of the coupling efficiency equal to 49%.
Finally, the laser output power was collected also for several values of the OC reflectivity, when $I = 500mA$. The reflectivity was varied by the rotation of the half-wave plate, placed in front of the cavity OC. Figure 4.34 shows the results and compares the obtained values, red points, with those expected from the iterative simulation procedure, previously described in this section, the solid blue curve. The values used in the simulation for the lens positions are those estimated through the measure of the beam width.
A very good agreement between the model and the experimental results is shown. This validates the model.

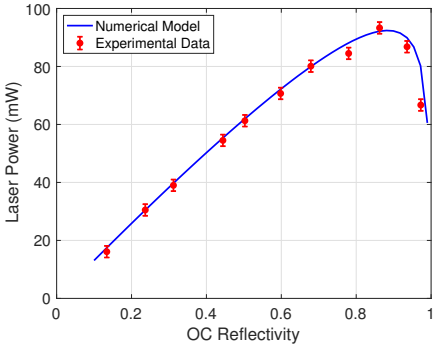

FIGURE 4.34: Output Power as a function of the OC reflectivity. The red point indicates the experimental data, while the solid blue curve the simulated results obtained by the iteration procedure, described at the beginning of this section.

Chapter 5

Interferometric Laser

The model developed for the standard ECL is needed for the study of the proposed power scaling architecture. Both the cavity design and the choice of the optical elements are crucial for reaching the optimum performance. The proposed design was first tested for a single gain stage. This proves the idea and validates the theoretical model. Then, the power scaling architecture was proved with two gain media.

5.1 Laser output power: Ideal condition

An interferometric laser can be thought as an ECL, where the SOA is replaced by the ISA, or the ISAs sequence. Let us first study the behavior of the interferometric laser when only a single gain stage is present. The idea of the laser system is shown in fig. 5.1.

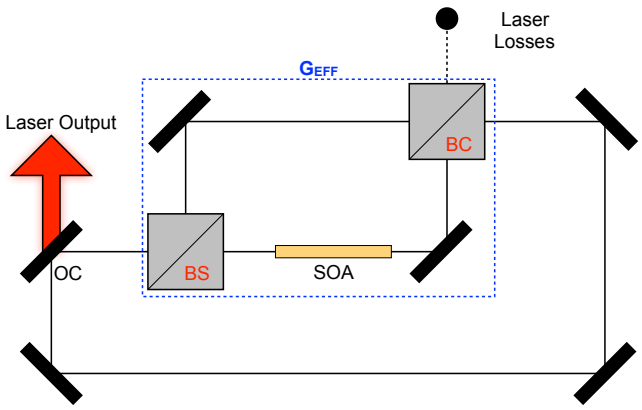

FIGURE 5.1: Scheme of the ring cavity single stage interferometric laser.

The preliminary study was performed only to evaluate the laser output power. At a first approximation, such a system can be studied by replacing the SOA gain, in the ECL model, with the ISA effective gain, obtained in eq. 3.8. Therefore, the whole ISA block can be viewed as an effective gain medium. Also for this device, the laser operates when the stationary state is reached. This state reflects the condition in which the total saturated effective gain equals the total cavity losses. If L indicates the total cavity losses, while R_{oc} refers to the output coupler reflectivity, in the stationary state it can be easily shown that the total gain is equal to

$$G_{eff} = \frac{1}{L\,R_{oc}} \tag{5.1}$$

In such a situation the intracavity power, P_c, after a round trip equals the power circulating in the amplifer, while the laser output power is simply given by

$$P_{out} = T_{oc} P_c \tag{5.2}$$

with T_{oc} being the output coupler transmittivity, $T_{oc} = 1 - R_{oc}$.
The laser was first analyzed in an ideal situation. Similarly to the ISA study, it was first assumed that the interferometer arms are perfectly balanced and that the no loss condition is verified. Under these assumption eq. 5.1 transforms into

$$|\sqrt{G}\, t_{bs}\, r_c + t_c\, r_{bs}|^2 = \frac{1}{L\, R_{oc}} \tag{5.3}$$

with the index bs referring to the first beam splitter (BS), while c to the beam combiner (BC), such that $t_c / r_c = r_{bs} / \sqrt{G} t_{bs}$ (eq. 3.7).
Assuming a total cavity loss equal to $L = -3dB$, figure 5.2a shows the laser output power as a function of the OC reflectivity, for different BS reflectivities. Figure 5.2a shows the corresponding values of the BC reflectivity. The simulations were performed at a wavelength of $\lambda = 1.58\,\mu m$, for an injection current of $500 mA$.

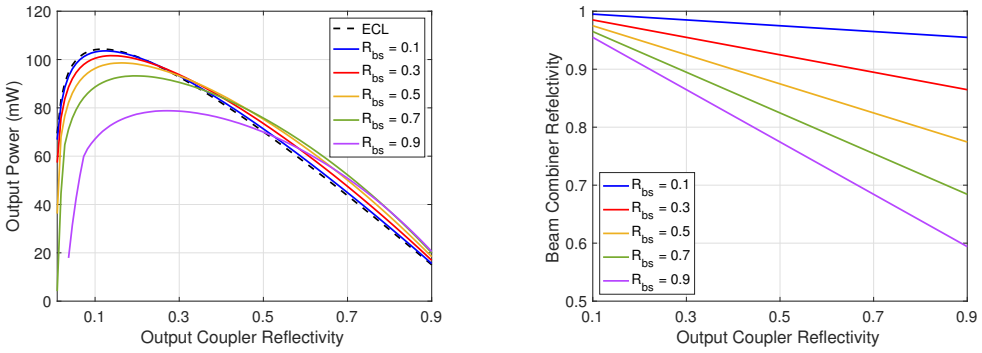

(A) (B)

FIGURE 5.2: (a): ISA ECL output power as a function of the OC reflectivity. The different curves refer to different values of R_{bs}. The dashed black line indicates the SOA ECL behavior. (b): Beam combiner reflectivity, R_c, as a function of the OC reflectivity, for different values of R_{bs}.

The laser output power, when only a single stage is implemented, decreases with the increase in the beam splitter reflectivity. This is associated with the decrease in the small signal effective gain[1].
Nevertheless, the result should not discourage, because the main goal of the device is offering a new combining strategy, thanks to the the addition of multiple gain stages. Thanks to the theory developed in Chapter 3, the multi-gain laser device, depicted in fig. 1.12, can be simply studied using the effective gain expression valid for the ISA sequence, given by eq. 3.18. Similarly to the amplifier sequence, also in this case, we initially assumed that the incident power on each gain medium remains the same, at each consecutive stage. The condition implies that all the SOAs operate at

[1] See fig. 3.2d in Chapter 3

the same value of the saturated gain. Furthermore, we assume the validity of the no loss condition at each beam combiner.
Figure 5.3 shows the increase of the laser output power with the number of gain elements composing the device. The two different solid curves refer to different values of the initial beam splitter reflectivity, while the black dashed line indicates the power scaling, achievable when incoherently combining N standard ECLs. The simulations were performed assuming the ideal case in which the only cavity losses are those imparted by the cavity OC.

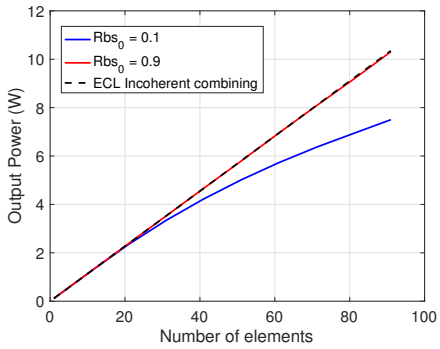

FIGURE 5.3: Interferometric laser output power as a function of the elements composing the ISA sequence. Rbs_0 is the reflectivity of the first beam splitter, at the entrance of the sequence. The dashed line shows the total power when combining N standard ECLs.

The proposed architecture seems to be promising. By comparison between the blue and the red curves, we can deduce that the fundamental ingredient for the success of the new combining scheme is the power reduction in each amplifier, with the consequent increase of the output saturation power. The comparison beween the red solid line and the black dashed line shows that, for high values of Rbs_0 in the ideal working condition, the proposed architecture achieves the optimum combining efficiency. The reason is associated to the combined action of the intra-cavity coherent combining, on the power dependence of the ISA sequence effective gain (eq. 3.18 in Chapter 3) and on the ISA sequence behavior of saturation power (fig. 3.5b in Chapter 3).

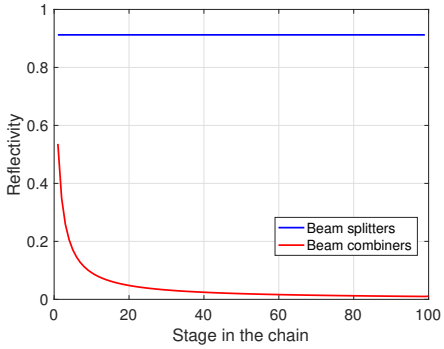

FIGURE 5.4: Reflectivity of the optical components in the laser device, as a function of the gain stages. The blue curve indicates the beam splitters in the gain arm, while the red curve refers to the beam combiners, placed in the upper arm of the device.

Finally, figure 5.4 shows the optimal values of the reflectivities, of all the beam splitters and combiners present at each sequence stage, when the total number of elements is equal to 100 and $R_{bs} = 0.9$. While the beam splitters reflectivity remains equal for each gain stage, the beam combiners reflectivity should decrease as the stage number increases. Inevitably, this particular behavior represents both a technological and a physical limit to the total number of stages, that can be implemented in the laser device.

5.2 Phase difference and interference

In the reality, the interferometer arms in our design are always unbalanced, because of the presence of the gain medium in only one arm of the interferometer. Furthermore, as already mentioned, the power dependence of the SOA refractive index makes difficult the compensation of the optical phase difference through passive strategies, such as, for example, the implementation of a free space optical delay line.
Therefore, in presence of a certain phase difference, when the ISA is placed within the resonator, different wavelengths undergo different amplification. Depending on the resonator geometry and on the optical components, the laser oscillation can be reached, and sustained in time, only for certain wavelengths. The red curve in figure 5.5, where the behavior of the laser power with the number of cavity round-trip is reported, represents a clear example of this.

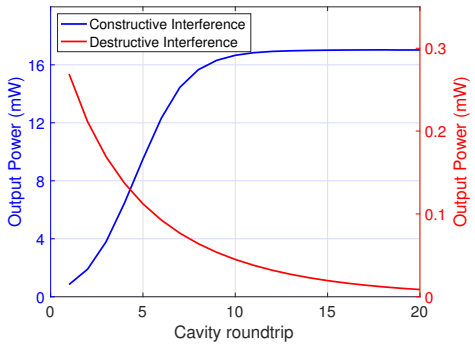

FIGURE 5.5: Laser output power, for different cavity round trips, for two different values of the wavelength ($\lambda = 1.5802\,\mu m$ for the red curve, while $\lambda = 1.5805\,\mu m$ for the blue curve), when$\delta d = 0.48cm$. The simulation were performed for a cavity loss equal to $-3dB$, while $Rbs = 0.9$,$R_{OC} = 0.3$ and $R_c = 0.15$. The value of R_c was chose to maximize the output power visibility (see eq. 3.22 in Chapter 3).

As a consequence, similarly to what we have seen with the ISA case study, interference fringes will appear and the presence of some losses at the exit of each beam combiners is inevitable.
Of course, the implementation of active control stages is possible and allows the achievement of all of the advantages seen in the previous section. Nevertheless, the addition of control stages, for this particular architecture, especially in a free space configuration, increases the complexity of the device, which could not represent a feasible solution in a not controlled environment. For this reason, we tested the novel design of the ISA ECL in absence of active phase controllers. In this situation, the power measured both at the output of the laser device and at the exits of each beam combiners, will be an average between the maximum and the minimum of the

interference fringes. The choice of the optical components can be optimized, in order to maximize the laser output power and simultaneously minimize the laser losses. Let us initially consider only a single stage ISA ECL, with $R_{bs} = 0.9$ and a $\delta d = 0.48cm$, with δ being the difference between the two interferometer arms lengths (eq. 4.42 in Chapter 3). Through an optimization procedure, the reflectivities of the OC and Rc were varied until the best performance is reached. This is achieved when $R_{oc} = 0.2$ and $R_c = 0.99$. Figure 5.6a shows the wavelength dependence of the laser power at the straight port of the beam combiner (P_c), and of the signal exiting from the unusable port of the BC (which is a source of loss for the ISA ECL), in the optimum configuration. The colored dashed line indicates the average values, that will be eventually measured, while the dashed black lines shows the ideal values, under the condition $\delta d = 0$. The presence of some losses also in absence of a phase difference, is related to the different visibility at the two exits of the beam combiner, as explained in Chapter 3, when R_c is not perfectly chosen.
We evaluated the variation of the multi-gain laser output power, when $\delta d \neq 0$ and each optical component is optimized. Figure 5.6b shows the obtained result up to $N = 100$, in the ideal case of null intra-cavity losses.

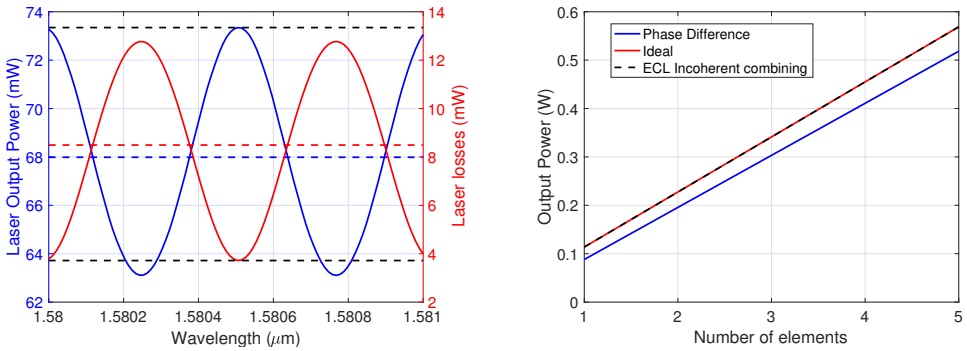

(A) (B)

FIGURE 5.6: (a): Laser output power (the blue curve) and laser losses (red curve), as a function of the wavelength. The colored dashed lines indicates the average values, while the black dashed lines refers to the ideal performances, in absence of any phase difference, for the given configuration ($R_{bs} = 0.9$, $R_c = 0.99$ and $R_{OC} = 0.2$). (b) Output power for the multi-gain laser device as a function of the number of SOAs. The blue line is the result when a phase difference δd is assumed, while the red line refers to the ideal case. The black dashed line reports the power scaling achievable with the incoherent combining. The simulation were performed assuming the ideal case in which the cavity losses are those imparted by the cavity OC.

As expected, a slight decrease of the laser output power is observed. Nevertheless, the architecture still offers a valid and solid alternative for power scaling, also when working under non ideal conditions.

5.3 Design revisited

In the previous sections, we demonstrated that the realization of a robust combining architecture is possible, when each single optical components is chosen in an

appropriate way. Therefore we moved to the experimental validation of the idea. In particular, we want to prove the advantage of the power reduction, circulating on the amplifier, for power scaling purposes. As outlined in the previous section, the presence of some losses at the beam combiner describes a non ideal solution, that could affect the validation of the idea, at least for a small number of combined SOAs. For this reason, to avoid this limitation, the laser design was revisited. Figure 5.7 shows a sketch of the new laser design, when only a single gain stage in present.

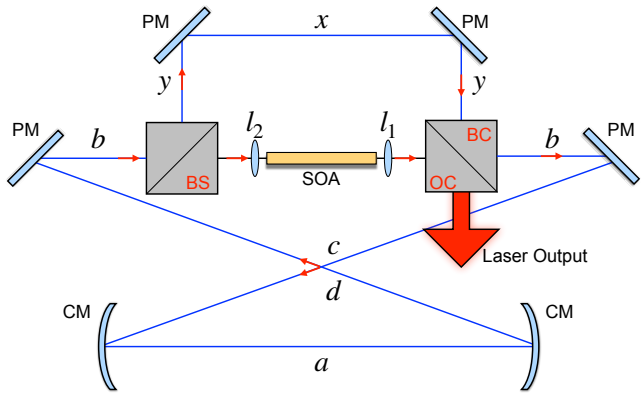

FIGURE 5.7: Sketch of the revisited design.

Also in this case, the addition of sequential stages is possible. However, supplementary considerations, postponed to the next sections, are needed.
Two main differences, with respect to the previous design, can be highlighted. The first one regards the beam combiner, that, here, acts also as the cavity OC, avoiding the presence of unwanted optical losses. The second variation is the increase, in the new scheme, of the optical path difference between the two arms of the interferometer. The result is a decrease of the interference fringes frequency spacing. This could represents a drawback if an active phase control stage needs to be implemented, because of a more difficult phase balancing. However, since here we are interested in a passive architecture, the laser output power is not influenced by the increase in the path difference.
The study of the new architecture, cannot be reduced to the simply description of an effective gain, as in the previous design. For this reason, to evaluate the laser performances the iteration procedure (outlined in Chapter 4) is again used to study the field evolution after several roundtrips. Also in this case, we expect a stationary state, corresponding to the laser working condition.

5.3.1 Modeling

The ASE emitted from the SOA is, obviously also for this device, the responsible for the starting of the laser oscillation. The emitted beam travels towards the beam splitter. Here a portion of the beam will undergo amplification, while a second portion travels along the upper arm of the interferometer. At the beam combiner, the interference of the two beams occurs. Here, the combined beam is in turn split in a first part that will contribute to the laser output power, and in a part which will sustain the laser oscillation.

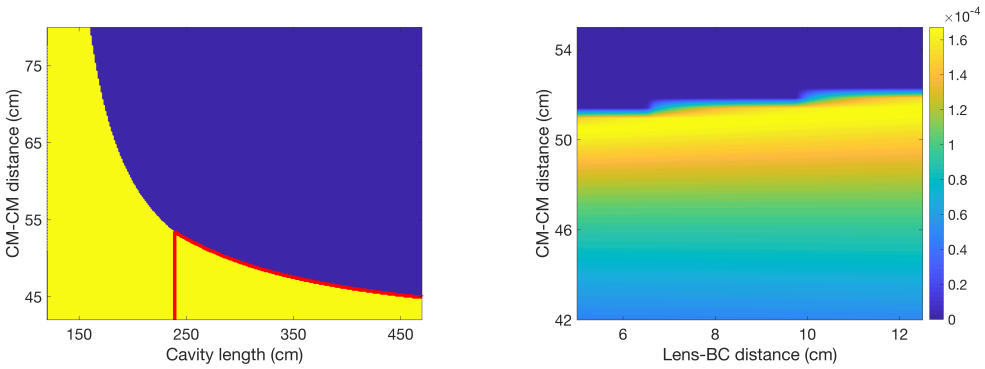

(A) (B)

FIGURE 5.8: (a): External cavity stability region. The yellow region identify the stable configuration. The red lines indicates the regions of interest for our experimental set-up. (b): Excitation efficiency, as a function of the distance between the two CMs and of the distance between the collimating lens l_1 and the BC. The yellow regions corresponds to the resonator configuration characterized by a higher value of the excitation efficiency between the SOA emitted beam and the external cavity mode distribution.

Similarly to the case of the standard ECL, the strategy to correctly design the interferometric laser resonator involves the individuation of the stability region, corresponding to all the resonator configurations characterized by lower values of coupling losses. These last, at each round trip, are evaluated according to the power overlap integral between the SOA waveguide mode and the result of the interference of the beams traveling in the two separate arms.
On the other hand, the whole device can also be viewed as an external passive resonator, whose geometry is indicated by the blue line in figure 5.7, whose mode distribution is excited by the SOA emitted beam. Therefore, the choice of the resonator geometry, should consider also the external resonator configurations in which the self-consistency condition is verified. This last can be easily found, according to the theory presented in Chapter 4. Finally, to fully exploit the potential of the external resonator, the laser geometry should maximize the excitation efficiency of the external cavity modes.

Figure 5.8a shows the stability graph for the external cavity. The stable resonator configurations corresponds to the yellow region in the map. Because of some geometrical constraints in our experimental set-up, the regions of interest are only those lying in the area identified by the two red lines. Figure 5.8b shows the excitation efficiency of the external cavity modes by the SOA beam. Also in this case the geometrical constraints of our set-up [2], limits the achievement of a good excitation efficiency. Because of the small values of excitation efficiency (the maximum value is $\approx 1 \times 10^{-4}$, as reported from the color bar in fig. 5.8b), the mode structure of the external cavity is not sufficiently excited. For this reason, the ISA ECL output beam profile is entirely determined by the SOA beam properties and by position of the collimating lens. A further development in the cavity design, should be devoted to the increase of the excitation efficiency of the external cavity mode distribution. For higher values, the laser output profile is highly influenced by the external cavity

[2] Among there are the bulky dimensions of the used mounts in the gain block and of the used optical components in the cavity, and the incidence angle condition on the CMs

mode distribution. The interplay between the different transversal modes of the external cavity, can also represent a valid tool for beam shaping applications.
In order to have a higher number of stable configuration, a $4f$ system is placed in the upper arm of the interferometer, as shown in fig. 5.9.

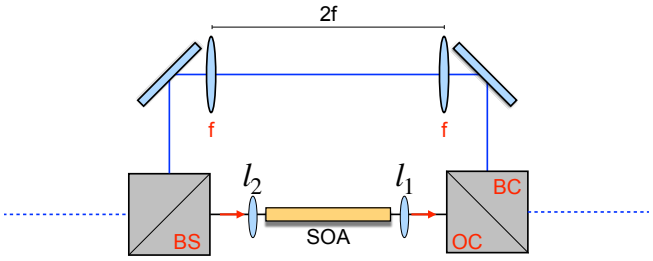

FIGURE 5.9: Image of the implemented 4f system. The two lenses, are placed respectively at a distance f from the BS and BC.

In this way, the q-parameter of a beam entering the $4f$ system, remains the same after its propagation along the whole optical system[3]. In the studied resonator, the presence of the $4f$ system, reducing the beam divergence, increases the number of possible configuration within the stability region.

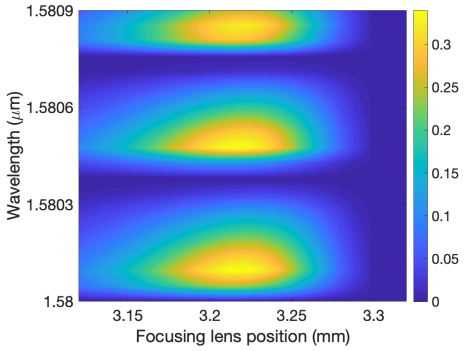

FIGURE 5.10: (c) Power overlap integral between the cavity beam, result of the interference of the beams propagating in the two separate arms, and the SOA mode. The map is obtained for different values of the wavelength and of the focusing lens position, l_2, for a given resonator configuration, $a = 45\,cm \quad b = 15\,cm \quad c = d = 60\,cm \quad x = 24\,cm \quad x + 2y = 4f\,cm$.

Furthermore, a slightly increase was observed also for the excitation efficiency with respect to the values reported in fig. 5.8b.
Figure 5.10 shows an example of power overlap integral between the combined beam and the SOA beam, in a given resonator configuration (the one in fig. 5.7 with the 4f system) where

$$a = 45\,cm \quad b = 15\,cm \quad c = d = 60\,cm \quad x = 24\,cm \quad x + 2y = 4f \quad f = 10\,cm$$

Because of the interference, also the coupling efficiency shows a clear dependence on the wavelength.

[3] Indeed, $M = \begin{bmatrix} 1 & f \\ 0 & 1 \end{bmatrix} \begin{bmatrix} 1 & 0 \\ -1/f & 1 \end{bmatrix} \begin{bmatrix} 1 & 2f \\ 0 & 1 \end{bmatrix} \begin{bmatrix} 1 & 0 \\ -1/f & 1 \end{bmatrix} \begin{bmatrix} 1 & f \\ 0 & 1 \end{bmatrix} = \begin{bmatrix} 1 & 0 \\ 0 & 1 \end{bmatrix}$

We then evaluate the laser output power, as function of the OC reflectivity, for different values of the BS reflectivity, in a given stable configuration, when the injection current is equal to $500mA$. The laser behavior, shown in figure 5.11a, slightly differs from the one found for the previous design, reported in fig. 5.2a. Nevertheless, the features characteristics of the ISA ECL are still observed.

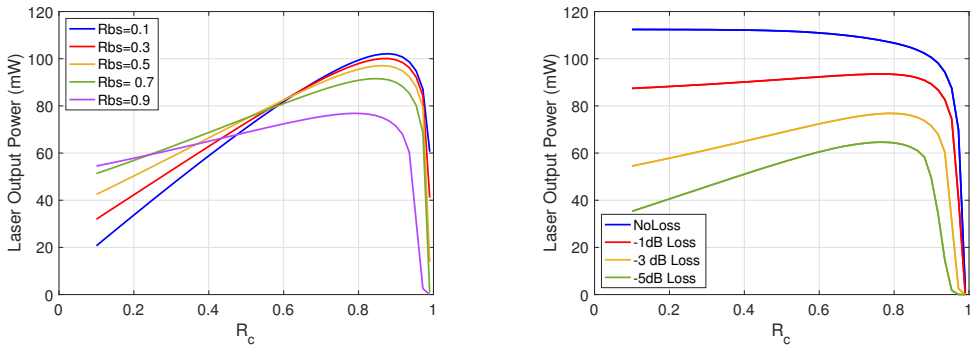

(A) (B)

FIGURE 5.11: (a): ISA ECL output power, as a function of the OC/RC reflectivity, when the cavity losses are equal to $-3bB$. The different curves refer to different values of the initial beam splitter reflectivity. (b): Laser Output Power as a function of the OC/RC reflectivity, when $R_{bs} = 0.9$, for different values of the total cavity losses

.

Finally, the laser power was evaluated for different values of the total laser losses, which include both the cavity losses, and the coupling losses in the gain block. Figure 5.11b shows the obtained result, when $R_{bs} = 0.90$. Depending on the total losses the maximum value of the ISA ECL is reached for different R_c.

5.3.2 Experimental results

The single stage ISA ECL was experimentally tested in one of its stable configuration. More in details, $a = 45cm$, $c = d = 60cm$, $b = 15cm$, $x = 24cm$, $y = 8cm$ and $f = 10cm$. Figure 5.12 shows a photo of the realized device.

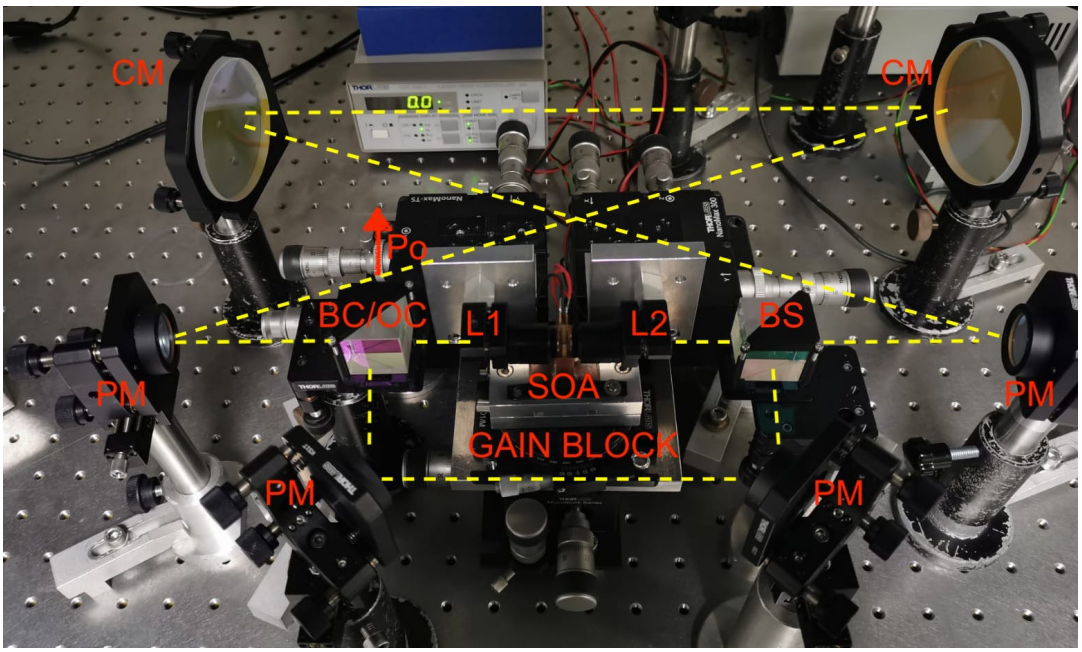

FIGURE 5.12: Photo of the single stage interferometric laser. The picture was taken before the addiction of the 4f imaging system and of the isolator. The different optical component are labeled as usual.

The 4f system was placed and tested using an external laser source. Figure 5.13 shows the measured beam width, along the X direction. The black dashed line in the image indicates the length of the $4f$ optical system. It is clearly verified that the width of a beam entering the 4f system, remains the same also at its exit.

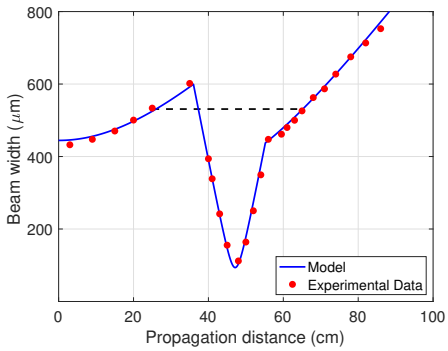

FIGURE 5.13: Experimental verification of the implemented 4f system.

Also in this device, a free space optical isolator is placed at the exit of one of the two SOA facets, to force a single resonant propagating direction. After the alignment procedure, which consists in the optimization of the SOA coupling efficiency, the laser output power was collected for different values of the SOA injection current. The same measurements were repeated, for different values of the OC reflectivity,

$R_c = 0.5, 0.7, 0.9$. Different R_c corresponds to different alignment condition of the laser. Figure 5.14 shows some of the obtained results. To verify the role of the ISA, the same measures were repeated, by blocking the beam propagating in the free arm of this last. The obtained result is shown by the red curves in the figure. The power increase due to the beam interference is clearly visible.

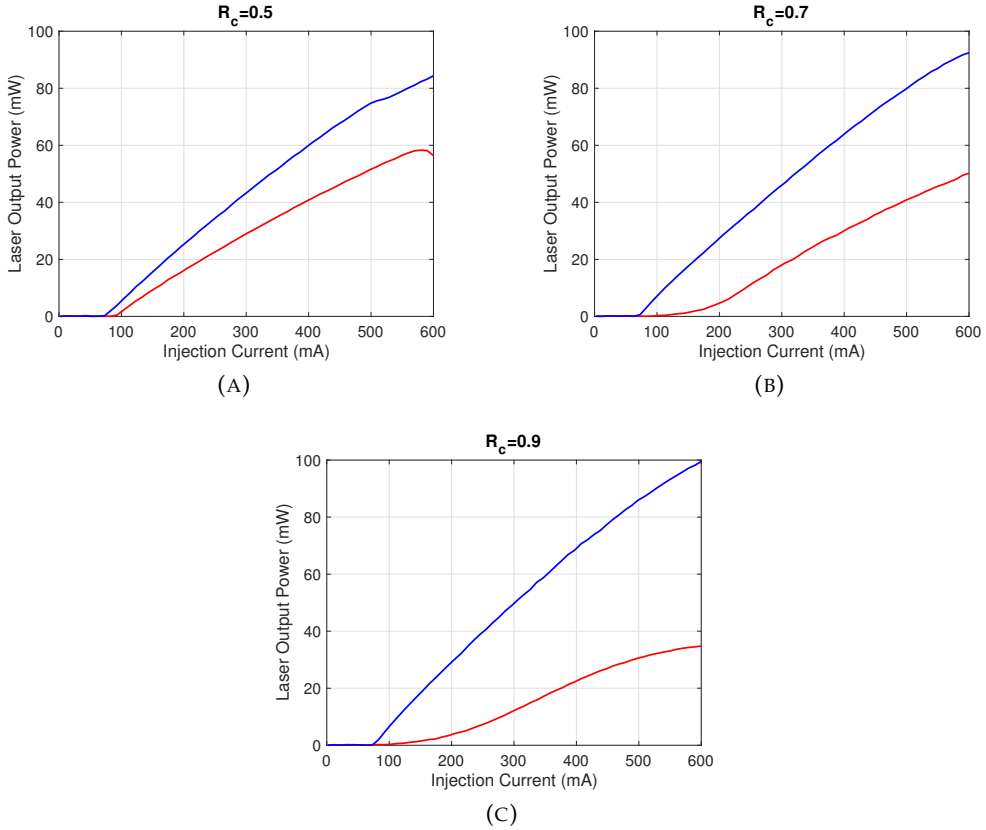

FIGURE 5.14: Experimental Results. Laser output power versus the SOA injection current. The blue curve refers to the interferometric laser, while the red curve is obtained when blocking the free arm of the interferometer. (a): $R_c = 0.5$, $R_{bs} = 0.9$, (b): $R_c = 0.7$, $R_{bs} = 0.9$, (c): $R_c = 0.9$, $R_{bs} = 0.9$

From the experimental results some important consideration can be made. First, it appears the laser output power increases when the BC reflectivity increases. However, the experimental results are not perfectly matched by the theoretical predictions, as shown in fig. 5.15. The simulations were performed assuming the values of losses equal to those measured experimentally.We further suppose a coupling efficiency of the SOA beam of 50%.

We associated the observed discrepancies to different coupling condition experienced both by the internal cavity and external cavity beams. Here we name internal cavity the SOA ECL path, obtained when the free arm of the interferometer is blocked. Higher values of R_c correspond to an increase of the quality factor of the external cavity, and simultaneously to an increase of the internal cavity losses. The higher quality factor of the external cavity leads to an alignment condition, which favors the laser oscillation of this last, rather than the one relative to the internal cavity.

Finally, the results reported in fig. 5.14c shows that the power behavior of the ISA

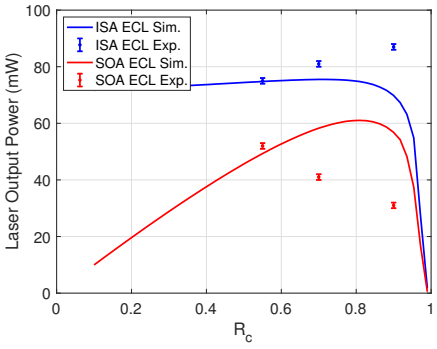

FIGURE 5.15: Comparison between the experimental values of the measured power (points) and the simulation results (solid curve), for the ISA ECL (the blue curve) and the resulting SOA ECL when the interferometer free arm is blocked (red curve).

ECL, resembles the one measured for the standard ECL[4] in the optimum alignment condition. Nevertheless, in spite of the relative high output power no kinks neither other nonlinear features appear. We associated the lack of such detrimental effects to the presence of the free arm of the interferometer. This result confirms one of our initial statement, that the limiting phenomena, associated with high power operations, are almost entirely reduced in the ISA ECL, at no expense of the laser output power.

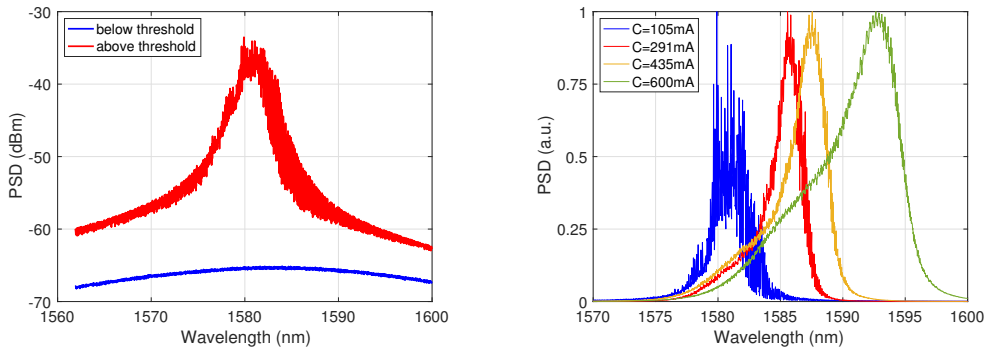

(A) (B)

FIGURE 5.16: Experimental results when $R_c = 0.7$. (a): Laser output spectra just above (red curve) and below (blue curve) the laser threshold current. (b): Emission spectra for several values of the SOA injection current. The curves are normalized according to their maximum values.

Emission spectra of the laser, for different values of the SOA injection current are shown in figure 5.16, when $R_c = 0.7$. The OSA resolution was set equal to $0.05nm$, while the VBM equal to $100Hz$. The emission spectra narrow as soon as the injection current reaches the threshold value. Similarly to the standard ECL, figure 5.16b shows that the emission peak shifts and the emission bandwidth increases, when increasing the SOA injection current. Differently from the standard ECL, here the fringes visibility changes with the injection current, and therefore the laser power. The result is consistent with the theory reported in Chapter 3.

[4]See figure 4.31

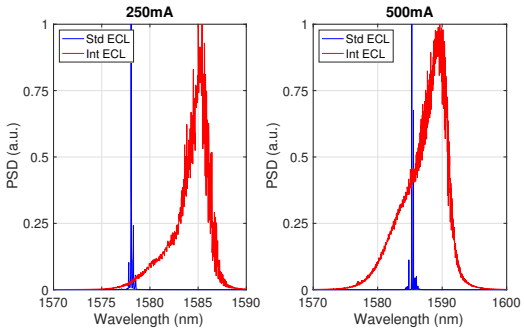

FIGURE 5.17: Comparison between the emission spectra of the ISA ECL when the free interferometer arm is blocked (blue curves) or not (red curves), for two different values of injection current, $I = 250mA$ and $I = 500mA$.

Emission spectra were also measured when the free interferometer arm is blocked. In this case, the laser behaves as a standard ECL. The blue curves in fig. 5.17 shows the results. A comparison with the spectra of the ISA ECL, taken at the same value of injection current, is also shown. We notice that the ISA ECL emission spectra show a higher number of cavity modes, as expected because of both the increase of the cavity length, the process of interference and the reduced losses.

Both the emission wavelength and the emission bandwidth differs in the two situ-

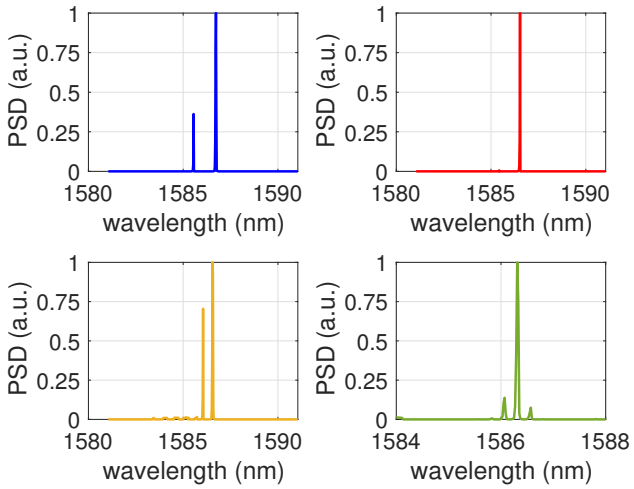

FIGURE 5.18: Emission spectra collected at a $VBM = 100kHz$, for several time instants. The different curves refer to the ISA ECL, when operating at $300mA$.

ations, similarly to what was observed in fig. 5.16b. Again, the explanation can be searched in the joined effects of the reduction of optical losses and increase of circulating power in the ISA ECL.

Finally, the same emission spectra were collected at a higher VBM, equal to $100kHz$. Figure 5.18 shows the result for the intereferometric laser, when an injection current of $300mA$ is applied. The measures were taken at different times, within 1 minute long interval. The contribution of the individual modes is visible. In this way single snapshots of the emission spectra are possible. We noticed few lines that move

within the ISA ECL bandwidth (the red curve in fig. 5.16b). We can therefore, conclude that the collected data, reported in fig. 5.16 are the results of an averaging of the individual oscillations due to the different modes and the different interference conditions.
The beam profile at the laser output was collected through the scanning-slit beam profiler, at a distance of approximately 30cm from the cavity OC. Figure 5.19 shows the results for the two situations in which the beam propagation in the free interferometer arm is blocked or not.

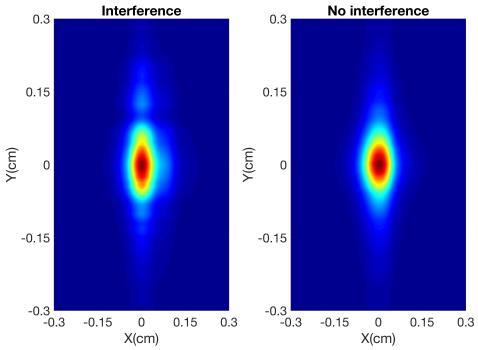

FIGURE 5.19: Laser output beam profile. The measure was taken at a distance of 30cm from the cavity OC.

As expected, the beam profile is almost entirely determined by the SOA emitted beam, and it is slightly affected by the external cavity. The differences can be either caused by the interference between the two spots or to some alignment errors.

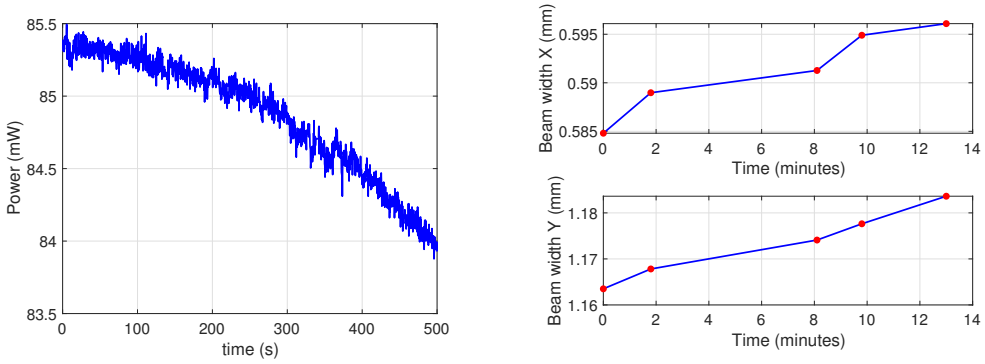

(A) (B)

FIGURE 5.20: (a): Laser output power as a function of time. A variation of 2% is observed in less than 10 minutes. (b):Measured beam width, at different time interval.

Finally, we evaluated the laser stability, by measuring the time dependence of the-laser output. The data are reported in fig. 5.20a. It is observed that progressively the laser output power decreases. The reason was attributed to the lens, whose mechanical supports relax in time. To prove it, the beam profile was collected at different times, with the beam profiler fixed in a certain position. The measured beam width is reported in figure 5.20b. The variations with respects to the initial point are clearly visible. From the simulation, it can be easily shown that even a small variation (of the

order of some tens of μm) can significantly influence the coupling efficiency. A more stable behavior is expected when the lenses are glued on fixed mechanical blocks.

5.4 Double stage interferometric laser

Since the single stage interferometric laser confirms the advantages of the ISA gain block, we moved to test a double stage ISA ECL. Figure 5.21 shows a sketch of the realized device.

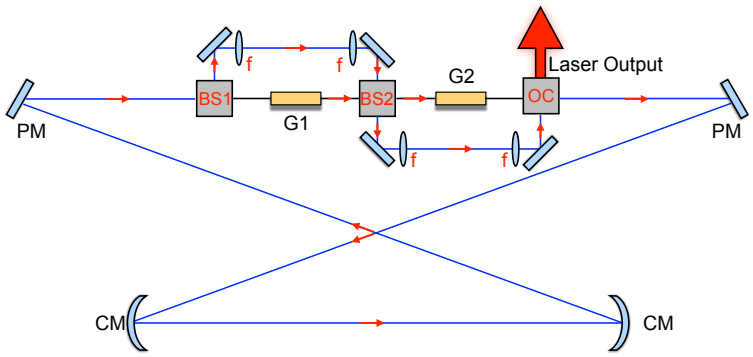

FIGURE 5.21: Scheme of the double stage interferometric laser.

The selected configuration avoids the losses in the BC by circulating the field in the free arms of the interferometer. With this respect, the choice of BS_2 is crucial to determine the saturation behavior of the amplifiers. As a matter of fact, a high value of R_{bs_2} translates into a higher portion of the beam coming from G_1 that is reflected towards the free arm of the second interferometer. At the same time, a large portion of the beam traveling in the free arm of the first interferometer is sent directly to $G2$, with a highly R_{bs_2}. These two facts contrasts with the idea, of reducing the circulating power in each single amplifier gain stage. Therefore, a compromise needs to be found. In any case, this configuration allows combining a sequence of ISA with a limit imposed by the gain saturation law.
With respect to the first configuration we proposed (fig. 5.1 and fig. 1.12), this design has the advantage of no losses at BC while the number of stages is limited and the circulating power in the amplifier is higher. The absence of losses should easy its actual realization.

5.4.1 Modeling

The optimization of the cavity components and distances can be simply reduced to the ones obtained for the single stage laser. This is possible thanks to the implementation of an additional $4f$ imaging system in the second interferometer, as shown in fig. 5.21. The double $4f$ system has two main advantages. It expands the possible resonator configurations, within the external cavity stability region, and maintains equal the value of the coupling efficiency between the cavity field and the two SOAs guided modes. The optimum configuration can be easily found, according to the single-stage interferometric laser modeling procedure. The only additional consideration regards the evaluation of the coupling efficiency between the two SOAs.
The collimating lens of G_1, the focusing lens of G_2 and the distance between the two amplifiers should be chosen to minimize the coupling losses on G_2, for both the beam coming directly from $G1$ and the one propagating into the first free interferometer arm. Figure 5.22 shows the power overlap integrals, for the coupling efficiency

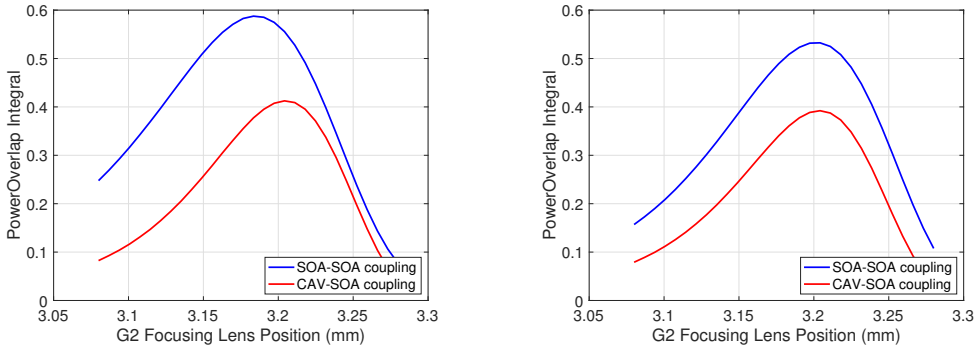

FIGURE 5.22: Power overlap integral of both the SOA-SOA beams, and the SOA-Cavity beam. (a): when $x = 24cm$, (b): when $x = 30cm$.

between the two SOA beams (the blue curves) and for the coupling efficiency between the cavity and the SOA beam (the red curves). The integral are shown for two different values of the interferometer length.
We can see that if the maximum of the power overlap integral is reached at two different positions of the focusing lens (see fig. 5.22a), the interferometer length ($x + 2y$ in fig. 5.7) is not appropriate. On the contrary (see fig. 5.22b), if the length is correct a common value of the lens can be found. This will introduce additional losses and the cavity does not fully exploit the advantages introduced by the interferometers.
The final laser design was chosen, following all the considerations made up to now. Some geometrical constraints, such as the bulky dimension of the lenses, the presence of the mechanical mounts and the angle of the curved mirror, limit the design possibility. These can be mitigated once a custom mechanical form can be fabricated at the end of the validation phase.

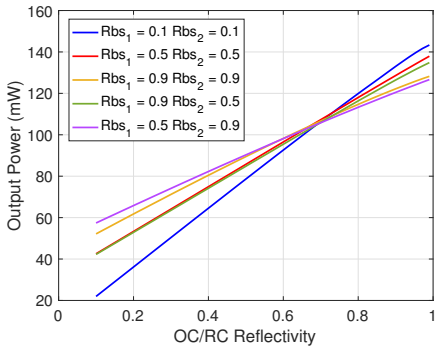

FIGURE 5.23: Double stage ISA ECL, simulation result. Laser output power as a function of the OC/RC reflectivity.

Finally, the laser output power, was evaluated for several values of the reflectivity of the various components in the cavity. Also in this case, the results were obtained by following the field evolution during several cavity round-trips. Figure 5.23 shows the simulated result for different combinations of R_{bs_1} and R_{bs_2}, as a function of the OC reflectivity. The simulations were performed, assuming the losses in both the cavity, α_c and in the interferometers, α_{i1} and α_{i2}, equal to the measured values, respectively, $\alpha_c \approx -2.5dB$, $\alpha_{i1} \approx -4.2dB$ and $\alpha_{i2} \approx -1.3dB$.

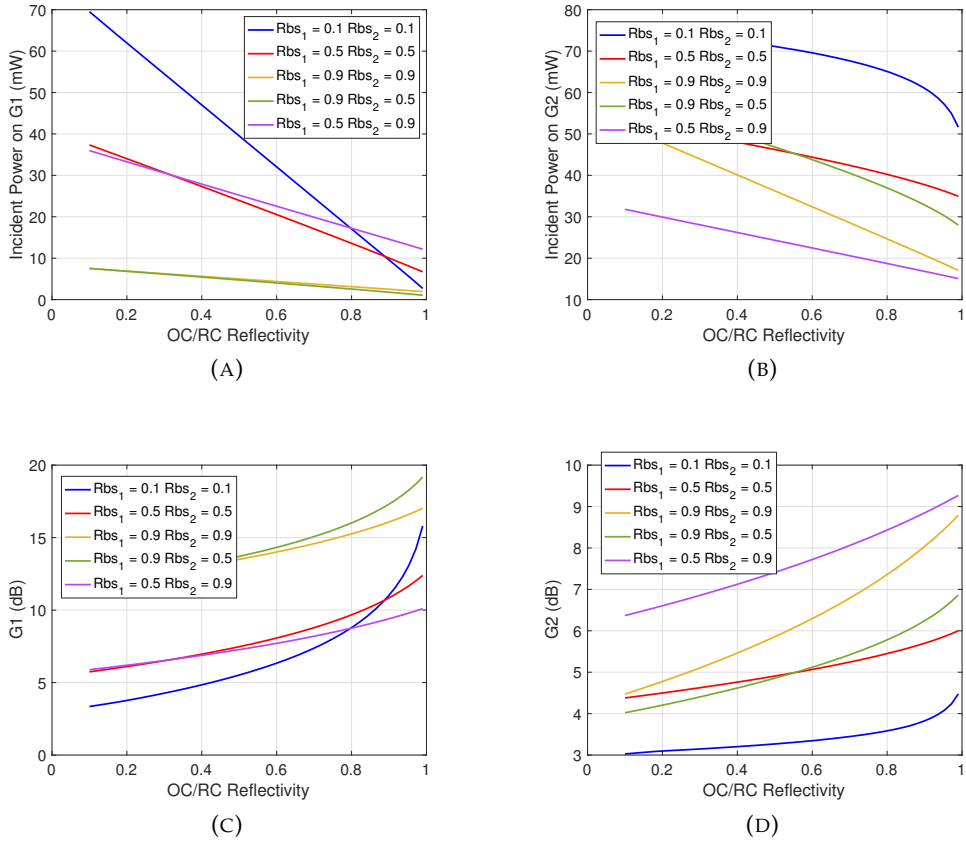

FIGURE 5.24: Double stage ISA ECL, simulation result. (a): Incident Power on G1. (c): Incident power on G2. (d): Saturated Gain of G1. (e): Saturated Gain of G2. The different curves refer to different combination of R_{bs^1} and R_{bs^2}

For a better understanding of the laser behavior, also the incident power on the two amplifiers, and the resulting saturated gain, are reported in fig. 5.24. First, let us notice that for every configuration of the two beam splitter reflectivity, the maximum laser output power is achieved when the OC reflectivity assumes the maximum value. This situation corresponds to the minimum value of the incident power on each gain medium, which in turn corresponds to the maximum value of the saturated gain.
Consistently with the results for the single stage ISA ECL and for the multi-gain laser (showed at the beginning of this chapter), when the number of combined element is small, the maximum laser output power is achieved for low values of the two beam splitters reflectivity. This condition corresponds to the maximum power amplification. Because of the gain saturation law, this behavior is influenced by the total number of SOAs, and changes when this last increases.

5.4.2 Experimental results

To validate the power scaling by sequences of ISA gain blocks, the configuration of major interest is the one with the incident power on the second gain element as low as possible. According to the simulation model, we therefore mounted and tested a double stage ISA ECL with $Rc = 0.9$,$R_{bs_1} = 0.5$ and $R_{bs_2} = 0.9$. The cavity geometry follows the same geometry realized for the single stage laser. The only difference regards the length of the free arms of the two inteferometers. According to the results, reported in fig. 5.22, x was set equal to $27cm$, which is the maximum length that we can use in our set-up. Therefore, we expect slightly different coupling coefficients between the G_2 SOA (see fig. 5.21), and its incident beams. Table 5.1 summarize the chosen cavity configuration.
Finally, optical isolators are used before each SOAs.

a (cm)	b (cm)	c (cm)	d(cm)	x(cm)	y (cm)	f_{4f} (cm)	l_1(cm)	l_2 (cm)
45	15	60	60	27	6.5	10	≈ 0.316	≈ 0.325

TABLE 5.1: Cavity Parameter.

The very high number of optical components in the cavity makes the whole alignment procedure far from trivial. An external laser was used to align the cavity.
The laser output power as a function of the SOAs injection current is reported in figure 5.32a. In this case, the current of the two amplifiers is varied simultaneously of the same quantity. A threshold behavior, sign of the lasing, is observed. The obtained power is larger than the one obtained form the ECL and from the single stage ISA ECL. Furthermore, for the expected value of measured losses, the results are consistent with the simulated values, reported in fig. 5.23 when the SOA current, for both the amplifiers, is set to be equal to $500mA$. The same measure was repeated, by fixing one of the two SOA injection current at a value of $500mA$, while varying the second SOA injection current. Figure 5.32b shows the obtained result.

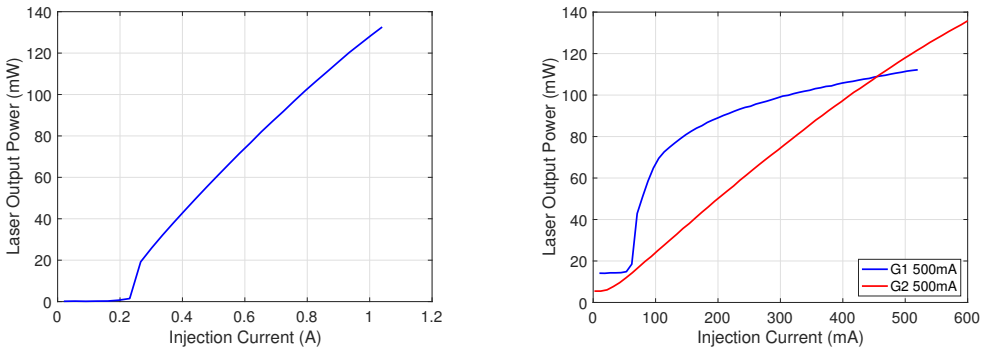

(A) (B)

FIGURE 5.25: Double stage ISA ECL experimental results. (a): Laser output power versus the total injection current when the two SOA are driven by the same current. (b): Laser output power versus the single SOA injection current, while fixing the other at $500mA$. The blue curve refers to the case when the current of the amplifier indicated as G_1 in fig. 5.21, while the red curve shows the results when the G_2 injection current is varied.

Very different behaviors are observed in the two experimental conditions. When the

current in the first ISA block (the blue curve) is varied the laser output power saturates. While when the current driving the second ISA block, G_2, is varied the laser power increases linearly. This difference can be explained in different ways. A first explanation can be associated to a high value of power circulating in the resonant cavity and incident on the amplifiers. It can be either associated to G_1 or to G_2. For example the use of an initial beam splitter with a relative low value of reflectivity, as in our case, can be not sufficient to reduce the input power in the G_1 block. A similar argument holds for G_2 and the second beam splitter. If this is the case, one or both the two amplifiers work in a very highly saturated regime. However, nonlinear features and detrimental effects (kinks) associated with the high power operation should be observed. For this reason, we believe that the observed behavior is mostly related to the particular coupling condition experienced by $G2$. To better understand the situation, we can observe that in the absence of the coupling between the two SOAs, the whole system can be viewed as composed by two separated laser cavity. These are schematically indicated in fig. 5.26 by the blue and the red lines. The blue line in fig. 5.26 refers to the G_1 external cavity, while the red line indicates the cavity containing G_2. At the OC, the contributions add with a relative weights which depend on the value of the OC reflectiviy. For our design, $R_{OC} = 0.9$ and thus the major contribution is imparted by the cavity containing G_2.

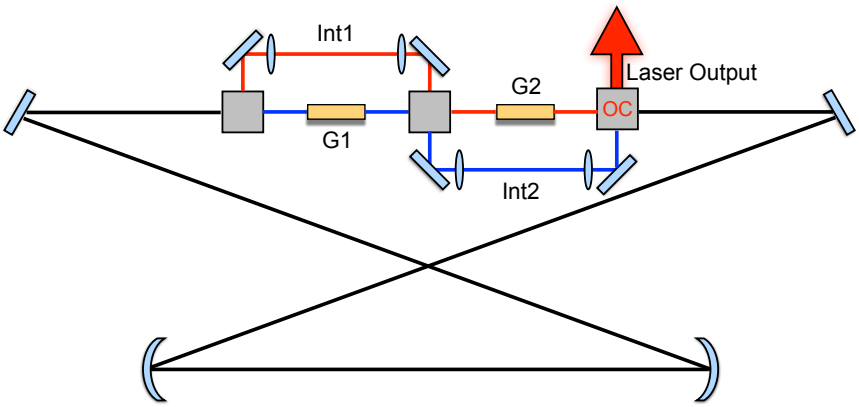

FIGURE 5.26: Scheme of the operation mechanism of the laser device. The blue line shows the laser cavity for G_1, while the red curve refers to the G_2 cavity. The black line is common for both the two resonant cavities.

If we consider, the coupling between the SOA, G_2 will amplify both the contribution coming from the external cavity, and the contribution coming directly from G_1. If G_2 is not correctly aligned within its own cavity (the red line in fig. 5.26), its only contribution is the amplification of the signal coming from G_1. This also means that the measured output power as a function of the injection current, will mostly resemble the SOA ASE. Furthermore, because the output power is mainly due to the signal amplified by G_2, the contribution of the free arm of the second interferometer (blue line in fig. 5.26) is completely masked.
To better understand the role of the individual amplifiers, we turned off one of the two SOA. Figure 5.27 shows the measured results.
The blue curve represents the situation in which G_1 is turned off, while the red curve refers to G_2 turned off. When G_1 is off, because of the various reflectivities of the optical components, the double stage ISA ECL is analogous to a standard ECL (tested in Chapter 4). If the G_2 cavity is correctly aligned, we expect values of output power

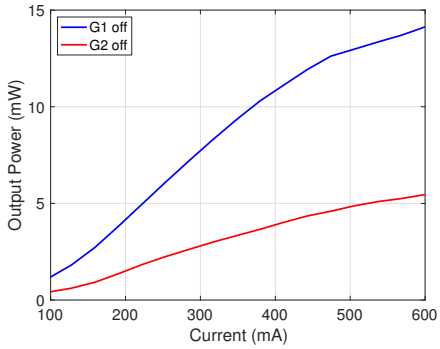

FIGURE 5.27: Laser output power when one of the two SOA is turned off. The blue curve shows the situation G_1 off, while the red one when G_2 is off.

compatible with the one measured for the ECL and reported in fig. 4.31. The lower measured power (see the blue line in fig. 5.27), which are also closed to the SOA ASE power (see fig. 2.14a) suggests a poor coupling condition between G_2 and its own cavity (the red line in fig. 5.26). The same considerations are not valid for the opposite situation G_2. Because of the higher losses, due to the different reflectivities, in the G_1 cavity low value of output power are expected (red curve in fig. 5.27). Other information can come from the study of the laser when the free interferometers arms are blocked. Figure 5.28 shows some of the measured results.

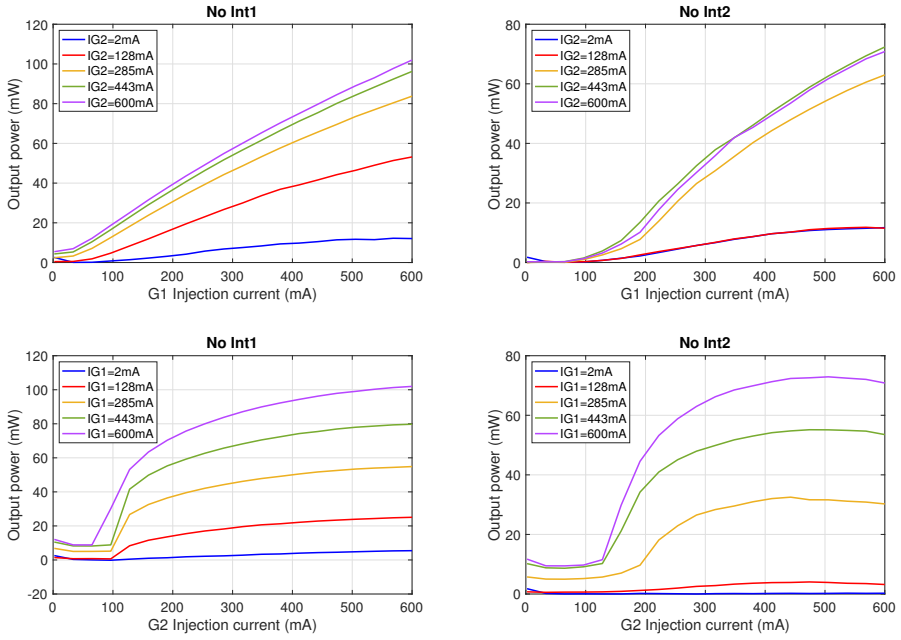

FIGURE 5.28: Laser output power as a function of the injected current. The left panels refer to the cavity where the free arm of the interferometer is block, while the right panels describe the situation when the free arm of the second interferometer is blocked. The upper panels shows the output power versus the G_1 injection current for few G_2 current values, while the lower panels the viceversa situation.

The left panels shows the measures obtained when the free arm of the first interferometer is blocked, while the right panels show the situation when the free arm of the second interferometer is blocked. The measures, reported in the upper insets of the image, were performed by varying the current on G_1, while fixing the working value of G_2. On the other hand, the lower insets describe the opposite situation. The top panels show the laser output when G_1 driving current is varied for different values of G_2 current, while the bottom panels when the G_2 driving current is varied for a few G_1 current.
The first consideration that can be made regards the values of the measured power. The major contribution to the total laser output is coming from the second interferometer arm. This is equivalent to say that the cavity path which involves G_1, shows higher performances than the lasing cavity with G_2 only.

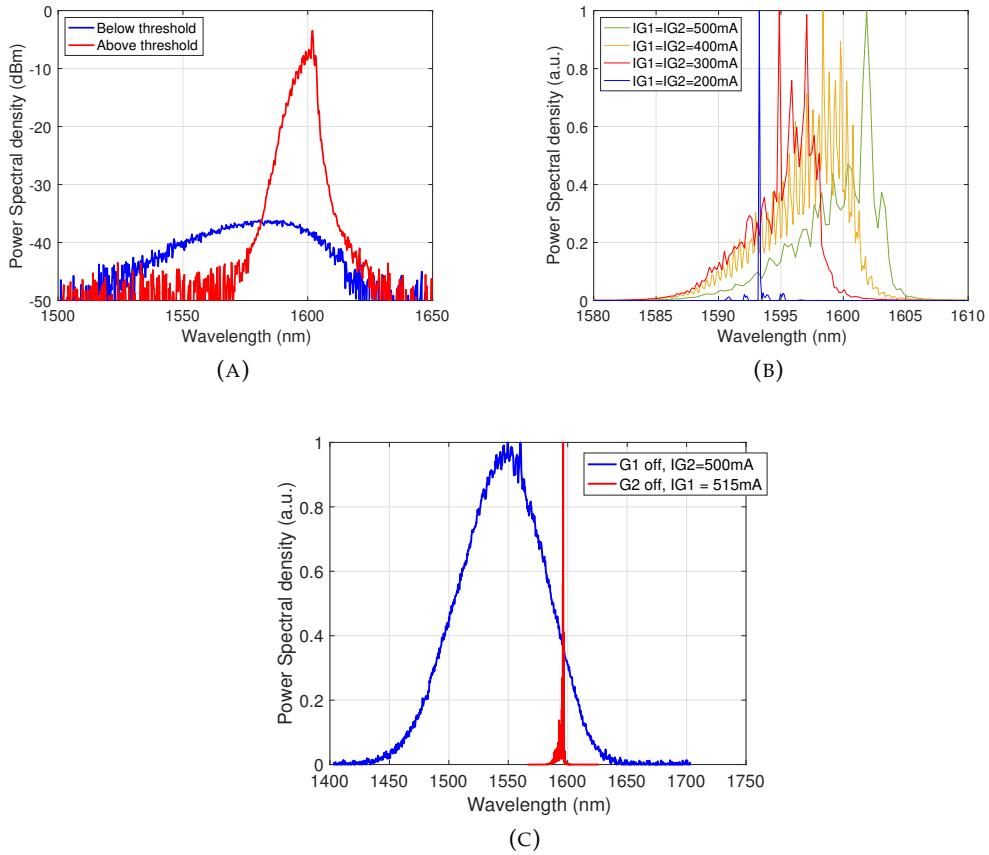

FIGURE 5.29: Experimental results. (a): Laser output spectra just above (red curve) and below (blue curve) the laser threshold condition. (b): Emission spectra for several values of the two SOAs injection current. The curves are normalized to their maximum values. (c): Emission spectra collected when turning off one of the two amplifiers. The blue curve is obtained when G_1 is off, while the red curve describes the opposite case.

The optima working conditions of the cavity involves not only the alignment of each SOA with its own cavity, but also the mutual coupling between the two amplifiers. This is surely achieved through R_{bs_2}, which couples the amplified emission from G_1 to the entrance facet of G_2, but also via the common external cavity (the black line in

fig. 5.26). This last, if correctly aligned, couples the amplified power from G_2 to the entrance facet of G_1. The contribution coming from the mutual coupling between G_1 and G_2 in the laser output power, remains also when the free interferometers are blocked. Thus, when the first interferometer free arm is blocked in the output power appears the contribution due to the G_1 cavity and to the coupling between G_1 and G_2 through R_{bs_2} and the external cavity. On the contrary, when the second interferometer free arm is blocked, the output power shows, besides the contribution due to the mutual coupling of G_1 and G_2, the G_2 cavity. From the right upper panel of fig. 5.28 we observe that G_1 shows a lasing behavior even when its cavity is blocked. This condition suggests a good coupling between the signal emitted from G_2 and the first amplifier, through the external cavity. However, from the right lower panel, we observe a behavior which resembles the one described for the ASE in Chapter 2, while the typical behavior of a laser device is missing. This means that the alignment procedure to maximize the laser output power, favors the coupling between the two SOAs (via R_{bs_2}), rather than the oscillation of the G_2 external cavity, which is absent. The final result will is the realization a laser cavity, for G_1, whose power is enhanced by the presence of G_2, which simply acts as an amplifier.

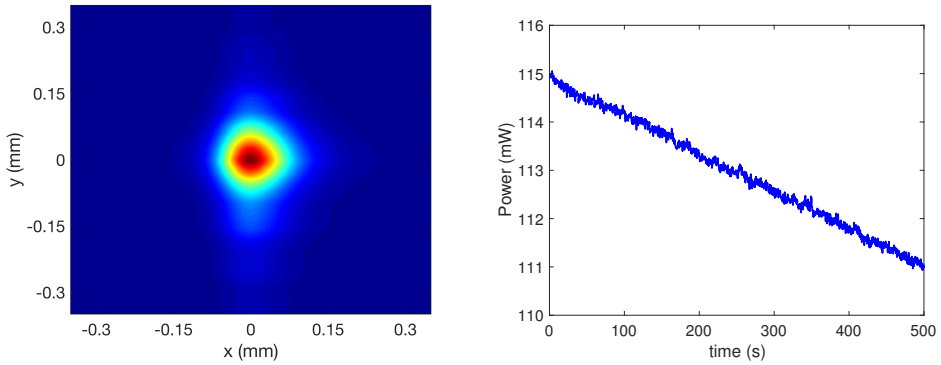

(A) (B)

FIGURE 5.30: Experimental results. (a): Laser beam profiler. The measure was taken at a distance of 30cm from the cavity OC. (b):Laser output power, as a function of time, when the two amplifiers operates at 500mA

The emission spectra at the output of the laser cavity were collected with an OSA, and are shown in fig. 5.29a. A narrowing of the emission spectra is observed, as soon as the current value reaches the threshold value. Figure 5.29b shows the spectra collected for different values of the current of the two SOAs. The emission peak shifts, consistently with what observed previously. The emission bandwidth shows clear interference fringes, sign of the presence of the interference process.
Interestingly, when the driving current is switched off in one or in the other SOA, the laser spectra are very different. Figure 5.29b shows the results. While G_1 still shows a lasing emission, as indicated by the red curve, also in absence of G_2, the collected spectra of this last shows only the amplifier ASE contribution, the blue curve in the image. This ultimately confirms, the considerations made above regarding the laser behavior.
The laser output spatial profile of the laser was collected. As shown in fig. 5.30a, the major contribution to the beam profile is coming from by the G_2 beam profile,

influenced by the position of the its collimating lens, and it is not affected by the interference of this last with the beam incident on the other entrance of BC. This means that the resulting beam quality is only determined by the SOA characteristics.
Finally, also the laser stability was evaluated. The results are reported in fig. 5.30b. Because of the higher number of optical components, mount and movement systems, the power stability shows worse performances with respect to the single stage interferometric laser. Also in this case, a more stable device is expected when each optical components is fixed in a single mechanical board.

5.4.3 A further improvement

To further improve the laser, a better alignment condition needs to be reached, in order to obtain the lasing operation for both the amplifiers. Moreover, a further reduction of the power incident on the gain medium needs to be obtained. We expect that this power reduction translates into a higher laser output power.
Therefore, we modified the laser cavity by using the polarization dependence of the gain coefficient of the SOAs. The newly designed laser cavity is shown in fig. 5.31

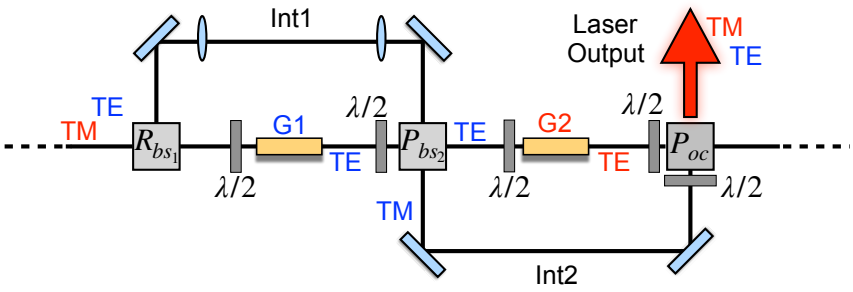

FIGURE 5.31: Scheme of the operation mechanism of the device, at the beginning of the laser oscillation. The blue labels refer to G_1, while the red ones indicate the G_2 polarization state.

The beam splitter between the two amplifiers, is replaced by a polarized beam splitter, P_{bs_2}. A $\lambda/2$ wave-plate is placed after G_1 and before P_{bs_2}, to set the fraction of the beam, emitted from G_1, that will be amplified by G_2. Therefore, the beam traveling in the second interferometer, has an orthogonal polarization state with respect to the one amplified by G_2. The cavity OC is also replaced with a polarized beam splitter, P_{OC}. Here, the TE polarized field amplified by G_2 overlaps with the TM polarized field propagating in the second interferometer. Two wave-plates placed at entrance of P_{OC} set the beam portions, that combine. The resulting beam is either sent out or made recirculating in the cavity. Therefore, within the resonator, the propagating field contains the two polarization components. The use of two additional wave-plates, placed in front of the two amplifiers, maximize the amplified power. Furthermore, depending on the wave-plate angles, the whole device can be aligned in two different operating conditions. In the first one, each amplifier is independent and the final device can be thought as two separated cavities, coupled together, at P_{OC}. The second configuration instead involves the direct coupling between the two beams. The two working conditions can be easily interchanged by rotating the various wave-plates. The full potential of the scheme can be reached if also R_{bs_1} is replaced with a polarizer beam splitter, to fully amplified the signal incident on G_1 and G_2.
In order to highlight and test the different behaviors, we tested the laser cavity, when

the two SOAs are not directly coupled.
The laser output power was first collected by varying in the same way the two SOAs injection current. The obtained result is reported in fig. 5.32a.

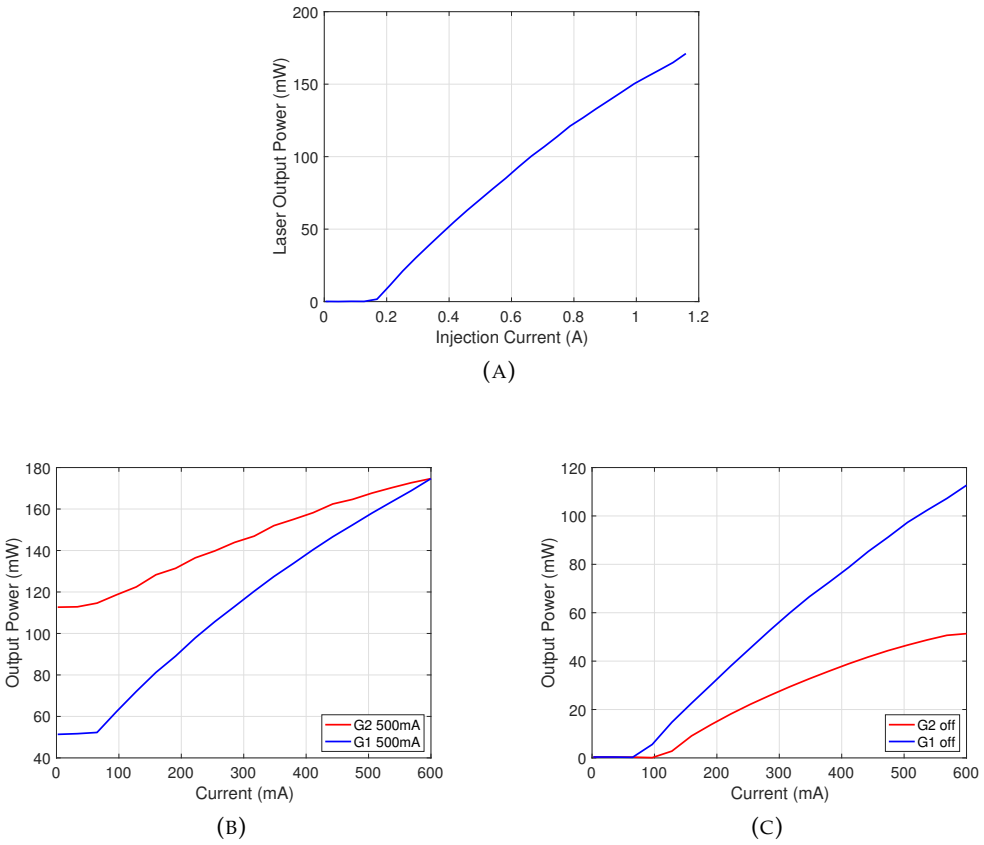

FIGURE 5.32: Experimental result for the second version of the double stage interferometric laser. (a): Laser output power when both the two SOA injection currents are simultaneously varied. (b): Laser output power, when only a single SOA injection current is varied, while fixing the other at $500mA$. The blue curve shows the result when varying the current of the amplifier indicated as G_1, in fig. 5.21, while the red curve shows the laser behavior when only the G_2 is varied.

The obtained behavior demonstrates the lasing operation. The measured output power is higher than the one obtained for the previous laser cavity, as expected because of the lower power circulating in the two amplifiers. Also in this case, the result is consistent with the simulated one. Figure 5.32b reports the measure, when the injection current of one amplifier is varied, while the one of the other is set at $500mA$. The obtained result differs from those found for the previous laser cavity, in the same experimental condition. As expected, here, the two amplifiers lase separately. The result is further confirmed by fig. 5.32c, which shows the measured power, when one of the two SOAs is turned off. The lasing operation is still maintained, for both the amplifiers. The different laser output powers are due to the different cavity losses experienced by the two individual cavity, including those due to the different beam splitters.
Also in this case, the measurements were repeated excluding the contribution of the interferometers. Figure 5.33 shows the obtained results.

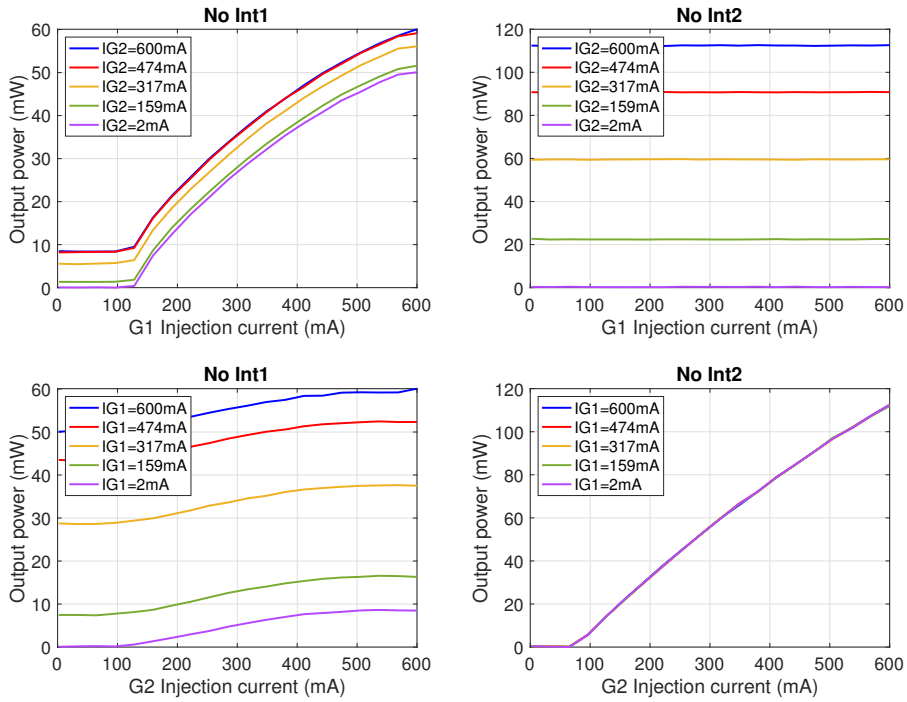

FIGURE 5.33: Laser output power as a function of the injected current. The left panels refer to the cavity where the free arm of the interferometer is block, while the right panels describe the situation when the free arm of the second interferometer is blocked. The upper panels shows the output power versus the G_1 injection current for few G_2 current values, while the lower panels the viceversa situation.

These data confirm the individual laser behavior for the two resonant system containing each amplifier. When the free arm of the first interferometer is blocked (left panels), in absence of the direct coupling between the two SOAs, we expect to see the lasing behavior of G_1 and the ASE emission of G_2, which is what we have observed. On the contrary, when the second interferometer free arm is blocked, only the contribution of G_2 is visibile. The experimental results, the right panels in fig. 5.33 show the expected behavior.
The emission spectra collected at the laser output, are shown in figure 5.34.
The spectrum narrows when the threshold current is reached. Differently, from the previous cavity this value is reached for a lower value of the injection current. Figure 5.34b shows the emission spectra for different values of the SOA injection current. Also in this situation, the behavior resembles the one obtained for the previous devices. Finally, figure 5.34c shows the behavior when one of the two amplifier is turned off. The result is a further confirmation of the achievement of the lasing condition for both the two amplifiers.
The laser beam profile is collected, at a distance of $40cm$ from the cavity OC. As shown in fig. 5.35, differently from the previous case, here, the measured beam profile of the laser device differs from the one of the beam emitted from G_2.
The reason is probably associated to the use of the polarizer beam splitter for the OC. Indeed, in the previous device because of the OC reflectivity, the major contribution in the laser output was coming from the beam emitted from G_2. Here, the wave plates, placed in front of the OC, are rotated until the maximum value of the laser

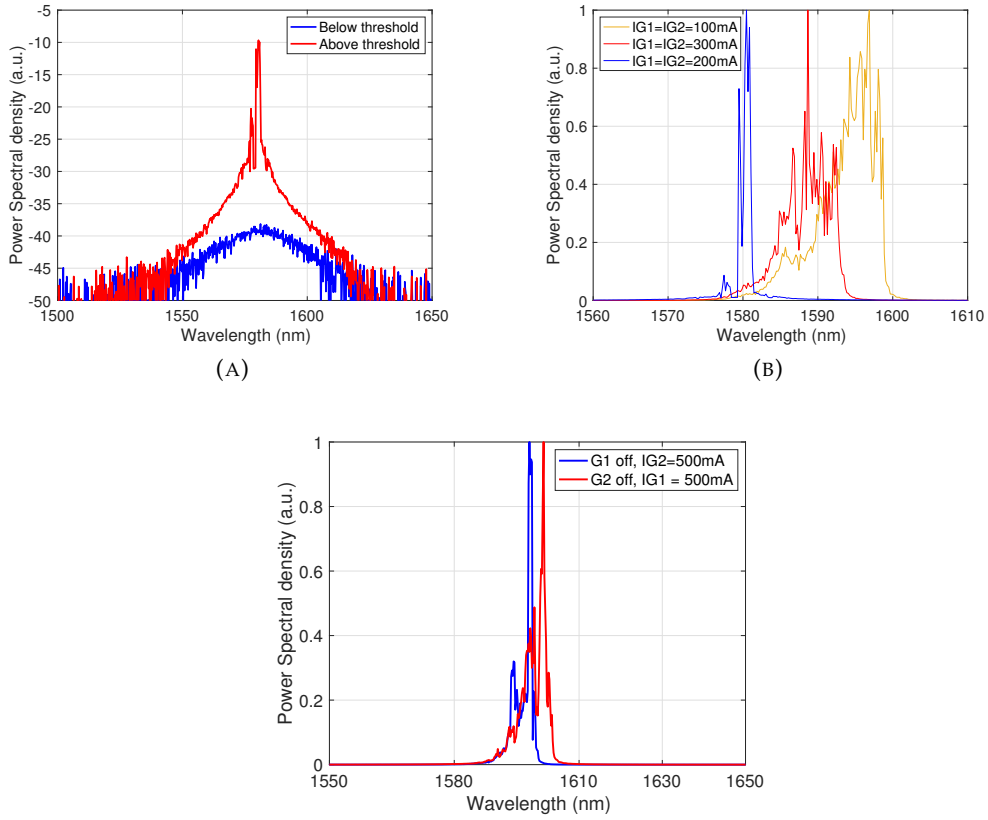

(A) (B)

(C)

FIGURE 5.34: Experimental results. (a): Collected spectra just above (red curve) and below (blue curve) the laser threshold current. (b): Emission spectra for several values of the two SOAs injection current. The curves are normalized according to their maximum values. (c): Emission spectra collected when turning off one of the two amplifiers. The blue curve is obtained when G_1 is absent, while the red curve describes the opposite case.

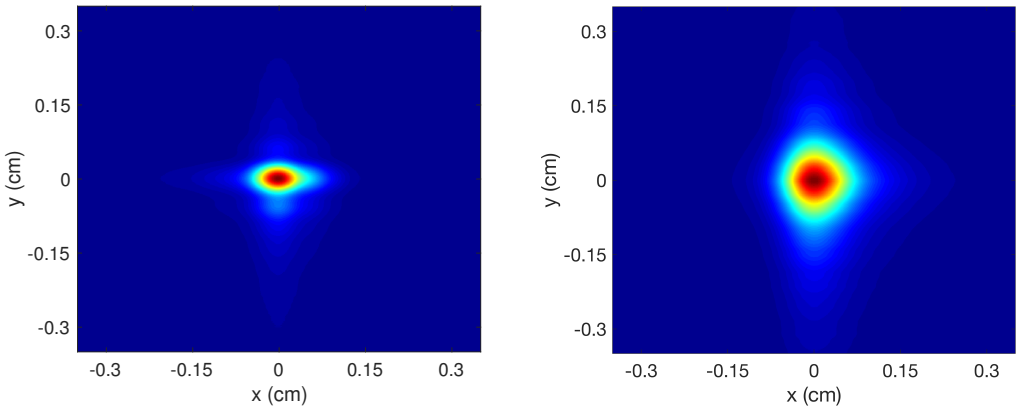

(A) (B)

FIGURE 5.35: (a): Laser Beam Profile. (b): SOA 2 beam profile.

output power is reached. Therefore, the optimum configuration does not necessarily corresponds to the same value of R_c, used in the previous design. The resulting

beam profile is affected by the different contributions of the two different beams, combined at the cavity OC.
Finally figure 5.36 shows a photo of the implemented laser cavity.

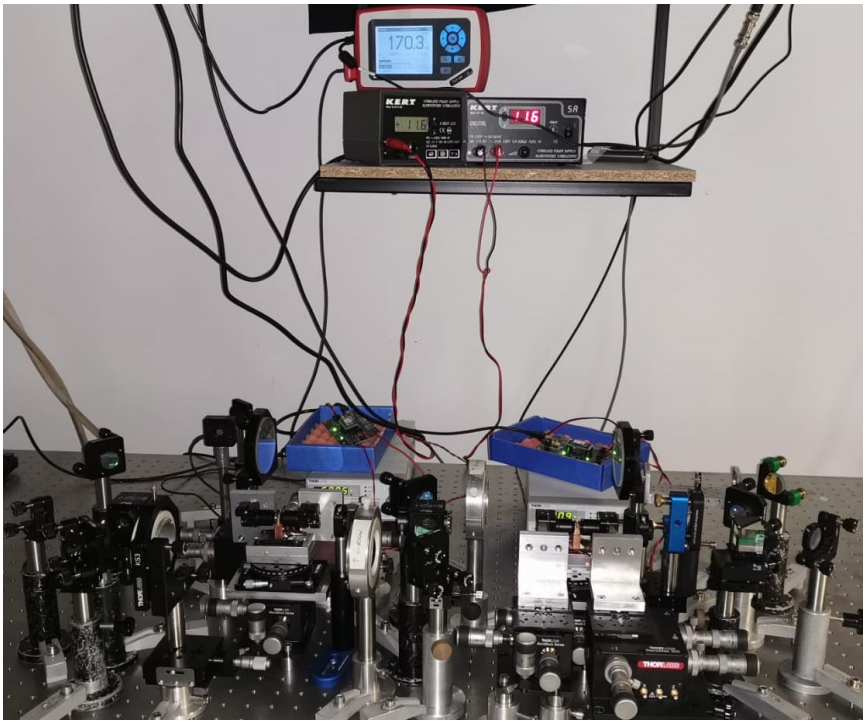

FIGURE 5.36: Photo of the realized laser device.

The laser device should also have been tested in the second working condition, when the two SOAs couple directly among each other. However, because of the restriction due to COVID-19, the access to the laboratory was not allowed and the measures could not have been taken.
This laser can offers the possibility to increase of the number of combined emitters, using the polarization dependence of the SOA gain. Figure 5.37 shows the combining scheme when 4 SOAs realize the sequence.
Different amplification condition are reached, depending on the rotation angle of

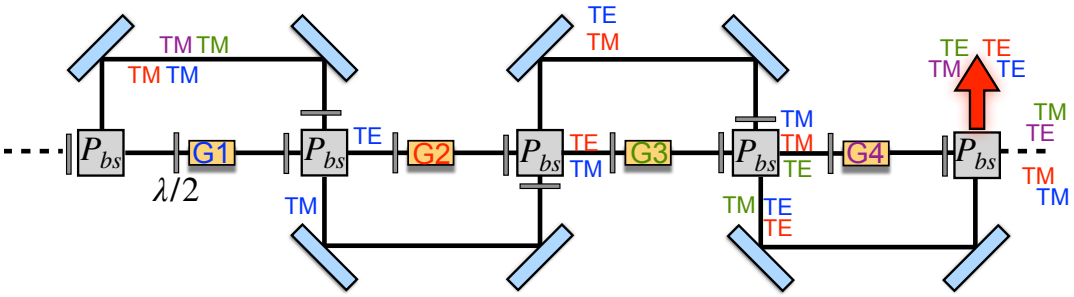

FIGURE 5.37: Diagram of the polarization state in the ISA sequence.
The different colors refer to the different gain media.

the wave-plates. Eventually, some additional losses are introduced. Because of the different polarization, a fraction of the propagating beam will not undergo amplification. With respect of the previous laser cavity design the number of combined

emitters increases.
To conclude this chapter, table 5.2 summarize the obtained experimental and simulated results, when the SOAs injection current is equal to $500mA$. The values of loss used in the simulation correspond to the actual measured values, $\alpha_{cav} = -0.7dB$, $\alpha_{int1} = -4.2dB$ and $\alpha_{int2} = -1.3dB$. We consider a $\alpha_c = -3dB$ coupling loss in both the SOAs. The table also shows the expected results for the design presented in fig. 1.12, within Chapter 1 , when $N = 2$ and each optical component is optimized.

Design	Simulated Power[5]	Measured Power	Loss
Figure 5.21	$133\,mW$	$(128.6 \pm 0.5)mW$	Measured
Figure 5.31	$172\,mW$	$(150.5 \pm 0.5)mW$	Measured
Figure 1.12	$140\,mW$	–	Measured
Figure 1.12	$227\,mW$	–	$0dB$

TABLE 5.2: Summary of the obtained results. Both the simulated and the experimental values are reported, for the different multi-ISA ECL configurations.

[5]When the two SOAs operate at $500mA$.

Chapter 6

Conclusion

This thesis presented a novel cavity design to increase the output power of semiconductor laser in a scalable way. I have validated the new solution for power scaling of diode laser and showed that is comparable with the already exiting techniques.
In Chapter 3 I presented the fundamental element of the idea, the ISA. The main advantages of the ISA, here proposed, are related to the reduction of the power incident on the SOA. This last is achieved by placing the SOA in only one arm of an interferometer. In addiction to the reduction of nonlinear phenomena, associated with high power operation, the proposed strategy allows the realization of a sequence of ISA gain blocks. Differently from a SOAs sequence, which offers some advantages only when very low power input signal needs to be amplified, here the amplification is reached also for high input power. This is due to the difference in the saturation behavior of the ISA effective gain, with respect to the SOA gain. While the SOA sequence output power is limited, the maximum power that can be obtained at the output of an ISA sequence, depends linearly on the number of ISAs, as shown in fig. 3.6. Table 6.1 compares the two sequences and summarizes the main differences.
I also numerically proved the robustness of the novel gain block when working under non optimal conditions. The model was also experimentally verified for a single stage ISA. The very good agreement between the obtained results and the simulation, as presented in fig. 3.16, validates the model and substantiated the proposed gain block.
Up to our knowledge, a device analogous to the one here proposed is absent. A similar scheme was presented in [91]. The fundamental difference with our solution is the presence of SOAs in the two interferometer arms. The result is a doubling of the amplified power, but no advantages with respect to the SOA saturation behavior

Amplifier Sequence	
SOA Sequence	ISA Sequence
Advantages	
• High G_0	• High P_s
• Low power amplification	• High power amplification
	• Linear Increase of P_{out} with N
	• Reduced high power detrimental effects
Disadvantages	
• Saturated P_{out}	• High number of optical components
• High Power detrimental effects	

TABLE 6.1: Comparison between the two amplifier sequences.

appear. Therefore, a further power scaling is not achievable.
The proposed ISA sequence can be used to make a laser when placed within a resonant optical cavity, as presented in Chapter 5. According to my theoretical model, I was able to prove the potential of the proposed laser system. I compared it with other commonly used solutions, based on incoherent beam combining, as shown in fig. 5.3. Our device shows a power scaling capability comparable with respect to the existing architectures. The reason is attributed to the advantages due to the realization of a unique laser source, within which the combining occurs.
The advantages introduced by the use of a common unique resonator, in the proposed system, are related to total cavity losses. Indeed let us suppose to compare a double-stage interferometric laser with an IBC between 2 ECLs. The steady-state working condition of the ECL is reached when the saturated gain equals the total laser losses. These last are mainly due to three contribution. A first one is related to the coupling losses between the gain active medium and the optical beam. The second contribution arise from the reflectivity of the cavity OC, while the last contribution represents the losses experienced by the beam when propagating into the optical cavity. Let us initially consider the ideal case in which the cavity losses are only those imparted by the cavity OC. Furthermore, let us suppose to have a 100% combining efficiency in the two systems. As reported in table 6.2, the output power, resulting from the combining, is equal in both the combining scheme. This represent a first proof of the potential of the proposed solution.
Let us now examine the presence of additional losses in the laser resonator. Let us assume that the resonator design is the same for both the ECL and the interferometric laser. If the design is properly realized, as presented in Chapter 5, the coupling losses, in the interferometric laser are the same for each gain stage, which in turn are equal to the coupling losses experienced by the ECL. On the contrary, the cavity losses are different for the two combining schemes. Each individual ECL experiences a certain intra-cavity loss, while the interferometric laser will experience the same cavity loss, independently of the number of combining elements. This is due to the use of the common resonator. Therefore, the steady-state working condition of the proposed system differs from the one obtained in the ECL and depends on the balance between the ISA sequence effective gain and the total losses.
It was found that, while for a low number of combined element the extracted power in our solution is less than the one achievable with an IBC, when the number of combined element increases, the use of a unique laser resonator avoids the addition of the intra-cavity propagation losses. The result is an increase of the extracted power with respect to the IBC power. The reason is associated to the combined action of the ISA sequence effective gain and the total cavity losses. Table 6.2 summarized the obtained results.
Of course, in the reality, the achievement of 100% of combining efficiency in the proposed system is a more difficult task rather than in a simpler IBC scheme. Furthermore, the increase of the optical components in the system negatively influences the alignment, causing the increase of the intra-cavity losses. The choice of the system design became crucial for the achievement of a good power scaling and need to be carefully studied. Nevertheless, I further proved the robustness of the studied architecture when the system is far from the ideal working condition, as shown in fig. 5.6b.
Therefore, the results obtained by the simulation proved that the proposed solution can offer an alternative, which is different but comparable with the state-of-the-art solution already present in the market. This finding was the goal of this work.
The simulations were experimentally validated in different configurations. By the

Power Scaling Comparison

OUR SOLUTION			IBC		
N	P @ $l = 0dB$	P @ $l = 3dB$	N	P @ $l = 0dB$	P @ $l = -3dB$
1	113 mW	79 mW	1	113mW	104mW
2	227 mW	177 mW	2	227mW	208mW
30	3.4 W	3.29 W	30	3.4W	3.12 W
100	11.37 W	11.2 W	100	11.37W	10.4 W

TABLE 6.2: Comparison between the laser output power achieved with our combining scheme and with incoherent combining technique, for two different values of cavity losses.

comparison between the two tested devices, schematically represented in figs. 5.21, 5.31, I proved that a higher output power is reached, for lower incident power on the SOA. This concept is the key aspect of the proposed power scaling architecture. The realized device is certainty far from being ready to an industrial implementation, and further work needs to be performed. The first improvement regards the high numbers of optical components, which negatively impact the total cavity losses, because of the increase in the device complexity. To overcome this problem the strategy is to move to an integrated platform. Both the choice of the platform and the chip design need to be decided. Because of the device complexity, a whole project needs to be devoted for the achievement of this task. Nevertheless, the semiconductor technology is ready for the full integration. SOA placed in the integrated version of a free-space interferometer are already commonly implemented in photonics chip [94]. The use of waveguides relaxes the constraints imposed by the resonator design in free space configuration, and increases the efficiency when coupling the field with the SOA. Moreover, the implementation of active control systems is easier in the integrated platform. Finally, the limitation on the number of combined SOA, outlined by the results in fig. 5.4, can be overcome when using our device into a modular scheme where different types of combining techniques are employed.
The proposed novel power scaling architecture was protected by filling a patent. The next step is to transfer the concept to an industrially manufactured device.

Publications & Patent

- M. Mancinelli, A. Trenti, **S. Piccione**, G. Fontana, J. S. Dam, P. Tidemand-Lichtenberg, C. Pedersen, L. Pavesi (2017). *Mid-infrared coincidence measurements on twin photons at room temperature*. Nature communications 8 (1), 1-8

- S Piccione, M Mancinelli, A Trenti, G Fontana, J Dam, Peter Tidemand-Lichtenberg, C Pedersen, L Pavesi (2018) *Mid-infrared coincidence measurements based on intracavity frequency conversion*. Proceedings Volume 10516, Nonlinear Frequency Generation and Conversion: Materials and Devices XVII; 105161P (2018) Event: SPIE LASE, 2018, San Francisco, California, United States

- S. Signorini, S. Piccione, M. Ghulinyan, G. Pucker, L. Pavesi (2018). *Are on-chip heralded single photon sources possible by intermodal four wave mixing in silicon waveguides?*. Quantum Photonic Devices 10733

- S. Signorini, S. Piccione, G. Fontana, L. Pavesi, M. Ghulinyan, G. Pucker. (2019) *Towards MIR heralded photons via intermodal four wave mixing in silicon waveguides*. Quantum Information and Measurement, T5A. 11

- S.Piccione, L.Pavesi (2020) *Design of an external cavity semiconductor laser for intra-cavity beam combining*.Proceedings Volume 11266, Laser Resonators, Microresonators, and Beam Control XXII; 1126615 (2020) Event: SPIE LASE, 2020, San Francisco, California, United States.

- S.Piccione, S.Biasi, L.Pavesi, C.Raffaldi. Submitted Patent (2020) *Dispositivo Laser a Guadagno Interferometrico*.

Conferences

- SPIE Photonics West, San Francisco (27/01-1/02/2018): P*oster Presentation*
- Fotonica 2018, Lecce (23-25/05/2018): *Oral Presentation*
- SPIE Photonics West, San Francisco (1-6/02/2020): *Oral Presentation*
- SPIE Photonics Europe, Digital Forum (6-10/04/2020): *Oral Presentation*

Appendix A

Derivation of the SOA small signal gain coefficient

The material system shows gain when the stimulated emission transition rate overcomes the absorption one. This condition is known as Population Inversion and in a semiconductor occurs when

$$E_{fc} - E_{fv} > E \tag{A.1}$$

where $E = h\nu$ is the photon energy of the incoming light, while f_c and f_v the Fermi distribution function of respectively the conduction and valence band. The process is characterized by the net stimulated emission rate. In case of a monochromatic radiation field of frequency ν_0 and intensity I_0, it is given by [119]

$$R_{st} = I_0 \int \frac{1}{\tau_r} \frac{c^2}{8\pi n^2 \nu_0^2 h\nu_0} g(\nu)\rho(\nu)\left[f_c(\nu) - f_v(\nu)\right] d\nu \tag{A.2}$$

where

c	Light speed in vacuum
τ_r	Radiative carrier recombination lifetime
n	Refractive index of the active region
h	Planck constant
$\rho(\nu)$	Optical joint density of states
$g(\nu)$	Lorentzian lineshape function

The light intensity gained during its propagation within the active medium can be obtained by solving the following differential equation

$$\frac{dI_0}{dz} = R_{st} h\nu \tag{A.3}$$

whose solution is of the form $I_0(z) = I_0(0)e^{\gamma z}$.
After some manipulation, it can be easily shown that the gain coefficient is given by the following formula [71]

$$\gamma(\nu) = \frac{c^2}{\tau_{sp} 8\pi n_r^2 \nu_0^2} \frac{(2m_r)^{3/2}}{\pi\hbar^2} \int \sqrt{h\nu - E_g} \frac{2T_0}{(2\pi T_0^2)(\nu - \nu_0)^2 + 1} \left[f_c(\nu) - f_v(\nu)\right] \tag{A.4}$$

In most situation we can replace the lineshape function with $\delta(\nu - \nu_0)$. The substitution into eq. 2.2 lead to the following expression for the gain coefficient

$$\gamma(\nu_0) = \frac{\lambda_0^2}{\tau_{sp} 8\pi n_r^2} \frac{(2m_r)^{3/2}}{\pi\hbar^2} \sqrt{h\nu_0 - E_g} \left[f_c(\nu_0) - f_v(\nu_0)\right] \tag{A.5}$$

The result shoes that the gain coefficient exhibits a clear dependence on the band-gap energy, on the population inversion condition, expressed by $[f_c(\nu_0) - f_v(\nu_0)]$, on the amplified signal wavelength and on the temperature of the active medium.

Appendix B

Scalar Diffraction Theory

B.1 Rayleigh-Sommerfeld diffraction integral

The wave propagation inside a medium with refractive index n_r, is described by the scalar wave equation[105]

$$\nabla^2 u(\vec{r},t) - \frac{n_r^2}{c^2}\frac{\partial^2 u(\tilde{r},t)}{\partial^2 t^2} = 0 \tag{B.1}$$

where $u(\vec{r},t)$ refers to the scalar components of both the electric and magnetic field. For monochromatic wave, expressed $u(\vec{r},t) = \Re\{U(\vec{r},t)\}$[74], the wave equation assumes the following form

$$(\nabla^2 + k^2)\, U = 0 \tag{B.2}$$

called Helmholtz equation, with $U(\vec{r},t) = a(\vec{r})\exp[i\phi(\vec{r})]\exp[i2\pi\nu t]$ known as complex wavefunction and k wave number. The function $a(\vec{r})$ describe the wave amplitude, $\phi(\vec{r})$ its phase, while ν indicates the wave frequency.
The calculation of the complex wavefunction U at a certain observation point can be accomplished using the Green's Theorem[120], that is expressed in the form

$$\int\int\int_V (U\nabla^2 G - G\nabla^2 U)dv = \int\int_S \left(U\frac{\partial G}{\partial n} - G\frac{\partial U}{\partial n}\right) ds \tag{B.3}$$

where U and G are two complex functions of position, while S is a closed surface surrounding the volume V. The appropriate choice of the auxiliary Green's function, G, and of the closed surface S, allows the resolution of the diffraction problems.
Let us indicate with P_0 the observation point, while S is an arbitrary close surface surrounding P_0. If the Green function is chosen such that at an arbitrary point P_1 is given by [105]

$$G(P_1) = \frac{\exp(-ikr_{01})}{r_{01}} \tag{B.4}$$

where r_{01} is the length of the vector joining the point P_0 and P_1. It can be shown that G verifies the Helmholtz equation.
Substituting G into the expression of the Green theorem eq. B.3, leads to

$$U(P_0) = \frac{1}{4\pi}\int\int_S \left(G\frac{\partial U}{\partial n} - U\frac{\partial G}{\partial n}\right) ds \tag{B.5}$$

where n indicates the normal to the surface S.
The result in eq. B.5 expresses the Helmholtz-Kirchhoff integral theorem, stating that the field at any point P_0 is expressed in terms of the boundary values of the wave on any closed surface surrounding the point.
A different choice of the Green function is given by the following expression

$$G_-(P_1) = \frac{\exp(-ikr_{01})}{r_{01}} - \frac{\exp(-ik\tilde{r}_{01})}{\tilde{r}_{01}} \tag{B.6}$$

with $\tilde{r}_{01}$ being the distance between the point P_1 and $\tilde{P}_0$, which is the mirror image of P_0. In this case the G function is simultaneously generated by two sources at P_0 and $\tilde{P}_0$. By substituting this expression in eq. B.5 we obtained

$$U(P_0) = \frac{i}{\lambda}\int\int_\Sigma U(P_1)\frac{\exp(-ikr_{01})}{r_{01}} cos(\vec{n},\vec{r}_{01})ds \tag{B.7}$$

that is known as the Rayleigh-Sommerfeld diffraction formula. It follows that the field at a generic point P_0 can be determined by knowing the field on a point P_1 on the aperture $\$igma$, distant r_{01} from P_0. The Rayleigh-Sommerfeld diffraction integral expresses the Huygens-Fresnel principle, according to which every point on a wavefront is a sources of spherical waves.
If z indicates the distance between the initial plane and the observation plane, the vector joining P_0 and P_1 is given by

$$r_{01} = \sqrt{z^2 + (x_0 - x_1)^2 + (y_0 - y_1)^2} \tag{B.8}$$

The angle between the outward normal $\vec{n}$ and the vector $\vec{r_{01}}$, is given by the following relation

$$\cos\theta = z/r_{01} \tag{B.9}$$

Then, the integral in eq. B.7 assumes the following form

$$U(x_0, y_0, z) = \frac{iz}{\lambda}\int\int_\Sigma U(x_1, y_1, 0)\frac{e^{-ik\sqrt{z^2+(x_0-x_1)^2+(y_0-y_1)^2}}}{z^2 + (x_0 - x_1)^2 + (y_0 - y_1)^2}dx_1dy_1 \tag{B.10}$$

where it is assume that the initial plane is at $z = 0$.

B.2 Fresnel Approximation

When the paraxial approximation is valid, the distance between the two points in eq. B.8 can be written as

$$r_{01} \approx z + \frac{(x_0 - x_1)^2 + (y_0 - y_1)^2}{2z} \tag{B.11}$$

The substitution of this expression into eq. B.10 give the following formula

$$U(x_0, y_0, z) = \frac{ie^{-ikz}}{z\,\lambda} \int\int_{\Sigma} U(x_1, y_1, 0) \exp\left[-ik\frac{(x_0 - x_1)^2 + (y_0 - y_1)^2}{2z}\right] dx_1 dy_1 \tag{B.12}$$

which is the so called Fresnel diffraction integral.
It can be shown [121] that the propagation within a certain optical system, described by the ABCD matrix of the form

$$M = \begin{bmatrix} A & B \\ C & D \end{bmatrix} \tag{B.13}$$

can be solved if eq. B.12 modifies into

$$U(x_0, y_0, z) = \frac{i}{B\,\lambda} \int\int_{\Sigma} U(x_1, y_1, 0) \tag{B.14}$$
$$\exp\left[-ik\frac{A(x_1^2 + y_1^2) + D(x_0^2 + y_0^2) - 2x_0\,x_1 - 2y_0\,y_1}{2B}\right] dx_1 dy_1$$

when $A = D = 1$ and $B = z$ the two expression are equivalent.

Appendix C

Gaussian Beam

It can be shown that Gaussian beams are solutions of the diffraction integral problem when the Fresnel approximation is valid.
A Gaussian beam is described by the following expression for the complex amplitude [74]

$$U(x,y,z) = \frac{1}{q(z)} \exp\left[-ik\frac{x^2+y^2}{2q(z)}\right] \tag{C.1}$$

where q is referred to as the complex beam parameter. It is defined as

$$\frac{1}{q} = \frac{1}{R} - i\frac{\lambda}{\pi w^2} \tag{C.2}$$

R indicates the curvature radius of the beam wavefront, while w is called the beam size and defines the transverse scale of the beam. It is defined as the beam width when the intensity profile is equal to I_{max}/e. The minimum value of the beam width is called the beam waist, w_0. The variation of the curvature radius and of the beam size, with the propagation distance are expressed by the following formulas

$$\begin{aligned} R(z) &= z\left[1+\left(\frac{\pi w_0^2}{\lambda z}\right)^2\right] \\ w(z) &= w_0^2\left[1+\left(\frac{\lambda z}{\pi w_0^2}\right)\right] \end{aligned} \tag{C.3}$$

It is clear that, knowing of the beam waist and of its position, with respect to z makes possible the determination of the Gaussian beam at every value of z. Because of the diffraction, we can define the beam divergence as $\theta_0 = \lambda/w_0$.
The propagation of a Gaussian beam through a generic optical system, described by the ABCD matrix is given by the following

$$q_1 = \frac{A+Bq_0}{C+Dq_0} \tag{C.4}$$

and it is referred to as the ABCD-law of Gaussian beam.
The Gaussian beam is not the only eigensolution of the Fresnel diffraction integral. More in details, the full set of eigenmodes, also referred to as Hermite-Gaussian modes, can be written as

$$U(x,y,z) = H_l\left(\frac{\sqrt{2}x}{w}\right) H_m\left(\frac{\sqrt{2}m}{w}\right) e^{-ik(x^2+y^2)/2q} \tag{C.5}$$

where H_l and H_m are Hermite polynomials respectively of order m and n.

Appendix D

Discrete Fourier Transform and Scaled Fourier Transform

Light propagation within an optical system may be treated as a linear system, described by a certain transfer function, which is expressed through the diffraction integral A. As a consequence, Fourier analysis become an helpful tool in wave optics.
The continuous Fourier Transform (FT) of a 1D spatial function $f(x)$ is defined as[105]

$$F(x) = \mathcal{F}\{f(x)\} = \int_{-\infty}^{+\infty} f(x)e^{-i2\pi\nu_x x}dx \tag{D.1}$$

where x is the spatial variable and ν_x the spatial frequency. An equivalent expression is found also for 2D functions.
Most problems associated with optical propagation cannot be analytically solved and a numerical approach is needed. For this reason, an equivalent discrete form of eq. D.1 has been proposed. The integral in eq. D.1 can be expressed as a Riemann sum[107]

$$F(x_m) = \mathcal{F}\{f(x_n)\} = \sum_{n=-\infty}^{n=+\infty} g(x_n)e^{-i2\pi\nu_{xm}x_n}(x_{n+1} - x_n) \tag{D.2}$$

with n,m integers number going from $-\infty$ to $+\infty$. In real situation the numerical functions are defined over a finite number of samples, N. If δ indicates the sampling interval of the spatial variable, such that $x_n = n\delta$, the sampling interval of the spatial frequency variable is given by $\delta_f = 1/(N\delta)$, such that $\nu_{xm} = m\delta_f$. Therefore, the spatial frequency coordinates are inevitably related to the space variables. Finally, the Discrete Fourier Transform (DFT) becomes

$$F(\frac{m}{N\delta}) = \delta \sum_{n=-N/2}^{N/2-1} f(n\delta)\omega_N^{mn} \tag{D.3}$$

where $m, n = -N/2, 1 - N/2, ..., N/2 - 1$ and $\omega_N = exp(-i2\pi/N)$. Analogous considerations hold also for the inverse relations.
From an analysis of the Fresnel diffraction integral, it is clear that this last resembles the expression of a Fourier Transform. As a consequence DFTs are commonly used approach to solve Fresnel propagation problems. It can be shown that also the propagation within an arbitrary optical system can be reduced to the evaluation of DFTs. The fundamental limit of this approach is caused by the relationship between the space and the spatial frequency variable. Indeed, this implies a well definite

relationship between the initial and the observation coordinate variables. A solution to this problem was obtained by the two-step resolution method[107]. Here the propagation problem is solved through an intermediate plane, to relax the constraint condition. However, such a method remains accurate only for near field diffraction problem.
A novel approach to extend the applicability of FT-based resolution method was given by the work in [110], where the so called Scaled Fourier Transform is used (SFT). The SFT is a known concept in literature [122, 123] and its discrete version is expressed by the following formula

$$F_m = \sum_{n=-N/2}^{N/2-1} f_n \omega_N^{-\alpha mn} \tag{D.4}$$

where α is called the scale factor and indicates the proportionality factor between the sampling intervals of the initial and observation planes. When $\alpha = 1$ the SFT reduces to the ordinary DFT.
Using the identity $2mn = m^2 + n^2 - (n-m)^2$, eq. D.4 transforms into

$$F_m = \omega_N^{-m^2\alpha/2} \sum_{n=-N/2}^{n/2-1} f_n \omega_N^{-n^2\alpha/2} \omega_N^{\alpha(m-n)^2/2} \tag{D.5}$$

that can be viewed as discrete convolution of the form

$$F_m = \omega_N^{-m^2\alpha/2} \sum_{n=-N/2}^{n/2-1} g_n h_{n-m} \tag{D.6}$$

where

$$\begin{aligned} g_n &= f_n \omega_N^{-n^2\alpha/2} \\ h_n &= \omega_N^{\alpha(n)^2/2} \end{aligned} \tag{D.7}$$

The convolution can be solved via discrete version of the convolution theorem, after the linearization procedure via the zero-padding method. The final solution,F_n^{pad} consists of only the N points of interest.
Finally, the Fourier transform of scale α of the discrete function$f$ is given by

$$F_m = \omega_N^{-m^2\alpha/2} F_n^{pad} \tag{D.8}$$

For 2D discrete function, the scaled Fourier Transform is expressed by

$$F_{m_1,m_2} = \sum_{n_1=N/2}^{N/2-1} \sum_{n_2=N/2}^{N/2-1} f_{n_1,n_2} \omega_N^{-\alpha m_1 n_1} \omega_N^{-\alpha m_2 n_2} \tag{D.9}$$

The procedure for its solution, its equal for the one of 1D discrete functions.

Bibliography

[1] A. Einstein. "The Quantum Theory of Radiation". In: *Physikalische Zeitschrift* 18 (1917), pp. 121–128.

[2] J. P. Gordon, H. J. Zeiger, and C. H. Townes. "Molecular Microwave Oscillator and New Hyperfine Structure in the Microwave Spectrum of NH_3". In: *Phys. Rev.* 95 (1 1954), pp. 282–284.

[3] A. L. Schawlow and C. H. Townes. "Infrared and Optical Masers". In: *Phys. Rev.* 112 (6 1958), pp. 1940–1949.

[4] T. H. Maiman. "Stimulated Optical Radiation in Ruby". In: *Nature* 187 (4736 1960), pp. 493–494.

[5] A. Javan, W. R. Bennett, and D. R. Herriott. "Population Inversion and Continuous Optical Maser Oscillation in a Gas Discharge Containing a He-Ne Mixture". In: *Phys. Rev. Lett.* 6 (3 1961), pp. 106–110.

[6] R. N. Hall et al. "Coherent Light Emission From GaAs Junctions". In: *Phys. Rev. Lett.* 9 (9 1962), pp. 366–368.

[7] LaserFocusWorld in collaboration with SPIE. *2020 Summary | report*.

[8] F. Takamoto M.and Hong, R. Higashi, and H. Katori. "An optical lattice clock". In: *Nature* 435 (7040 2005), pp. 321–324.

[9] B. P. et all Abbott. "Observation of Gravitational Waves from a Binary Black Hole Merger". In: *Phys. Rev. Lett.* 116 (6 2016), p. 061102.

[10] V. S. Letokhov. "Laser biology and medicine". In: *Nature* 316 (6026 1985), pp. 325–330.

[11] Alster T. Husain Z. "The role of lasers and intense pulsed light technology in dermatology". In: *Clin Cosmet Investig Dermatol.* 9 (2016), pp. 29–40.

[12] *Illumination device and method for laser projector*. US Patent 6.870,650 B2. 2003.

[13] Xiaoming Zhu and J. M. Kahn. "Free-space optical communication through atmospheric turbulence channels". In: *IEEE Transactions on Communications* 50.8 (2002), pp. 1293–1300.

[14] J Dutta Majumdar and I Manna. "Laser material processing". In: *International Materials Reviews* 56.5-6 (2011), pp. 341–388.

[15] Pratik Shukla, Jonathan Lawrence, and Yu Zhang. "Understanding laser beam brightness: A review and new prospective in material processing". In: *Optics & Laser Technology* 75 (2015), pp. 40 –51.

[16] H. Injeyan and Goodno G.D. *High-power Laser handbook*. McGraw-Hill, 211.

[17] W. J. Witteman. "High-Output power and long lifetimes of sealed-off CO2 lasers". In: *Applied Physics Letters* 11.11 (1967), pp. 337–338.

[18] IPG Photonics. *Fiber Lasers, Laser Systems and Beam Delivery*. 2020. URL: https://www.ipgphotonics.com/en/products.

[19] P. Crump et al. “85 % power conversion efficiency 975 nm broad area diode laser at -50 C, 76 % at 10 C”. In: *2006 Conference on Lasers and Electro-Optics and 2006 Quantum Electronics and Laser Science Conference* (2006), pp. 1–2.

[20] David G. Mehuys. *Chapter 4 - High-Power Semiconductor Lasers*. Ed. by Eli Kapon. San Diego: Academic Press, 1999, pp. 259 –321.

[21] J.W. Tomm et al. “Mechanisms and fast kinetics of the catastrophic optical damage (COD) in GaAs-based diode lasers”. In: *Laser & Photonics Reviews* 5.3 (2011), pp. 422–441.

[22] O. Hess, S. W. Koch, and J. V. Moloney. “Filamentation and beam propagation in broad-area semiconductor lasers”. In: *IEEE Journal of Quantum Electronics* 31.1 (1995).

[23] J. R. Marciante and G. P. Agrawal. “Nonlinear mechanisms of filamentation in broad-area semiconductor lasers”. In: *IEEE Journal of Quantum Electronics* 32.4 (1996), pp. 590–596.

[24] J. P. Donnelly et al. “AlGaAs-InGaAs slab-coupled optical waveguide lasers”. In: *IEEE Journal of Quantum Electronics* 39.2 (2003), pp. 289–298.

[25] Donnelly J. P. et al. “AlGaAs-InGaAs slab-coupled optical waveguide lasers”. In: *IEEE Journal of Quantum Electronics* 39.2 (2003), pp. 289–298.

[26] Coherent DILAS. *Tapered Amplifier*. 2018. URL: http://dilas.com.

[27] P. Crump et al. “Development of high-power diode lasers with beam parameter product below 2 mm x mrad within the BRIDLE project”. In: 9348 (2015). Ed. by Mark S. Zediker, pp. 98 –108.

[28] Christian Lauer et al. “Advances in performance and beam quality of 9xx-nm laser diodes tailored for efficient fiber coupling”. In: 8241 (2012). Ed. by Mark S. Zediker, pp. 282 –291.

[29] Martin Behringer. “High-Power Diode Laser Technology and Characteristics”. In: *High Power Diode Lasers: Technology and Applications*. Ed. by Friedrich Bachmann, Peter Loosen, and Reinhart Poprawe. Springer New York, 2007, pp. 5–74.

[30] Peter Loosen and Alexander Knitsch. “Incoherent Beam Superposition and Stacking”. In: *High Power Diode Lasers: Technology and Applications*. Ed. by Friedrich Bachmann, Peter Loosen, and Reinhart Poprawe. Springer New York, 2007, pp. 121–179.

[31] Joerg Malchus et al. “A 40kW fiber-coupled diode laser for material processing and pumping applications”. In: *High-Power Diode Laser Technology and Applications XIII*. Ed. by Mark S. Zediker. Vol. 9348. International Society for Optics and Photonics. SPIE, 2015, pp. 1 –12.

[32] *Arrangement of multiple diode laser module and method for operating the same*. US Patent 9,318,876 B1. 2016.

[33] Stefan Heinemann et al. “Compact high brightness diode laser emitting 500W from a 100um fiber”. In: *High-Power Diode Laser Technology and Applications XI*. Ed. by Mark S. Zediker. Vol. 8605. International Society for Optics and Photonics. SPIE, 2013, pp. 191 –197.

[34] T. Y. Fan. “Laser beam combining for high-power, high-radiance sources”. In: *IEEE Journal of Selected Topics in Quantum Electronics* 11.3 (2005), pp. 567–577.

[35] A. Sanchez Rubio et al. "Wavelength beam combining for power and brightness scaling of laser systems". In: *lincoln Laboratory Journal* 20.2 (2014), pp. 52–67.

[36] K. Nosu, H. Ishio, and K. Hashimoto. "Multireflection optical multi/demultiplexer using interference filters". In: *Electronics Letters* 15.14 (1979), pp. 414–415.

[37] Peter O. Minott and James B. Abshire. "Grating Rhomb Diode Laser Power Combiner". In: *Optical Technologies for Space Communication Systems*. Ed. by Kul B. Bhasin and Gerhard A. Koepf. Vol. 0756. International Society for Optics and Photonics. SPIE, 1987, pp. 38 –49.

[38] V. Daneu et al. "Spectral beam combining of a broad-stripe diode laser array in an external cavity". In: *Opt. Lett.* 25.6 (2000), pp. 405–407.

[39] B. Previtali et al. In: *Proceedings of Lasers in Manufacturing Conference 2015*. 2015.

[40] G. Costa Rodrigues, H. Vanhove, and J.R. Duflou. "Direct Diode Lasers for Industrial Laser Cutting: A Performance Comparison with Conventional Fiber and CO2 Technologies". In: *Physics Procedia* 56 (2014), pp. 901 –908.

[41] Robin K. Huang et al. "Teradiode's high brightness semiconductor lasers". In: *Components and Packaging for Laser Systems II*. Ed. by Alexei L. Glebov and Paul O. Leisher. Vol. 9730. International Society for Optics and Photonics. SPIE, 2016, pp. 63 –71.

[42] H. Zimer et al. "Beam combining technologies for direct diode laser systems at the kW power level". In: *2013 High Power Diode Lasers and Systems Conference (HPD)*. 2013, pp. 38–39.

[43] Lumentum. *Products*. 2020. URL: https://www.lumentum.com/en.

[44] Joerg Malchus et al. "A 40kW fiber-coupled diode laser for material processing and pumping applications". In: *High-Power Diode Laser Technology and Applications XIII*. Ed. by Mark S. Zediker. Vol. 9348. International Society for Optics and Photonics. SPIE, 2015, pp. 1 –12.

[45] *HighLight DL HQ Series*. 2020. URL: https://it.coherent.com/lasers/laser/highlight-dl-series.

[46] *Kilowatt-Class diode laser system*. US Patent 8,488,245 B1. 2013.

[47] *Beam combining light source*. US Patent 8,427,749 B2. 2013.

[48] Joerg Malchus et al. "A 25kW fiber-coupled diode laser for pumping applications". In: *High-Power Diode Laser Technology and Applications XII*. Ed. by Mark S. Zediker. Vol. 8965. International Society for Optics and Photonics. SPIE, 2014, pp. 62 –71.

[49] *Arrangement of multiple diode laser module and methods for operating the same*. US Patent 9,318,876 B1. 2016.

[50] Bernd Köhler et al. "Multi-kW high-brightness fiber coupled diode laser". In: *High-Power Diode Laser Technology and Applications XI*. Ed. by Mark S. Zediker. Vol. 8605. International Society for Optics and Photonics. SPIE, 2013, pp. 68 –75.

[51] *Wavelength combined laser system*. US Patent 9,391,425 B2. 2016.

[52] *Multi-wavelength beam combining system and method*. US Patent 9,104,029 B2. 2015.

[53] *High brightness dense wavelength multiplexing laser*. US Patent 9,391,713 B2. 2016.

[54] U. Witte et al. "kW-class direct diode laser for sheet metal cutting based on DWDM of pump modules by use of ultra-steep dielectric filters". In: *Opt. Express* 24.20 (2016), pp. 22917–22929.

[55] Gregory D. Goodno and Joshua E. Rothenberg. "Engineering of Coherently Combined, High-Power Laser Systems". In: *Coherent Laser Beam Combining*. John Wiley & Sons, Ltd, 2013. Chap. 1, pp. 1–44.

[56] Shawn M. Redmond et al. "Active coherent beam combining of diode lasers". In: *Opt. Lett.* 36.6 (2011), pp. 999–1001.

[57] N. Satyan et al. "Coherent Power Combination of Semiconductor Lasers Using Optical Phase-Lock Loops". In: *IEEE Journal of Selected Topics in Quantum Electronics* 15.2 (2009), pp. 240–247.

[58] Kevin J. Creedon et al. "High efficiency coherent beam combining of semiconductor optical amplifiers". In: *Opt. Lett.* 37.23 (2012), pp. 5006–5008.

[59] M. A. Vorontsov and V. P. Sivokon. "Stochastic parallel-gradient-descent technique for high-resolution wave-front phase-distortion correction". In: *J. Opt. Soc. Am. A* 15.10 (1998), pp. 2745–2758.

[60] Juan Montoya et al. "External cavity beam combining of 21 semiconductor lasers using SPGD". In: *Appl. Opt.* 51.11 (2012), pp. 1724–1728.

[61] D. R. Scifres, R. D. Burnham, and W. Streifer. "Phase-locked semiconductor laser array". In: *Applied Physics Letters* 33.12 (1978), pp. 1015–1017.

[62] Lew Goldberg and J. F. Weller. "Single lobe operation of a 40-element laser array in an external ring laser cavity". In: *Applied Physics Letters* 51.12 (1987), pp. 871–873.

[63] Christopher J. Corcoran and Frederic Durville. "Passive coherent combination of a diode laser array with 35 elements". In: *Opt. Express* 22.7 (2014), pp. 8420–8425.

[64] C.X. Yu and T.Y. Fan. "Beam Combining". In: *High-power Laser handbook*. Ed. by H. Injeyan and Goodno G.D. McGraw-Hill, 2011. Chap. 19.

[65] H.F. Talbot Esq. F.R.S. "I. Facts relating to optical science. No. III". In: *The London, Edinburgh, and Dublin Philosophical Magazine and Journal of Science* 9.51 (1836), pp. 1–4.

[66] David Paboeuf et al. "Narrow-line coherently combined tapered laser diodes in a Talbot external cavity with a volume Bragg grating". In: *Applied Physics Letters* 93.21 (2008), p. 211102.

[67] B. Liu and Y. Braiman. "Coherent beam combining of high power broad-area laser diode array with near diffraction limited beam quality and high power conversion efficiency". In: *Opt. Express* 21.25 (2013), pp. 31218–31228.

[68] R. K. Huang et al. "High-power coherent beam combination of semiconductor laser arrays". In: *2008 Conference on Lasers and Electro-Optics and 2008 Conference on Quantum Electronics and Laser Science*. 2008, pp. 1–2.

[69] G. Schimmel et al. "Rear-side resonator architecture for the passive coherent combining of high-brightness laser diodes". In: *Opt. Lett.* 41.5 (2016), pp. 950–953.

[70] Amnon Yariv and Pochi Yeh. *Photonics: Optical Electronics in Modern Communications (The Oxford Series in Electrical and Computer Engineering)*. Oxford University Press Inc, 2006.

[71] M. J. Connelly. "Wideband semiconductor optical amplifier steady-state numerical model". In: *IEEE Journal of Quantum Electronics* 37.3 (2001), pp. 439–447.

[72] S.M. Sze and K.K. Ng. *Physics of Semiconductor Devices*. Wiley, 2006.

[73] N. K. Dutta. "Calculated absorption, emission, and gain in In0.72Ga0.28As0.6P0.4". In: *Journal of Applied Physics* 51.12 (1980), pp. 6095–6100.

[74] Bahaa E. A. Saleh and Malvin Carl Teich. John Wiley & Sons, Ltd, 2001.

[75] N.K. Dutta and Q. Wang. *Semiconductor Optical Amplifiers (Second Edition)*. World Scientific Publishing Co Pte Ltd, 2013.

[76] N. K. Dutta and R. J. Nelson. "The case for Auger recombination in In1xGaxAsyP1y". In: *Journal of Applied Physics* 53.1 (1982), pp. 74–92.

[77] Bozena Jaskorzynska, Johan Nilsson, and Lars Thylén. "Modal reflectivity of uptapered, tilted-facet, and antireflection-coated diode-laser amplifiers". In: *J. Opt. Soc. Am. B* 8 (1991), pp. 484–493.

[78] Thorlabs. *C-band booster optical amplifiers*. 2020. URL: https://www.thorlabs.de/thorproduct.cfm?partnumber=BOA1007H.

[79] Haiyin Sun. *Semiconductor lasers*. Springer, 2015.

[80] Govind P Agrawal and Niloy K Dutta. *A practical guide to handling laser diode beams*. Springer Science & Business Media, 2013.

[81] Prashant V. Kamat, Nada M. Dimitrijevic, and A. J. Nozik. "Dynamic Burstein-Moss shift in semiconductor colloids". In: *J. Phys. Chem.* 93 (1989), pp. 2873–2875.

[82] J. Huang and L.W. Casperon. "Gain and saturation in semiconductor lasers". In: *Optical and Quantum Electronics* 25 (6 1993), pp. 369–390.

[83] Andrej Marculescu et al. "Spectral signature of nonlinear effects in semiconductor optical amplifiers". In: *Opt. Express* 25.24 (2017), pp. 29526–29559.

[84] C. Henry. "Theory of the linewidth of semiconductor lasers". In: *IEEE Journal of Quantum Electronics* 18.2 (1982), pp. 259–264.

[85] B. R. Bennett, R. A. Soref, and J. A. Del Alamo. "Carrier-induced change in refractive index of InP, GaAs and InGaAsP". In: *IEEE Journal of Quantum Electronics* 26.1 (1990), pp. 113–122.

[86] M. Willatzen et al. "Nonlinear gain suppression in semiconductor lasers due to carrier heating". In: *IEEE Photonics Technology Letters* 3.7 (1991), pp. 606–609.

[87] Govind P. Agrawal. "Spectral hole burning and gain saturation in semiconductor lasers: Strong signal theory". In: *Journal of Applied Physics* 63.4 (1988), pp. 1232–1235.

[88] Amnon Yariv. *Optical electronics*. Saunders College Publ, 1991.

[89] Paul W Juodawlkis et al. "Continuous-wave two-photon absorption in a Watt-class semiconductor optical amplifier". In: *Optics Express* 16.16 (2008), pp. 12387–12396.

[90] HK Tsang et al. "Two-photon absorption and self-phase modulation in InGaAsP/InP multi-quantum-well waveguides". In: *Journal of applied physics* 70.7 (1991), pp. 3992–3994.

[91] John R. Andrews. "Interferometric power amplifiers". In: *Opt. Lett.* 14.1 (1989), pp. 33–35.

[92] Gregory L. Schuster and John R. Andrews. "Coherent summation of saturated AlGaAs amplifiers". In: *Opt. Lett.* 18.8 (1993), pp. 619–621.

[93] D. Wolfson et al. "40-Gb/s all-optical wavelength conversion, regeneration, and demultiplexing in an SOA-based all-active Mach-Zehnder interferometer". In: *IEEE Photonics Technology Letters* 12.3 (2000), pp. 332–334.

[94] Joo-Youp Kim et al. "All-Optical Multiple Logic Gates With XOR, NOR, OR, and NAND Functions Using Parallel SOA-MZI Structures: Theory and Experiment". In: *J. Lightwave Technol.* 24.9 (2006), p. 3392.

[95] Orazio Svelto. *Priciple of Lasers (Fifth edition)*. Springer, 2011.

[96] Anthony A. Tovar and Lee W. Casperson. "Generalized Sylvester theorems for periodic applications in matrix optics". In: *J. Opt. Soc. Am. A* 12.3 (1995), pp. 578–590.

[97] Herwig Kogelnik and Tingye Li. "Laser beams and resonators". In: *Applied optics* 5.10 (1966), pp. 1550–1567.

[98] A. G. Fox and T. Li. "Resonant modes in a maser interferometer". In: *The Bell System Technical Journal* 40.2 (1961), pp. 453–488.

[99] A. E. Siegman and H. Y. Miller. "Unstable Optical Resonator Loss Calculations Using the Prony Method". In: *Appl. Opt.* 9.12 (1970), pp. 2729–2736.

[100] MR Sayeh, Hans R Bilger, and Taufiq Habib. "Optical resonator with an external source: excitation of the Hermite-Gaussian modes". In: *Applied optics* 24.22 (1985), pp. 3756–3761.

[101] William S. C. Chang. *Fundamentals of Guided-Wave Optoelectronic Devices*. Cambridge University Press, 2009.

[102] Dana Z Anderson. "Alignment of resonant optical cavities". In: *Applied Optics* 23.17 (1984), pp. 2944–2949.

[103] Frank J Duarte. *Tunable lasers handbook*. Elsevier, 1996.

[104] Haiyin Sun. "Simple mathematical model for designing laser diode focusing optics with a large numerical aperture". In: *Optical Engineering* 53.10 (2014), p. 105105.

[105] Joseph W Goodman. *Introduction to Fourier optics*. Roberts and Company Publishers, 2005.

[106] Yitzhak Katznelson. *An introduction to harmonic analysis*. Cambridge University Press, 2004.

[107] Jason Schmidt. "Numerical simulation of optical wave propagation with examples in MATLAB". In: Society of Photo-Optical Instrumentation Engineers. 2010.

[108] William H Press et al. *Numerical recipes 3rd edition: The art of scientific computing*. Cambridge university press, 2007.

[109] Fabin Shen and Anbo Wang. "Fast-Fourier-transform based numerical integration method for the Rayleigh-Sommerfeld diffraction formula". In: *Applied optics* 45.6 (2006), pp. 1102–1110.

[110] Victor Nascov and Petre Cătălin Logofătu. "Fast computation algorithm for the Rayleigh-Sommerfeld diffraction formula using a type of scaled convolution". In: *Applied optics* 48.22 (2009), pp. 4310–4319.

[111] N Delen and B Hooker. "Free-space beam propagation between arbitrarily oriented planes based on full diffraction theory: a fast Fourier transform approach". In: *JOSA A* 15.4 (1998), pp. 857–867.

[112] Tomoyoshi Shimobaba et al. "Scaled angular spectrum method". In: *Optics letters* 37.19 (2012), pp. 4128–4130.

[113] Christof Pruss, Eugenio Garbusi, and Wolfgang Osten. "Testing Aspheres". In: *Optics & Photonics News* 19.4 (2008), p. 24.

[114] Yuhan Gao et al. "Automatic optimization design of Gaussian beam shaping system by using ZEMAX software". In: *Optik* 122.24 (2011), pp. 2176–2180.

[115] Andrew Stockham and John G Smith. "Tolerancing microlenses using ZEMAX". In: *Micromachining Technology for Micro-Optics and Nano-Optics IV*. Vol. 6110. International Society for Optics and Photonics. 2006, 61100U.

[116] Norman Hodgson and Horst Weber. *Optical resonators: fundamentals, advanced concepts, applications*. Vol. 108. Springer Science & Business Media, 2005.

[117] Michael Lang. "Correcting astigmatism in diode lasers". In: *Lasers & Optronics* 8.9 (1989), pp. 51–54.

[118] Eli Kapon. *Semiconductor Lasers II: Materials and Structures*. Elsevier, 1999.

[119] Larry A. Coldren Scott and W. Corzine Milan L. Masanovic. *Diode Lasers and Photonic Integrated Circuits*. John Wiley & Sons, 2012.

[120] George Green. *An essay on the application of mathematical analysis to the theories of electricity and magnetism*. Wezäta-Melins Aktiebolag, 1828.

[121] Stuart A Collins. "Lens-system diffraction integral written in terms of matrix optics". In: *JOSA* 60.9 (1970), pp. 1168–1177.

[122] Haldun M Ozaktas and M Alper Kutay. "The fractional Fourier transform". In: *2001 European Control Conference (ECC)*. IEEE. 2001, pp. 1477–1483.

[123] Haldun M Ozaktas et al. "Digital computation of the fractional Fourier transform". In: *IEEE Transactions on signal processing* 44.9 (1996), pp. 2141–2150.